

Copyright  
by  
Yu-Sheng Su  
2013

**The Dissertation Committee for Yu-Sheng Su certifies that this is the approved  
version of the following dissertation:**

**RECHARGEABLE LITHIUM-SULFUR BATTERIES WITH NOVEL  
ELECTRODES, CELL CONFIGURATIONS, AND RECHARGE  
STRATEGIES**

**Committee:**

---

Arumugam Manthiram, Supervisor

---

John B. Goodenough

---

Charles Buddie Mullins

---

Paulo J. Ferreira

---

Guihua Yu

**RECHARGEABLE LITHIUM-SULFUR BATTERIES WITH  
NOVEL ELECTRODES, CELL CONFIGURATIONS, AND  
RECHARGE STRATEGIES**

**by**

**Yu-Sheng Su, B.S., M.S.**

**Dissertation**

Presented to the Faculty of the Graduate School of  
The University of Texas at Austin  
in Partial Fulfillment  
of the Requirements  
for the Degree of

**Doctor of Philosophy**

**The University of Texas at Austin**

**August 2013**

## **Dedication**

Dedicated to my wife Rena, my boy Neil, and my parents Chih-Ping & Hsiu-Ying.

## **Acknowledgements**

First of all, I must offer my heartfelt thanks to my supervisor, Professor Arumugam Manthiram, for his intelligent instruction and guidance without conservation. If he hadn't recruited me in his lab and helped me apply for my fellowship, I wouldn't have had such a good environment to complete all of the projects in my dissertation. He is always supportive and encouraging me to try new approaches to solve the problems in the energy storage systems, which are risky; however, great rewards will be obtained if succeeded. I also want to express my gratitude to all my dissertation committee members, Professor John B. Goodenough, Charles Buddie Mullins, Paulo J. Ferreira, and Guihua Yu. They all agreed to serve on my committee without hesitation and gave me useful suggestions during my preliminary oral examination.

It's impossible to handle every task on your own, so I would like to thank all of the lab members for their help and understanding. I learned a lot from Dr. Fu, who is a generous and experienced researcher and always patient. Katharine Chemelewski polished most of my papers, fast and accurate. Eun Sung Lee, Thomas Cochell, Anmin Cao, Chih-Chieh Wang, Chih-Liang Wang, Longjun Li, Sheng-Heng Chung, and Chenxi Zu assisted my experiments on various aspects. I want to thank them wholeheartedly again.

Last but not least, I want to show my sincere appreciation to my lovely wife, Jen-Yen, who spent most of her time on taking care of our newborn Chen-Kuan, a crying machine. My mother-in-law also contributed a lot to this. I owe them many thanks. Of course, to raise a kid up until he gets a PhD degree is never easy, so I hope my parents both will be proud of me. Thank you, Dad and Mom. I made it.

# **RECHARGEABLE LITHIUM-SULFUR BATTERIES WITH NOVEL ELECTRODES, CELL CONFIGURATIONS, AND RECHARGE STRATEGIES**

Yu-Sheng Su, Ph.D.

The University of Texas at Austin, 2013

Supervisor: Arumugam Manthiram

Entering a new era of green energy, several criteria such as cost, cycle life, safety, efficiency, energy, and power need to be considered in developing electrical energy storage systems for transportation and grid storage. Lithium–sulfur (Li-S) batteries are one of the prospective candidates in this regard as sulfur offers a high theoretical capacity of 1675 mAh g<sup>-1</sup> at a safer operating voltage range of ~ 2.1 V and low-cost benefit. This dissertation explores various original designs of novel electrodes, new cell configurations, and recharge strategies that can boost the cycle performance of Li-S cells.

An *in situ* sulfur deposition route has been developed for synthesizing sulfur-carbon composites as cathode materials. This facile synthesis method involves the precipitation of elemental sulfur at the interspaces between carbon nanoparticles in aqueous solution at room temperature. Thus, a sulfur/multi-wall carbon nanotube (MWCNT) composite cathode with high-rate cyclability has been synthesized by the same process. Due to the self-weaving behavior of MWCNTs, extra cell components such as binders and current collectors are rendered unnecessary, thereby streamlining the electrode manufacturing process and decreasing the cell weight.

A novel Li-S cell configuration with a carbon interlayer inserted between the separator and cathode has been designed to enhance the battery cyclability as well. A conductive MWCNT interlayer acting as a pseudo-upper current collector not only reduces the charge transfer resistance of sulfur cathodes significantly, but also localizes and retains the dissolved active material during cycling. Moreover, with a bi-functional microporous carbon paper intrerlayer, we observe a significant improvement not only in the active material utilization but also in capacity retention, without involving complex synthesis or surface modification.

The kinetics of the sulfur/long-chain polysulfide redox couple ( $S_8 \leftrightarrow Li_2S_4$ , theoretical capacity = 419 mAh g<sup>-1</sup>) is experimentally proven to be very fast in the Li-S system. The Li-S cell with a blended carbon interlayer retains excellent cycle stability and possesses a high percentage of active material utilization over 250 cycles at high C rates (up to 15C). The meso-/micro- pores in the interlayer are in charge of accommodating the shuttling polysulfides and offering sufficient electrolyte accessibility.

An appropriate and applicable way to recharge Li-S cells within the lower plateau region has been designed to offer tremendous improvement with various Li-S battery systems. Adjusting the charging condition led to long cycle life (over 500 cycles) with excellent capacity retention (> 99%) by inhibiting the electrochemical reactions along with polysulfide dissolution. In addition, the redox products determined by *ex situ* x-ray photoelectron spectroscopy (XPS) further clarify the mechanism of polysulfide formation upon cycling, which is partially different from the general consensus. These approaches of novel electrode designs, new cell configurations, charging strategy, and understanding of the reactions in different discharge steps could progress the development and advancement of Li-S batteries.

## Table of Contents

List of Tables .....	xiii
List of Figures .....	xiv
Chapter 1: Introduction .....	1
1.1 Rechargeable Lithium-Sulfur Batteries .....	1
1.1.1 Mechanism .....	1
1.1.2 Applications .....	4
1.2 Challenges of Li-S Batteries .....	5
1.2.1 Insulating active materials .....	5
1.2.2 Polysulfide dissolution .....	6
1.2.3 Self-discharge .....	6
1.2.4 Shuttle effect .....	7
1.2.5 $\text{Li}_2\text{S}$ and sulfur plating .....	7
1.2.6 Volume expansion .....	7
1.3 Cathodes for Li-S Batteries .....	8
1.3.1 Sulfur-carbon composites .....	9
1.3.1.1 Porous carbon substrates .....	10
1.3.1.2 Impact of pore structures .....	10
1.3.1.3 Binder-free cathodes .....	11
1.3.1.4 Graphene composites .....	11
1.3.1.5 Surface functionalization .....	12
1.3.2 Sulfur-polymer composites .....	13
1.3.3 Alternative composites .....	14
1.3.3.1 Metal oxide additives/composites .....	14
1.3.3.2 Intercalation compound composites .....	15
1.3.3.3 Metal coatings .....	16
1.3.4 $\text{Li}_2\text{S}$ as the cathode material .....	16
1.3.5 Current collectors .....	17
1.3.6 Binders .....	18

1.4 Separators for Li-S Batteries.....	18
1.5 Electrolytes for Li-S Batteries .....	19
1.5.1 Liquid-phase electrolytes .....	20
1.5.2 Lithium salts for electrolytes .....	21
1.5.3 Ionic liquid electrolytes.....	22
1.5.4 Gel polymer/solid-state electrolytes .....	23
1.6 Anodes for Li-S Batteries .....	23
1.7 Working Temperatures for Li-S Batteries .....	23
1.8 Working Voltage Windows for Li-S Batteries .....	24
1.9 Objectives for this Dissertation.....	25
Chapter 2: General experimental procedures.....	27
2.1 Materials synthesis.....	27
2.2 Materials characterization.....	27
2.2.1 X-ray diffraction (XRD) .....	27
2.2.2 Thermogravimetric analysis (TGA).....	27
2.2.3 Scanning electron microscopy (SEM) and Transmission electron microscopy (TEM).....	28
2.2.4 Energy dispersive X-ray spectroscopy (EDS) .....	28
2.2.5 Surface area and pore size measurements.....	28
2.2.6 Raman spectroscopy .....	28
2.2.7 X-ray photoelectron spectroscopy (XPS) .....	29
2.3 Electrochemical characterization .....	29
2.3.1 Cell assembly .....	29
2.3.2 Cycle performance and rate capability test.....	30
2.3.3 Cyclic voltammograms (CV).....	30
2.3.4 Electrochemical impedance spectroscopy (EIS).....	30
Chapter 3: A facile <i>in situ</i> sulfur deposition route to obtain carbon-wrapped sulfur composite cathodes for lithium-sulfur batteries.....	31
3.1 Introduction.....	31
3.2 Experimental .....	33

3.2.1 <i>In situ</i> sulfur deposition synthesis of sulfur-carbon composites	33
3.2.2 Structural and microstructure characterizations	35
3.2.3 Cell assembly	35
3.2.4 Electrochemical characterizations	36
3.3 Results and discussion	37
3.3.1 XRD, SEM, TEM and EDS studies	37
3.3.2 Electrochemical properties	40
3.3.3 SEM and EIS analysis of cycled electrodes	44
3.4 Conclusions	47
Chapter 4: Self-weaving sulfur-carbon composite cathodes for high rate lithium-sulfur batteries	49
4.1 Introduction	49
4.2 Experimental	51
4.2.1 Synthesis	51
4.2.2 Materials characterizations	51
4.2.3 Electrochemical measurements	52
4.3 Results and discussion	53
4.3.1 Fabrication, structure, and microstructure	53
4.3.2 Electrochemical performance	57
4.3.3 Microstructure after cycling	63
4.4 Conclusions	65
Chapter 5: A new approach to improve cycle performance of rechargeable lithium-sulfur batteries by inserting a free-standing MWCNT interlayer	67
5.1 Introduction	67
5.2 Experimental	71
5.2.1 Synthesis and interlayer fabrication	71
5.2.2 Microstructure and elemental analysis	72
5.2.3 Electrochemical analysis	72
5.3 Results and discussion	73
5.3.1 Electrochemical characterizations	73

5.3.2 Morphological change during cycling .....	75
5.3.3 Cycle performance .....	77
5.4 Conclusions.....	79
Chapter 6: Lithium-sulfur batteries with a microporous carbon paper as a bi-functional interlayer.....	81
6.1 Introduction.....	81
6.2 Experimental.....	82
6.2.1 Synthesis and characterizations .....	82
6.2.2 Cell assembly .....	83
6.2.3 Electrochemistry .....	83
6.3 Results and discussion .....	84
6.3.1 Cell configuration of the Li / MCP interlayer / S battery .....	84
6.3.2 Pore-filling process of the MCP interlayer during cycling.....	85
6.3.3 Surface morphology and elemental analysis of the MCP interlayer .....	88
6.3.4 Electrochemical performance of the Li-S batteries with the MCP interlayer .....	88
6.3.5 Impact of pore size.....	91
6.4 Conclusions.....	92
Chapter 7: Fast, reversible lithium storage with sulfur/long-chain polysulfide redox couple.....	93
7.1 Introduction.....	93
7.2 Experimental.....	94
7.2.1 Synthesis and materials characterizations.....	94
7.2.2 Electrochemical characterizations .....	95
7.3 Results and discussion .....	96
7.3.1 Morphological analysis.....	96
7.3.2 Electrochemical analysis.....	98
7.3.3 Surface area and pore size distribution .....	102
7.3.4 Morphological change; elemental and surface analysis.....	104
7.4 Conclusions.....	108

Chapter 8: A strategic approach to recharge Li-S batteries for long cycle life....	109
8.1 Introduction.....	109
8.2 Experimental.....	113
8.2.1 Preparation of Li-S cells with microporous interlayers.....	113
8.2.2 Preparation of Li/dissolved polysulfide cells.....	114
8.2.3 Battery test.....	115
8.2.4 Air-sensitive XPS analysis.....	115
8.3 Results and discussion.....	116
8.3.1 Battery performance with extended cycles.....	116
8.3.2 <i>Ex situ</i> XPS analysis of polysulfides.....	119
8.3.3 Discharge mechanism of the Li-S battery.....	123
8.3.4 Long cycle life with the LiNO <sub>3</sub> -free electrolyte.....	124
8.3.5 Dissolved polysulfide cells with the modified recharge setting.....	126
8.4 Conclusions.....	127
Chapter 9: Summary.....	129
Appendix: List of Publications.....	131
References.....	133
Vita.....	142

## **List of Tables**

Table 8.1: Summary of the performance of advanced Li-S battery systems .....110

## List of Figures

Figure 1.1: Schematic illustration of an ideal Li-S battery during (a) discharging and (b) charging .....	3
Figure 1.2: Schematic illustration of a Li-S battery with a liquid electrolyte during (a) discharging and (b) charging .....	3
Figure 1.3: (a) Discharge profile and (b) charge profile of a fully utilized Li-S battery .....	5
Figure 1.4: Illustration of sulfur confined in the interconnected pore structure of CMK-3, a mesoporous carbon, separated apart by carbon nanofibers .....	9
Figure 1.5: (a) The cell configuration of a Li/dissolved polysulfide cell and the addition of polysulfide catholyte into a MWCNT electrode. (b) Voltage vs. time profile of the cell at C/10 rate.....	10
Figure 1.6: Scheme of sulfur immobilized on graphene oxide nanosheets. The enhanced binding of S to the C-C bond is due to epoxy or hydroxyl group. S atoms (yellow), oxygen atoms (red), hydrogen atoms (white), and bonded carbon atoms (blue) are highlighted.....	13
Figure 1.7: The formation mechanism of the one-step, bottom-up of PVP-encapsulated hollow S nanospheres .....	14
Figure 1.8: Schematic fabrication process to form TiO <sub>2</sub> -sulfur yolk-shell nanostructure.....	15
Figure 1.9: The model for the initial charging of Li <sub>2</sub> S with slow kinetics .....	17

Figure 1.10: The cell configuration of the Li-S battery with a bi-functional carbon interlayer that can reduce the charge-transfer resistance and capture unstable migrating polysulfides .....	20
Figure 1.11: The overview of solid-state-based and liquid-based electrolytes. Solvent-in-salt belongs to liquid phase but with salt content more than 50% .....	22
Figure 1.12: Schematic diagrams illustrates the recharge strategy for elongating the cycle life of Li-S cells .....	25
Figure 3.1: Scheme illustrating the <i>in situ</i> sulfur deposition route to obtain the sulfur-carbon composite.....	34
Figure 3.2: XRD patterns of the pure sulfur, sulfur-carbon composite, and carbon black.....	37
Figure 3.3: SEM images of the (a) carbon black, (b) pure sulfur, and (c) sulfur-carbon composite with carbon-wrapped sulfur network structure.....	39
Figure 3.4: (a) Low and (b) high magnification TEM images of the sulfur-carbon composite and (c) EDS analysis of (b) showing the existence of both sulfur and carbon.....	40
Figure 3.5: Cyclic voltammetry plots of the cathodes fabricated with the (a) pure sulfur and (b) sulfur-carbon composite at a scan rate of $0.05 \text{ mV s}^{-1}$ under a voltage window of $1.0 - 3.5 \text{ V}$ (vs. $\text{Li}^+/\text{Li}$ ).....	41
Figure 3.6: (a) First charge/discharge profile and (b) discharge curves at various cycles of the pure sulfur and sulfur-carbon composite cathodes cycled at $1.5 - 2.8 \text{ V}$ (vs. $\text{Li}^+/\text{Li}$ ) at a rate of C/20 .....	43

Figure 3.7: Comparison of the cyclability of the (a) pure sulfur and sulfur-carbon composite cathodes at a rate of C/20 and the (b) sulfur-carbon composite cathode at various C rates .....	44
Figure 3.8: SEM images of the (a) pure sulfur and (b) sulfur-carbon composite cathodes before cycling and the (c) pure sulfur and (d) sulfur-carbon composite cathodes after cycling at C/5 rate for 25 cycles.....	45
Figure 3.9: Electrochemical impedance spectra of the pure sulfur and sulfur-carbon composite cathodes before and after cycling at C/5 rate .....	47
Figure 4.1: Schematic fabrication process of a self-weaving sulfur-MWCNT composite cathode synthesized by an <i>in situ</i> sulfur deposition method. Three simple steps to synthesize binder/current collector-free sulfur-MWCNT composite cathodes: (i) dispersion of MWCNTs, (ii) sulfur nucleation (yellow) onto MWCNTs, and (iii) vacuum filtration, washing, and then drying .....	54
Figure 4.2: Thermogravimetric analysis of pristine MWCNTs and the self-weaving sulfur-MWCNT composites in flowing air with a heating rate of 10 °C/min, showing 40 wt. % sulfur in the S-CNT-A cathode and 63 wt. % sulfur in the S-CNT-B cathode .....	55
Figure 4.3: XRD patterns of pristine MWCNTs and the self-weaving sulfur-MWCNT composite cathodes. While the pristine MWCNTs show an amorphous structure, the sulfur in the composite cathodes is well-crystalline ...	56

Figure 4.4: SEM images and EDS mapping of the self-weaving sulfur-MWCNT composite (S-CNT-A) cathode: (a) High-resolution SEM image of MWCNTs in the S-CNT-A cathode, exhibiting the self-weaving behavior of winding MWCNTs, (b) surface morphology of the S-CNT-A cathode sample, and (c) elemental sulfur distribution in (b)57

Figure 4.5: Electrochemical measurements of the self-weaving sulfur-MWCNT composite cathodes: (a) Discharge/charge profiles of S-CNT-A at 1C rate, (b) CV plots of S-CNT-A at a scan rate of 0.3 mV/s between 2.8 and 1.5 V during the first 3 cycles, (c) first discharge/charge profiles of S-CNT-A at 1C, 2C, and 3C rates, (d) rate capability of the S-CNT-A cathode at various C rates, and (e) high-rate cycle performance (bottom half) and Coulombic efficiency (upper half) of the S-CNT-A cathode at 1C, 2C, and 3C rates for 100 cycles. The C rate is calculated based on the mass and theoretical specific capacity of sulfur ( $C = 1675 \text{ mA g}^{-1}$ ).  
 .....59

Figure 4.6: High-rate cycle performance of pure sulfur cathodes (carbon : sulfur = 3 : 2 by wt.) at 1C, 2C, and 3C rates. A severe capacity drop occurs after the first cycle.....62

Figure 4.7: High-rate cycle performance (bottom half) and Coulombic efficiency (upper half) of the S-CNT-B cathode at 0.5C, 1C, and 2C rates .....63

Figure 4.8: SEM images and EDS mapping of the S-CNT-A cathode after the 50<sup>th</sup> cycle at 2C rate: (a) High-resolution SEM image of the S-CNT-A cathode, where the active materials are captured into the interspaces of the MWCNT network (red arrows), (b) surface morphology of the cycled S-CNT-A cathode with a dense structure, and (c) elemental sulfur distribution in (b), revealing a homogeneous distribution of sulfur in the cathode and the structural stability after cycling .....65

Figure 5.1: A schematic cell configuration of rechargeable Li-S batteries: (a) traditional configuration with severe shuttle effect and Li<sub>2</sub>S poison problems and (b) new configuration with the MWCNT interlayer ..69

Figure 5.2: Scanning transmission electron microscopy (STEM) images of two different MWCNTs: (a) commercial MWCNTs with a straight tube structure and (b) as-synthesized MWCNTs with a curved tube structure used in this study.....70

Figure 5.3: Raman spectra of (a) commercial MWCNTs and (b) as-synthesized MWCNTs used in this study. The defect level of MWCNTs can be evaluated by the I<sub>D</sub>/I<sub>G</sub> ratio .....71

Figure 5.4: Electrochemical data of the Li-S cells: (a) cyclability of the cells at C/5 rate, (b) area-normalized Nyquist plots of the cells measured before cycling, (c) CV plots of the modified cell (first 10 cycles), and (d) discharge/charge profiles of the modified cell at 1C rate .....74

Figure 5.5: Morphology of the MWCNT paper: (a) before cycling and (b) after 100 cycles at 1C rate, (c) raw tube structure before cycling, (d) swollen tube structure after cycling, and (e) elemental mapping of (c).....76

Figure 5.6: V Morphology of the free-standing MWCNT paper covering sulfur electrodes after 50 cycles at C/2 rate, illustrating the embedding of the agglomerated active material within the MWCNTs .....	77
Figure 5.7: High-rate cycle performance and Coulombic efficiency of the lithium-sulfur cells with and without the MWCNT interlayer .....	78
Figure 5.8: Discharge/charge profiles of the Li/MWCNT interlayer/S battery with different electrolytes cycled at 1 C. The addition of LiNO <sub>3</sub> in the electrolyte improves the Coulombic efficiency (the ratio of discharge capacity to charge capacity) of lithium-sulfur cells up to 98% .....	79
Figure 6.1: Scheme and morphology of the MCP employed in the Li-S battery. (a) Schematic configuration of a Li-S cell with a bi-functional carbon interlayer with micropores inserted between the sulfur cathode and the separator, (b) SEM image of the surface of the MCP, and (c) TEM image of the microporous carbon particles. The scale bars in b and c represent, respectively, 500 and 10 nm.....	85
Figure 6.2: Nitrogen adsorption/desorption analysis, SEM images, and EDS mapping results of the MCP: (a) Isotherms and (b) pore size distributions of the microporous carbon powder, MCP, and MCP as an interlayer in the Li-S cell at 1C rate after 100 cycles. SEM images of the MCP (c) before cycling and (d) after cycling. Elemental mapping of (e) sulfur and (f) carbon in (d). The scale bars in c-f represent 50 nm.....	87

Figure 6.3: Electrochemical measurements of Li-S batteries: (a) EIS plots of Li-S cells with and without MCP, (b) CV scans, (c) discharge/charge profiles at various cycles, (d) rate capability up to 3C, and (e) cycle life and Coulombic efficiency of the cell with MCP at 1C and 2C for long cycles .....	90
Figure 7.1: SEM images of (a) MC, (b) BMC, and (c) interface between MC/BMC of the blended carbon interlayer; (d) high-magnification SEM and TEM (inset) images of BMC.....	97
Figure 7.2: SEM image of BMC covered by MC particles .....	98
Figure 7.3: Initial discharge plateau profile of the Li/blended carbon interlayer/S battery .....	99
Figure 7.4: (a) Discharge/charge plateau profiles with a cutoff voltage of 2.1 V; (b) CV curves under various scan rates; (c) CV plot at a scan rate of 2 mV s <sup>-1</sup> for 30 cycles.....	100
Figure 7.5: (a) Rate capability of the Li-S cells with and without the interlayer; (b) cyclability and (c) Coulombic efficiency of cells at different C rates; and (d) prolonged cycle performance at 10C and 15C rates .....	101
Figure 7.6: Initial discharge/charge profiles of the Li-S cells with and without the blended carbon interlayer.....	102
Figure 7.7: (a) Isotherms of MC, BMC, and the blended carbon interlayer before and after cycling; (b) pore size distributions of the blended carbon interlayer before and after cycling .....	103
Figure 7.8: Pore size distribution curves of MC, BMC, and the blended carbon interlayer .....	104

Figure 7.9: <i>Ex situ</i> SEM images of (a) the interlayer in discharged state and (b) the interlayer in charged state; EDX spectra of (c) the interlayer in discharged state and (d) the interlayer in charged state; XPS spectra of (e) the interlayer after discharging and (f) the interlayer after charging .....	105
Figure 7.10: XPS spectra of the blended carbon interlayer (BCI) after discharging and charging.....	107
Figure 7.11: XPS spectra of pure sulfur and lithium sulfide .....	107
Figure 8.1: (a) Typical discharge profile of the Li-S battery showing an upper plateau and a lower plateau with a total theoretical capacity of 1675 mAh g <sup>-1</sup> . (b) The strategic approach to recharge Li-S batteries: A full initial discharge followed by recharging and cycling within the solid-state region (the lower plateau). The lower plateau possesses a theoretical capacity of 1256 mAh g <sup>-1</sup> .....	112
Figure 8.2: (a) Cycle performance of the Li-S cells with the regular recharge setting (charged to 2.8 V) and the modified recharge setting (charged to 1000 or 600 mAh g <sup>-1</sup> ) at C/5 rate. (b) Discharge curves of the Li-S cells with the regular recharge setting at various cycles. (c) Discharge curves of the Li-S cells with the modified recharge setting (charged to 1000 mAh g <sup>-1</sup> ) at various cycles.....	117
Figure 8.3: The initial discharge curve of the Li-S cell with the microporous carbon interlayer at C/5 rate. The lower plateau capacity is 1064 mAh/g <sup>-1</sup> , which is about 85% of the theoretical capacity .....	118
Figure 8.4: XPS curves of (a) pristine sulfur and (b) pristine lithium sulfide. (2p <sub>3/2</sub> -sulfur: 163.7 eV; 2p <sub>3/2</sub> -lithium sulfide: 159.8 eV).....	120

Figure 8.5: (a) Discharge curve of the Li-S cell cycled at C/2 rate with the depth of discharge (DoD) indicated. XPS plots of the active material at (b) 16% DoD, (c) 34% DoD, (d) 74% DoD, and (e) 100% DoD. ( $2p_{3/2}$ -brown( $\text{Li}_2\text{S}_6$ ): 162.8 eV;  $2p_{3/2}$ -yellow( $\text{Li}_2\text{S}_4$ ): 161.2 eV; and  $2p_{3/2}$ -green( $\text{Li}_2\text{S}$ ): 159.8 eV) 121

Figure 8.6: The discharge reaction mechanism of a Li-S battery, which can be divided into three regions: the upper plateau, the sloping region, and the lower plateau. The former two are located in the dissolution region, and the latter is located in the solid-state region that provides highly reversible capacity and has only a negligible amount of polysulfide shuttle behavior.....123

Figure 8.7: Impact of  $\text{LiNO}_3$  additive in the electrolyte on battery performance at C/5 rate. The  $\text{LiNO}_3$ -free electrolyte is also suitable for the Li-S cell by utilizing the modified recharge setting .....124

Figure 8.8: SEM of the CNF electrode of the Li/dissolved polysulfide cell with (a) low magnification and (b) high magnification.....126

Figure 8.9: The initial discharge curve of the Li/dissolved polysulfide cell at C/5 rate. The starting active material is  $\text{Li}_2\text{S}_6$  instead of  $\text{S}_8$  .....126

Figure 8.10: (a) Cyclability, Coulombic efficiency, and (b) discharge curves of the Li/dissolved polysulfide cells using commercial CNF electrodes with the modified recharge setting (charged to  $700 \text{ mAh g}^{-1}$ ) at C/5 rate ....127

## Chapter 1: Introduction

### 1.1 RECHARGEABLE LITHIUM-SULFUR BATTERIES

Unlike the integrated circuit (IC) technology in semiconductor industry, batteries do not have an observed trend of performance doubling with a certain period like Moore's law.<sup>1</sup> After the first commercial lithium-ion (Li-ion) cell was released by Sony in 1991,<sup>2</sup> the progress in the rechargeable battery was not remarkably striking afterward. The major barrier to the development of high energy density battery technology lies in the limitation of the electrode materials, which determine the working voltage, capacity, and energy density of a battery.<sup>2-5</sup> Therefore, changing the battery chemistry from current lithium intercalation reactions in transition metal oxides or metal phosphates or graphite to other promising reactions is an inevitable means to boost the performance of Li-ion batteries.<sup>6</sup>

Lithium-sulfur (Li-S) batteries are regarded as one of the next-generation energy storage systems due to the extremely low-cost sulfur and their high energy density.<sup>6-8</sup> The price of sulfur per metric ton was as low as \$160 USD in 2012.<sup>9</sup> The theoretical capacity of sulfur is 1672 mA h g<sup>-1</sup> (calculated based on S<sup>0</sup> ↔ S<sup>2-</sup>). Coupled with the average operating voltage of a Li-S cell (2.15 V vs Li<sup>+</sup>/Li<sup>0</sup>) and the theoretical capacity of a pure lithium anode (3862 mA h g<sup>-1</sup>, calculated based on Li<sup>+</sup> ↔ Li<sup>0</sup>), the energy density can be estimated as high as ~2500 W h kg<sup>-1</sup>, which is an order of magnitude higher than that of traditional Li-ion batteries.

#### 1.1.1 Mechanism

Sulfur is in the form of polyatomic molecules with different structures, and octasulfur (cyclo-S<sub>8</sub>) is the most stable allotrope at room temperature. The electrochemical reactions occurring in the Li-S battery involve lithium, lithium ions (Li<sup>+</sup>),

sulfur, and polysulfide ions ( $S_n^{2-}$ ). The redox reactions can be written as follows. A discharge/charge current can be applied to the cell resulting in reduction/oxidation at the positive electrode and the oxidation/reduction at the negative electrode.

*Positive electrode:*



(forward direction: reduction/cathodic reaction; backward direction: oxidation/anodic reaction)

*Negative electrode:*



(forward direction: oxidation/anodic reaction; backward direction: reduction/cathodic reaction)

*Overall reaction:*



(forward direction: discharge reaction; backward direction: charge reaction)

These electrochemical reactions during cycling in an ideal Li-S cell without considering the impact of lithium polysulfide dissolution are illustrated in Figure 1.1.

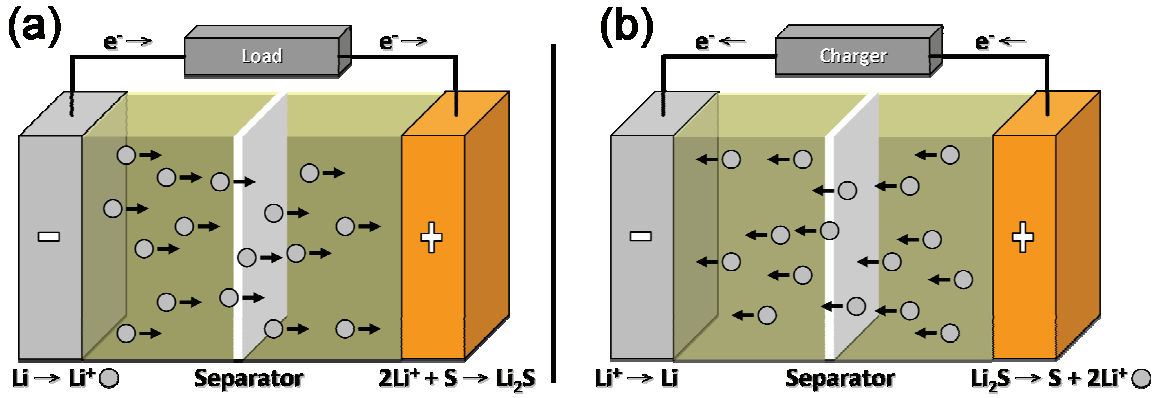


**Figure 1.1.** Schematic illustration of an ideal Li-S battery during (a) discharge and (b) charge.

However, in the real case, the above scheme may only represent the Li-S battery with solid-state electrolytes (all-solid-state design). The cathode reactions in Li-S batteries are displacement reactions, and several intermediate redox products ( $\text{Li}_2\text{S}_n$ ,  $n > 2$ ) formed are soluble in the liquid electrolyte, leading to serious side reactions and active material redistribution. A modified scheme is displayed in Figure 1.2.

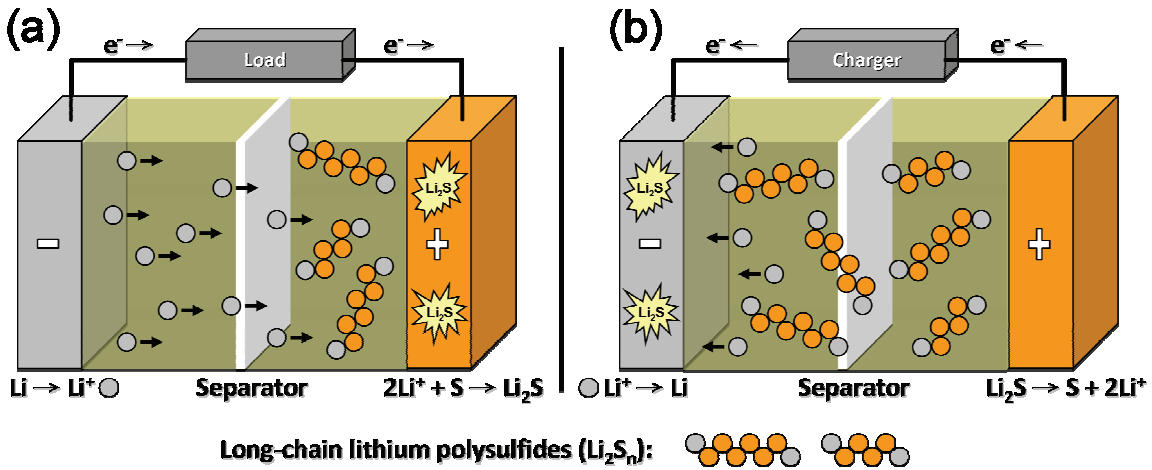


**Figure 1.2.** Schematic illustration of a Li-S battery with a liquid electrolyte during (a) discharge and (b) charge.

The discharge and charge profiles are shown in Figure 1.3. A typical discharge

curve at a moderate or high rate can be divided into three parts: the upper plateau, the sloping region, and the lower plateau. The predominant products of these three regions are, respectively,  $\text{Li}_2\text{S}_6$ ,  $\text{Li}_2\text{S}_4$ , and  $\text{Li}_2\text{S}$ .<sup>10</sup> The first two parts belong to the dissolution region, and the third part is ascribed to the solid-state region. At the initial stage of the first discharge, orthorhombic  $\alpha$ -sulfur combines with lithium ions and then transforms into  $\text{Li}_2\text{S}_6$ . Reduced polysulfide species keep dissolving in the electrolyte, which facilitates the utilization of inner sulfur due to its exposure to the electrolyte. Next, more long-chain polysulfides are produced, which thereby increase the viscosity of the electrolytes. When the electrolyte viscosity rises to a certain level, the lithium-ion transport will encounter some difficulties. Thus, the voltage drop in the sloping region reflects the concentration polarization (diffusion overpotential) in accordance with the increase in impedance.<sup>11, 12</sup>  $\text{Li}_2\text{S}$  was found to form in the beginning of the lower plateau,<sup>10</sup> which contributes to the major portion of the capacity with a fixed voltage. The electrochemical reactions during charge are reversed compared to that during discharge. A long flat lower plateau is seen firstly, representing the oxidation of  $\text{Li}_2\text{S}$  to polysulfides. The upper charge plateau, which is rather hard to define, indicates the oxidation reactions in the dissolution region. Crystalline sulfur has been detected at the end of recharge via *in operando* X-ray diffraction analysis.<sup>13</sup>

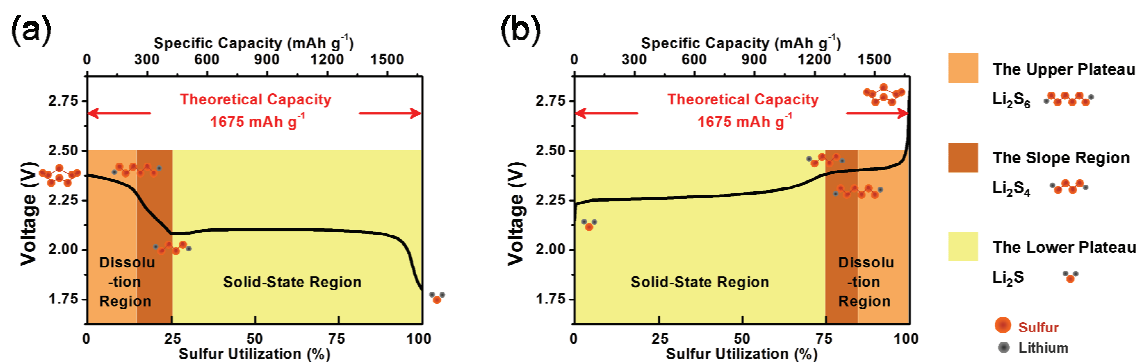


**Figure 1.3.** (a) Discharge profile and (b) charge profile of a fully utilized Li-S battery.

### 1.1.2 Applications

To keep the planet green, we need to take action to reduce the carbon footprint. Popularizing electric vehicles (EVs) is a common means that many governments are trying to do.<sup>14</sup> However, the cost, weight, size, driving duration, and safety concerns of the onboard Li-ion battery still hinder the promotion of EVs. For this reason, the Li-S battery seems a good fit due to its low-cost active material, environmental benignity, high gravimetric/volumetric energy density, and lower operation voltage.

Besides, the power of the battery employed in portable electronics like smart phones or laptops can be further improved. In most cases, the battery-user time of a smart phone is around a day, and that of a laptop is just a few hours. By utilizing the Li-S battery technology, the usage time of portable devices could be considerably enhanced at least by three times longer than that of present lithium-ion systems.

The Li-S battery can also be designed as a half-flow-mode cell with a tank of polysulfide catholyte at the cathode side.<sup>8</sup> This concept has recently been proved feasible with a membrane-free, semi-liquid cell configuration.<sup>15</sup> The redox flow Li-S cell is applicable to large-scale stationary energy storage for intermittent renewable energies

such as wind, solar, geothermal, and hydropower. In addition, this flow-type battery can be another potential solution for smart grid applications.<sup>16, 17</sup>

## **1.2 CHALLENGES OF LI-S BATTERIES**

Although Li-S batteries possess many advantages, low active material utilization, capacity degradation, self discharge, poor Coulombic efficiency, poor cycle life, and electrode volume expansion are still the challenges remaining with the Li-S cells.<sup>6-8</sup> These challenges are described in details in the following sections.

### **1.2.1 Insulating active materials**

Sulfur is an insulator with a very high electrical resistivity of  $2 \times 10^{23} \mu\Omega \text{ cm}$  at  $20 \text{ }^\circ\text{C}$ .<sup>18</sup> The end discharge product,  $\text{Li}_2\text{S}$ , is highly insulating as well. The high resistance causes Li-S cells to output low specific capacities (low active utilization). Conductive agents need to be appropriately added, and well-dispersed active material is desired to ensure smooth electron transport between the interfaces of conductor/active material.

### **1.2.2 Polysulfide dissolution**

As exhibited in Figure 1.2, the intermediate products from the electrochemical reactions, lithium polysulfides, can easily dissolve in the liquid electrolyte.<sup>19, 20</sup> The polysulfide dissolution can assist the utilization of active materials because the dissolved polysulfides ( $\text{Li}_2\text{S}_n$ ,  $n > 2$ ) can migrate freely to ensure intimate contact with conductive additives, yet insulating bulk sulfur and lithium sulfide cannot.<sup>21</sup> The dissolution behavior also brings numerous drawbacks. When the soluble polysulfides migrate out of the cathode region, they might not be re-utilizable, resulting in slow capacity fade during cycling.<sup>10</sup> These highly active polysulfides can further react with the electrolyte, depleting both active materials and solvent molecules.<sup>21, 22</sup> Other disadvantages like

self-discharge, shuttle effect, and  $\text{Li}_2\text{S}$  plating also originate from the polysulfide dissolution, which will be discussed next.

### **1.2.3 Self-discharge**

Self-discharge, another side effect resulting from the active material dissolution, is also an important issue in the Li-S battery systems. As the cell storage time increases, active sulfur located in the cathode structure reacts with the lithium ions in the electrolyte and, therefore, produces soluble lithium polysulfides, which could gradually diffuse out of the cathode. While self-discharge occurs, the open circuit voltage (OCV) of the cell declines and the upper discharge plateau around 2.3 – 2.4 V disappears,<sup>23-26</sup> implying the change in the oxidation state of the active material. An effective cell configuration that can prevent charged products from reacting with lithium ions and dissolving into the electrolyte is critical to avoid self-discharge in the Li-S battery.

### **1.2.4 Shuttle effect**

Due to the free movement of soluble polysulfides in the electrolyte, these “dissolved active materials” are able to migrate back and forth between the anode and cathode. This migration behavior is the so-called “shuttle effect,” which can result in anode corrosion and poor Coulombic efficiency,<sup>26-28</sup> and the dissolved polysulfides shuttle severely especially at the upper plateau region of the charge curve.<sup>26, 29, 30</sup> High-order polysulfides can migrate through the separator to the anode side and react with the lithium metal anode, and then convert into low-order polysulfides. The low-order polysulfides can diffuse backward to the cathode side and be re-oxidized to high-order polysulfides. This mechanism can go round and round, even until the cell is reaching over its theoretical capacity. Hence, extra energy is consumed for the shuttle movement in the Li-S battery, resulting in low Coloumbic efficiency. Novel cathode

structure designs and lithium anode passivation are widely adopted for the enhancement of Coulombic efficiency.

### **1.2.5 Li<sub>2</sub>S and sulfur plating**

The end products after cycling, Li<sub>2</sub>S and sulfur, can easily form thick and insulating layers covering the electrodes.<sup>27, 31-34</sup> This plating behavior may lead to the formation of some “inactive regions” in the cell, deteriorating the cyclability and battery performance; more seriously, it might cause cell failure if the agglomeration of Li<sub>2</sub>S/sulfur blocks the electron and ion transport in the electrode.<sup>31, 33</sup> Since the polysulfide dissolution is inevitable in the Li-S battery with a liquid electrolyte during the electrochemical reactions, appropriate pore distribution in the cathode matrix should be designed in order to trap the soluble polysulfide intermediates in the pores, which can avoid the active material agglomeration plating on the surface of the electrodes.

### **1.2.6 Volume expansion**

On account of the density difference between sulfur ( $\alpha$  phase, 2.07 g cm<sup>-3</sup>) and Li<sub>2</sub>S (1.66 g cm<sup>-3</sup>),<sup>18</sup> the volume change during cycling can be another problem for Li-S cells.<sup>35</sup> Severe volume expansion of the electrodes would lead to the failure of batteries due to huge crack formation. Flexible carbon materials can be used to buffer the volume change of the cathode. Utilizing partially-filled sulfur composites is also applicable to avoid the fracture of sulfur containers.

## **1.3 CATHODES FOR LI-S BATTERIES**

Since Ji *et al.* reported high specific capacity that can be realized by impregnating sulfur into a highly ordered mesoporous nano-sized carbon material in 2009 (Figure 1.4),<sup>36</sup> the Li-S battery system have drawn overwhelming research attention due to the thirst for high energy storage systems by the society. More than half of the research

studies have focused on the development of sulfur cathode structures to improve the cell performance.

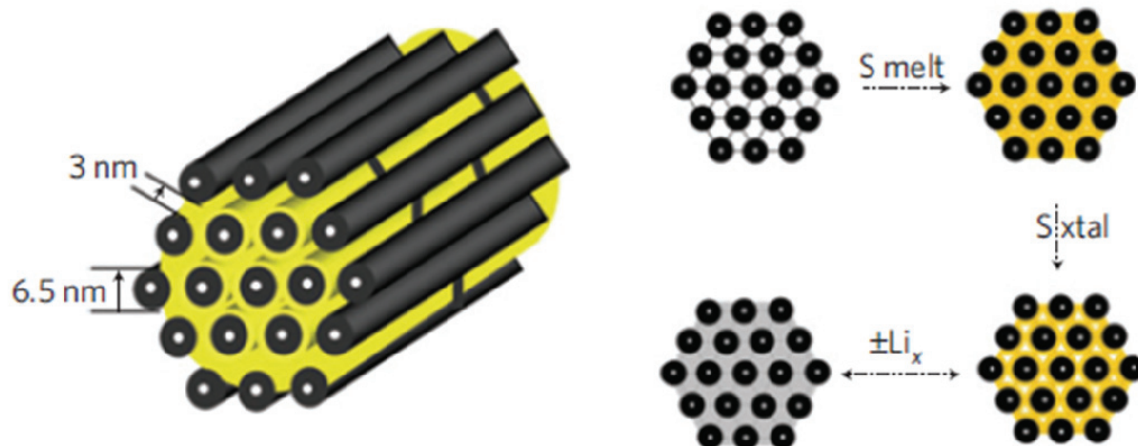


**Figure 1.4.** Illustration of sulfur confined in the interconnected pore structure of CMK-3, a mesoporous carbon, separated apart by carbon nanofibers. Reprinted from ref. 36.

### 1.3.1 Sulfur-carbon composites

Employing sulfur-carbon composites is the most common and effective way to improve the cathode performance. Carbon black,<sup>29, 37, 38</sup> microporous carbon,<sup>39, 40</sup> mesoporous carbon,<sup>41-43</sup> hierarchical porous carbon,<sup>36, 44-49</sup> hollow carbon spheres,<sup>50-52</sup> carbon nanotubes,<sup>53-60</sup> carbon nanofibers,<sup>61-64</sup> and graphene<sup>65-70</sup> have been employed as the host to accommodate active sulfur. Porous carbon substrates are regarded as the suitable matrix for the composite because of their absorbability of soluble polysulfides. The synthesis methods for sulfur-carbon composites can be classified as simple mixing,<sup>33</sup> ball-milling,<sup>53</sup> melting route,<sup>36, 37, 68, 71, 72</sup> sulfur vaporization,<sup>51</sup> solution-based synthesis,<sup>29, 38, 63, 67</sup> and dissolved polysulfide solution.<sup>30, 73</sup> Schuster *et al.*<sup>44</sup> showed that the cycle performance can be improved by removing external sulfur on the composites. Fu *et al.*<sup>73</sup> employed  $\text{Li}_2\text{S}_6$  dissolved polysulfide as an active material and a free-standing multi-wall

carbon nanotube (MWCNT) current collector, and highly reversible capacities were obtained because the dissolved active material can easily be fully utilized compared to the solid sulfur (Figure 1.5). Several studies showed that the initial phase, morphology, and distribution of the active material may only influence the first few cycles since solid sulfur is converted into lithium polysulfides, and then they freely migrate to other preferred locations, where they are thermodynamically stable, in the carbon structure.<sup>21, 74, 75</sup> Therefore, the carbon properties are the main factors to impact the cathode performance in the Li-S battery.

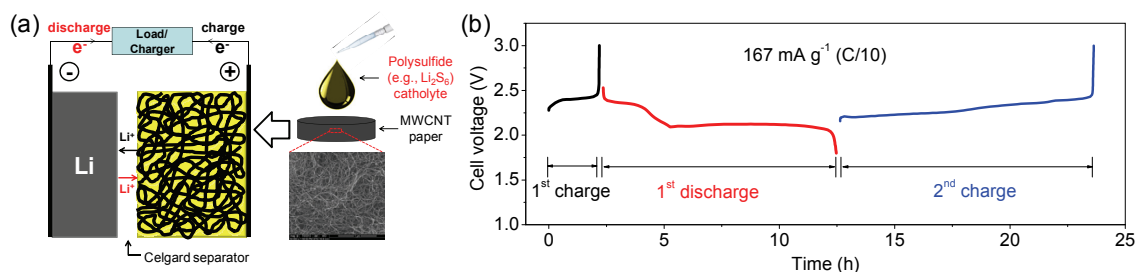


**Figure 1.5.** (a) The cell configuration of a Li/dissolved polysulfide cell and the addition of polysulfide catholyte into a MWCNT electrode. (b) Voltage vs. time profile of the cell at C/10 rate. Reproduced from ref. 73.

### 1.3.1.1 Porous carbon substrates

Porous carbon materials are frequently used to contain active sulfur and prevent polysulfides from dissolving into the electrolyte. The pore structure can be categorized into three types according to the pore size ( $d$ ): micropores ( $d < 2$  nm), mesopores ( $2$  nm  $< d < 50$  nm), and macropores ( $d > 50$  nm). Micropores were demonstrated as the ideal container for accommodating soluble polysulfides due to the small size.<sup>76</sup> Mesopores can promote lithium-ion transport because they offer abundant channels for the electrolyte at the cathode region.<sup>36, 45</sup> Macropores may be too large to securely store either the active material or electrolyte. Some network structures built from carbon nanotubes (CNTs) or

carbon nanofibers (CNFs) are able to suppress the polysulfide migration due to their high absorbability.<sup>59, 77</sup> Pore structures can also be introduced in CNTs and CNFs via various delicate synthesis methods to obtain improved cycle performance.<sup>60, 62, 63</sup>

### **1.3.1.2 Impact of pore structures**

To understand the impact of the pore size and pore volume of mesoporous carbon substrates on battery performance, a systematic study was carried out by Li *et al.*<sup>41</sup> It was found that the size of mesopores in the carbon does not have a great effect on the cyclability of Li-S cells when the mesopores are fully-filled, and the maximum sulfur loading is determined by the overall pore volume. However, partially-filled sulfur-mesoporous carbon composites are superior to fully-filled composite cathodes. This is because partially-filled composites can promote intimate contact between sulfur and mesoporous carbon, and space in the pores is needed for sufficient ion transport. However, mesopores are less efficient than micropores to trap soluble polysulfides since the size of polysulfide ions is closer to micropores. Our group is planning to investigate the relationship between micropore size and cycle performance from the sulfur-porous CNF composites with a series of micropores. The results will be reported in the future.

### **1.3.1.3 Binder-free cathodes**

In a typical slurry-casting procedure of making electrodes, polymer binders are constantly added to integrate carbon additives and active materials onto a current collector. Nonetheless, the addition of binders will decrease the overall energy density and somewhat reduce the electrode conductivity. Also, the solvent N-Methyl-2-pyrrolidone (NMP) used to dissolve and disperse the polyvinylidene fluoride (PVDF) binder was confirmed toxic.<sup>78</sup> Accordingly, the development of binder-free

cathodes can not only enhance the total energy density and electrode conductivity, but also eliminate the use of poisonous NMP.

Two major means are carried out to synthesize binder-free cathodes. One is inheriting the binder-free behavior from the pristine curly CNTs or CNFs, which form a free-standing paper right after filtration.<sup>75, 79, 80</sup> Sulfur needs to be pre-deposited onto the carbon substrates before vacuum filtration.<sup>59</sup> The carbon network of the binder-free cathode membrane can facilitate the lithium polysulfide absorption. Another way is employing a sheet of rigid carbon substrate that comprises pore structure.<sup>81, 82</sup> The carbon substrate is then co-heated with sulfur to make the sulfur melt permeate into the pores to form the composite.

#### **1.3.1.4 Graphene composites**

Graphene, a two-dimensional (2D) carbon monolayer that can be extracted from graphite, is regarded as an ultra-light, thin, and hard material with high conductivity, which has risen abruptly in the materials field in recent years.<sup>83</sup> The flexible characteristic of graphene renders it suitable to be the sulfur carrier in the Li-S battery.<sup>65-70</sup> The graphene in the composites coating or wrapping the sulfur can suppress the loss of active sulfur species due to the dissolution during cycling. The high electrical conductivity of graphene can improve the active material utilization as well.

#### **1.3.1.5 Surface functionalization**

To enhance the binding of sulfur to C-C bond, surface functionalization is a facile route to be conducted for carbon substrates.<sup>58, 66, 70, 84</sup> The functional groups work as a medium for the intimate connection between the soluble polysulfide intermediates and carbon surface. It was reported that carboxyl,<sup>58</sup> hydroxyl,<sup>66, 70, 84</sup> and epoxy<sup>66</sup> are favorable functional groups to enhance the cyclability of Li-S cells. Ji *et al.*<sup>66</sup> applied

graphene oxide as the carbon source, and both epoxy and hydroxyl groups could assist in immobilizing the active material during discharge/charge (Figure 1.6).

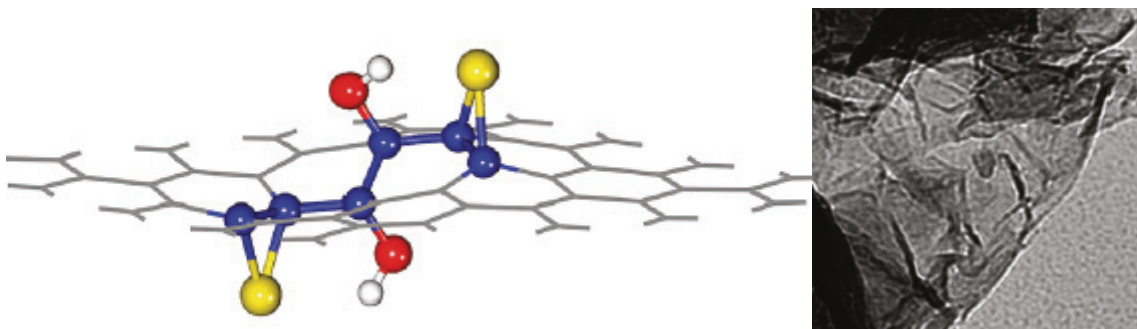


**Figure 1.6.** Scheme of sulfur immobilized on graphene oxide nanosheets. The enhanced binding of S to the C-C bond is due to epoxy or hydroxyl group. S atoms (yellow), oxygen atoms (red), hydrogen atoms (white), and bonded carbon atoms (blue) are highlighted. Reproduced from ref. 66.

### 1.3.2 Sulfur-polymer composites

Besides carbons, polymers are often seen in the literature to be used for the modification of sulfur cathodes. The polymers employed in Li-S system can be separated into two types: conducting polymers and non-conducting polymers. Conducting polymers such as polypyrrole (PPy),<sup>42, 85-89</sup> polyaniline (PANI),<sup>90, 91</sup> polythiophene (PT),<sup>92, 93</sup> and poly(3,4-ethylenedioxythiophene) (PEDOT),<sup>94</sup> can facilitate electron transport, improving the active material utilization. Moreover, the polymer coating works as a barrier to retard the polysulfide dissolution in the electrolyte. Non-conducting polymers, such as polyacrylonitrile (PAN),<sup>57, 95, 96</sup> polyvinylpyrrolidone (PVP),<sup>57, 94</sup> polyethylene glycol (PEG)<sup>36, 65, 36, 65</sup> and poly(propylene oxide) (PPO) & poly(ethylene oxide) (PEO) block copolymer,<sup>97</sup> were employed to offer a chemical gradient to suppress the out-diffusion of active polysulfide anions. A one-step, bottom-up synthesis method was designed by Li *et al.*<sup>94</sup> to obtain hollow sulfur nanospheres as the cathode composite

(Figure 1.7). Amphiphilic block copolymers comprise hydrophobic blocks and hydrophilic blocks. The hydrophobic end adheres to the hydrophobic sulfur, and the hydrophilic tail works as a chemical gradient.<sup>97</sup> In general, polymers in Li-S cells play a protective role to reduce the capacity fade by localizing the soluble polysulfides at the cathode region, whereas a certain amount of carbon additives/substrates is still critical to enhance the sulfur utilization and cyclability.<sup>36, 42, 57, 90, 94, 96-98</sup>



**Figure 1.7.** The formation mechanism of the one-step, bottom-up approach of PVP-encapsulated hollow S nanospheres. Reprinted from ref. 94.

### 1.3.3 Alternative composites

Not only carbons but also other materials could be applied to the composite synthesis with sulfur. If the alternative material only serves as an absorbing agent, the redox potential of the material must not overlap that of sulfur (1.5 V – 2.8 V vs. Li<sup>+</sup>/Li<sup>0</sup>) to prevent unwanted electrochemical reactions and structural change from the additives. The density and the addition of the alternative materials should not be too large; otherwise, this would deteriorate the energy density of the whole battery.

### 1.3.3.1 Metal oxide additives/composites

Various nano-sized metal oxides have been used as additives in sulfur composites, such as manganese nickel oxide,<sup>99, 100</sup> alumina,<sup>101</sup> silica,<sup>102</sup> and titanium oxide.<sup>103</sup> These nano additives function as adsorbing agents to improve cycle stability and reduce polysulfide shuttle. Seh *et al.*<sup>104</sup> designed a TiO<sub>2</sub>-sulfur yolk-shell composite that exhibits prolonged cyclability over 1000 cycles (Figure 1.8), showing that metal oxides might replace a portion of carbon to trap polysulfides, although the sulfur loading needs to be further increased for practical use. The idea of the yolk-shell structure is to avoid the fracture of the TiO<sub>2</sub> spheres during the volume expansion of the active material, which could lead to serious leakage of polysulfides. Extra void or pore space remained in the cathode structure is desirable not only to retain the dissolved polysulfides, but also cushion the volume change during discharge/charge.

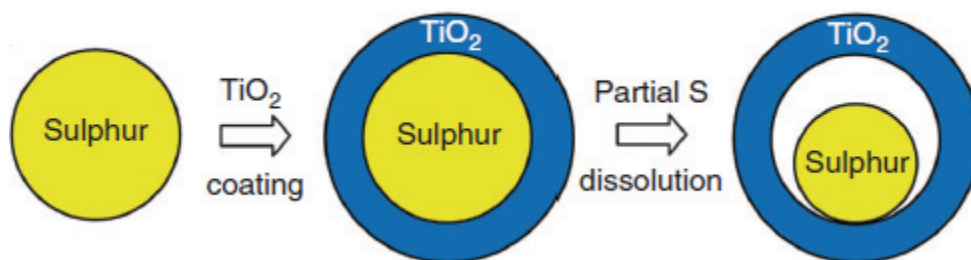


**Figure 1.8.** Schematic fabrication process to form TiO<sub>2</sub>-sulfur yolk-shell nanostructure. Reprinted from ref. 104.

### 1.3.3.2 Intercalation compound composites

We have proposed employing several mid-voltage intercalation compounds that possess similar redox potential as that of sulfur to contribute additional capacity for the Li-S battery. Some of them have been investigated in our lab and will be published elsewhere.<sup>105</sup> VO<sub>2</sub>-B was found to exhibit severe capacity degradation in the ether electrolyte, so it is unsuitable to be combined with sulfur as the cathode composite. On

the contrary,  $\text{TiS}_2$  works normally in the glyme-based electrolyte just like that in the carbonate-based electrolyte. The sulfur- $\text{TiS}_2$  composite material can deliver a higher capacity than sulfur-carbon composites when they have the same sulfur content, but the increased capacity is even higher than  $\text{TiS}_2$  can output. The reason is that  $\text{TiS}_2$  is a good conductor,<sup>2, 106</sup> which can enhance the sulfur utilization, leading to a better overall specific capacity. Furthermore, micron-sized  $\text{TiS}_2$  particles serve as many anchor points during cycling, thereby stabilizing the structure integrity of the electrode. Future work can focus on generating appropriate pore structure in suitable intercalation compounds for advancing the performance of sulfur composites.

### **1.3.3.3 Metal coatings**

Coating a monolayer or a thin layer of metal is another approach to make sulfur composites. Compared to carbon, metals have higher electrical conductivity and malleability. The disadvantage of weight increase from metal additives can be reduced by using coating techniques. Electroless coatings can be employed to synthesis core-shell sulfur composite with many different metal choices such as nickel, copper, palladium, cobalt, alloys, and so on. The coating layer can serve as electron transport pathways and a protective barrier for active sulfur.

### **1.3.4 $\text{Li}_2\text{S}$ as the cathode material**

Although there are several advantages to use Li-S system as energy storage devices, employing highly active lithium metal as anode still brings safety concerns. In this regard, one way is to use  $\text{Li}_2\text{S}$  as the starting cathode material which has a theoretical capacity of  $1166 \text{ mA h g}^{-1}$ . When the cathode is lithiated, other lithium-free high energy anodes (e.g., silicon and tin) could be used to substitute lithium metal anode.

Recent studies show that  $\text{Li}_2\text{S}$  can be reversible in electrochemical reactions.<sup>107-112</sup> Yang *et al.*<sup>107</sup> discovered that large energy barrier/overpotential was found when charging the  $\text{Li}_2\text{S}$  cathode because of the sluggish oxidation of solid-state bulk  $\text{Li}_2\text{S}$  (Figure 1.9). The charge transfer between  $\text{Li}_2\text{S}$  and the electrolyte and lithium-ion diffusion in  $\text{Li}_2\text{S}$  are kinetically slow. Uniform  $\text{Li}_2\text{S}$  distribution can be carried out by bonding lithium and nitrile groups in PAN.<sup>113</sup>  $\text{Si}/\text{Li}_2\text{S}$  and  $\text{Sn}/\text{Li}_2\text{S}$  systems were demonstrated as full cells without any lithium metal anodes.<sup>107-109</sup> Moreover, high active material utilization was realized with a design of  $\text{Li}_2\text{S}/\text{CNTs}$  sandwiched structure, showing the potential of  $\text{Li}_2\text{S}$  for practical applications.<sup>112</sup> The research focus on non-Li anode/ $\text{Li}_2\text{S}$  battery is still relatively limited in comparison with that on sulfur cathodes, and more research results are needed to evaluate the practicality of this system.

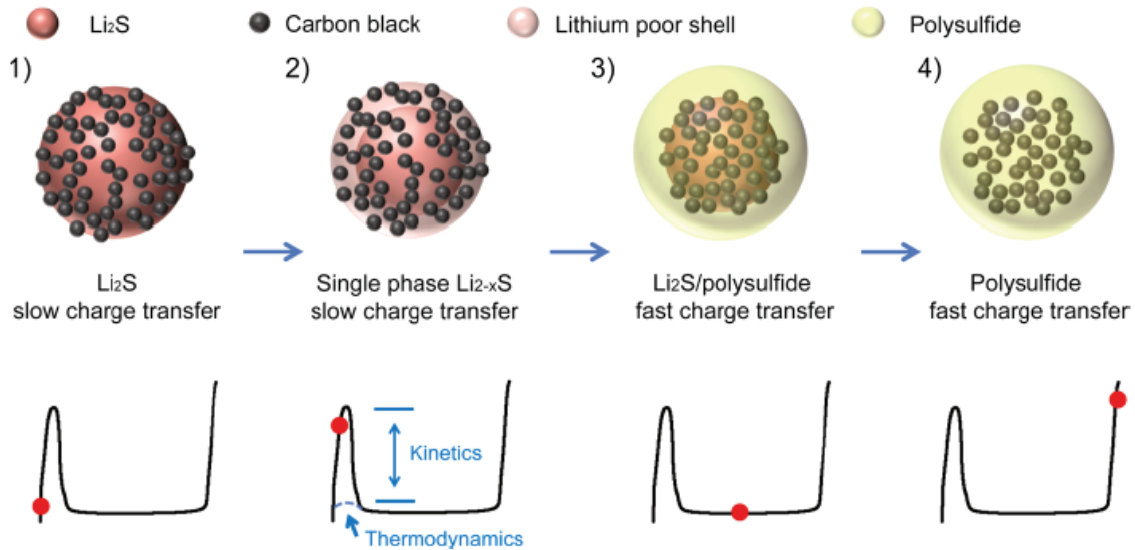


**Figure 1.9.** The model for the initial charging of  $\text{Li}_2\text{S}$  with slow kinetics. Reprinted from ref. 107.

### 1.3.5 Current collectors

In most cases, aluminum foil is widely used as the current collector for all types of lithium batteries. However, the structure of sulfur cathodes changes a lot during cycling because of the repeated dissolution and precipitation of active material. A three-dimensional (3D) current collector can offer additional benefit for loading high amounts of sulfur and providing abundant absorbing points for soluble polysulfides. The 3D conductive network can improve the contact between active material and current collector as well. Some foam materials made of carbon and nickel have been studied, which exhibit better cyclability than 2D Al current collector,<sup>114-116</sup> but the electrode weight gained could decrease the overall energy density, eliminating the merit of using sulfur as the cathode.

### 1.3.6 Binders

Employing advanced binders could be another approach to enhance the cycle performance even though the amount of binder in the electrode is usually low. Important requirements for a binder used in the battery are dispersible in solvents, electrochemically stable within the working voltage window, and inert with the electrolyte and active material. Polytetrafluoroethylene (PTFE), polyethylene oxide (PEO), and PVDF are commonly added in the electrode to provide sufficient adhesion between the interfaces of the active material, conductive agents, and current collector. To get rid of harmful NMP solvent, water-soluble binders are developed to replace traditional binders.<sup>117-122</sup> A Carbonyl- $\beta$ -Cyclodextrin was developed with strong bonding capability and good mechanical property, which suppresses active material aggregation efficiently compared to other common binders.<sup>122</sup> The water solubility was introduced after the precursor was treated with H<sub>2</sub>O<sub>2</sub>, and free hydroxyl groups formed due to the oxidation of C(2)OH.

High shear strength is also obtained due to the connection between intermolecular hydrogen bonds, leading to the strong bonding behavior.

#### **1.4 SEPARATORS FOR LI-S BATTERIES**

Since commercial polymeric separators are widely used as permeable membranes for liquid electrolytes in the battery, which work well to prevent short circuit and permit lithium-ion penetration. However, the separators cannot block the transport of polysulfide anions which result in the “shuttle effect”. Su and Manthiram<sup>75, 76, 84, 123</sup> conceived an idea of inserting a bi-functional interlayer between the separator and cathode, and the pores/carbon network can effectively capture the polysulfide intermediates (Figure 1.10). The interlayer not only serves as a polysulfide stockroom, but also offers additional electron paths covering the top surface of the cathode, leading to superior battery performance. Here the carbon interlayer can be regarded as another kind of separator to block the penetration of soluble polysulfides, resulting in less shuttle effect and better capacity retention. In the future, integrated separators should be specially designed for Li-S cells to allow lithium ion flow but hinder polysulfide migration.

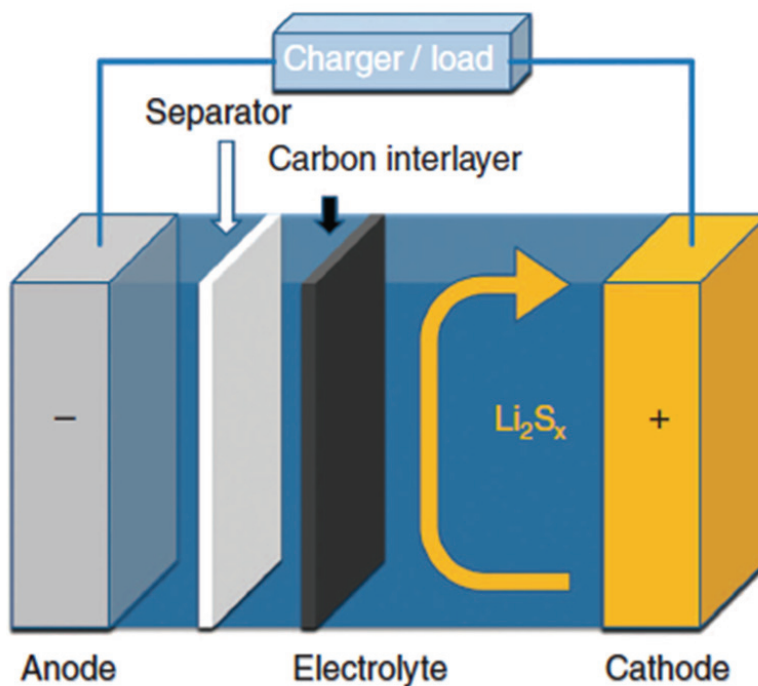


**Figure 1.10.** The cell configuration of the Li-S battery with a bi-functional carbon interlayer that can reduce the charge-transfer resistance and capture unstable, migrating polysulfides. Reprinted from ref. 76.

## 1.5 ELECTROLYTES FOR LI-S BATTERIES

Electrolyte systems in Li-S cells also play a critical role to influence the battery performance. Zhang<sup>21</sup> has already published a complete review paper to expound the liquid electrolyte employed in the Li-S system. Not all of the electrolytes fit the Li-S battery due to the existence of highly reactive polysulfide anions. Besides, non-liquid electrolytes like gel polymer and solid-state electrolyte exhibit some progress in this field.

### 1.5.1 Liquid-phase electrolytes

The mainstream Li-S battery research mostly adopts low viscosity ethers such as 1,3-dioxolane (DOL) and 1,2-dimethoxy ethane (DME) as the electrolyte solvents.<sup>22</sup>

DME possesses higher polysulfide solubility than DOL, but DME is reactive with lithium metal anode. DOL can help the anode surface form a solid electrolyte interface (SEI).<sup>22, 34</sup> Employing only one of the solvents alone results poor cycle performance.<sup>22, 124, 125</sup> By mixing the two solvents together, synergistic benefit is shown on the active material utilization and cyclability of the Li-S battery.

Carbonates (*e.g.*, ethylene carbonate and diethyl carbonate) were regarded as inapplicable electrolyte systems for Li-S cells because of their low polysulfide solubility and high reactivity with reduced sulfur species.<sup>126</sup> Polysulfides react with carbonates irreversibly during cycling, leading to the unwanted consumption of active material. Nevertheless, Xin *et al.*<sup>39</sup> showed that the sulfur cathode works perfectly with the carbonate-based electrolytes when the smaller sulfur molecules are confined in a state-of-the-art conductive microporous carbon matrix. Encapsulating sulfur in the micropores of carbon substrates seems applicable for carbonates to be used in the Li-S battery.<sup>40, 127, 128</sup> Since sulfur is trapped within the pores less than 2 nm, long-chain polysulfides and large sulfur particles may not form. This might lead to the disappearance of the upper plateau, which represents the dissolution region of the electrochemical reaction in the Li-S system.<sup>10, 21</sup> Single discharge/charge plateau is seen with the Li-S batteries that employ carbonate-based electrolytes,<sup>39, 40, 127, 128</sup> but further in-depth investigation is still needed to confirm the redox reaction mechanism of sulfur species in carbonates.

### 1.5.2 Lithium salts for electrolytes

$\text{LiCF}_3\text{SO}_3$ ,  $\text{LiN}(\text{CF}_3\text{SO}_2)_2$  (LITFSI), and  $\text{LiClO}_4$  are common lithium salts added into the organic solvent to prepare the electrolytes for Li-S cells. These three salts only have slight impact on the battery performance.<sup>126</sup> Other conventional salts like  $\text{LiPF}_6$  and

LiBF<sub>4</sub> are inappropriate because they react with lithium polysulfides and induce ring-opening polymerization of DOL solvent.<sup>21</sup> LiNO<sub>3</sub> is a popular co-salt for the electrolyte because a small amount can significantly improve the Coulombic efficiency.<sup>129</sup> The addition of LiNO<sub>3</sub> in the electrolyte can passivate the lithium anode to avoid the attack from the reactive polysulfides.<sup>34, 130</sup> However, the use of LiClO<sub>4</sub> or LiNO<sub>3</sub> remains a concern due to their highly oxidative property.<sup>21</sup> A solvent-in-salt concept was carried out by dissolving a large amount of LITFSI salts into the DOL/DME co-solvents in the report from Suo *et al.*<sup>131</sup> (Figure 1.11). This saturated electrolyte can hinder the polysulfide dissolution during cycling, resulting in stable capacity output and high Coulombic efficiency.

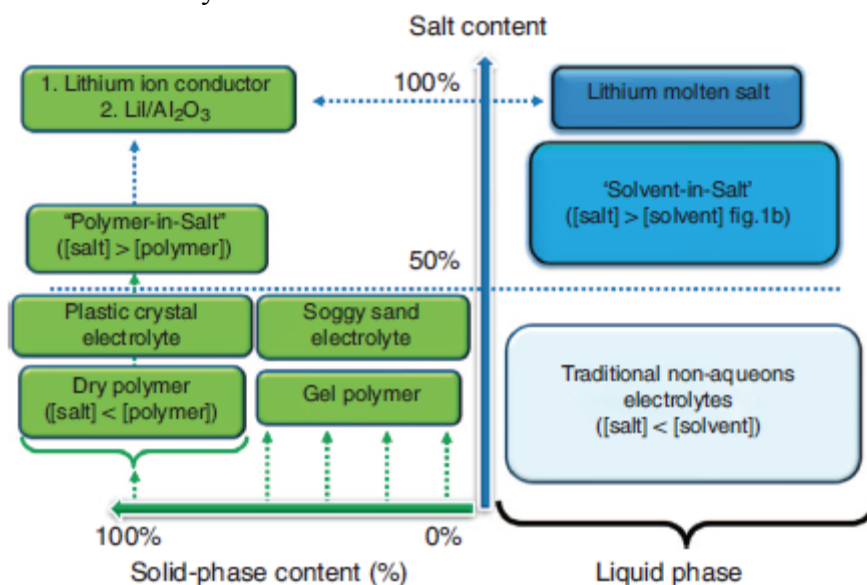


**Figure 1.11.** Overview of solid-state-based and liquid-based electrolytes. Solvent-in-salt belongs to liquid phase but with a salt content of > 50%. Reprinted from ref. 131.

### 1.5.3 Ionic liquid electrolytes

Room-temperature ionic liquids (RTILs) are less volatile, non-flammable, and electrochemically stable solvents for the electrolyte in electrochemical devices.<sup>132, 133</sup>

N-methyl-N-butyl-piperidinium,<sup>134</sup> 1-ethyl-3-methylimidazolium  
bis(trifluoromethanesulfonyl)imide,<sup>135</sup>  
N,N-diethyl-N-methyl-N-(2-methoxyethyl)ammonium  
bis(trifluoromethanesulfonyl)amide,<sup>136</sup> and N-methyl-N-allylpyrrolidinium  
bis(trifluoromethanesulfonyl)imide<sup>137</sup> were demonstrated to be applicable RTILs for Li-S  
cells. Another ionic liquid, N-methyl-N-propylpyrrolidinium bis(trifluoro  
methanesulfonyl)imide, needs to be heated to 50 °C to gain sufficiently low viscosity to  
serve as the electrolyte solvent.<sup>138</sup>

#### 1.5.4 Gel polymer/solid-state electrolytes

Gel polymer and solid state electrolytes are also potential candidates for the  
electrolyte in Li-S cells. Soluble polysulfides are difficult to migrate in the high-viscosity  
gel electrolytes and solid-state electrolytes, which could decrease the loss of active  
material and restrain shuttle effect. Poly(vinylidene fluoride-co-hexafluoropropylene)<sup>71</sup>  
and PEO<sub>20</sub>LiCF<sub>3</sub>SO<sub>3</sub> + 10% ZrO<sub>2</sub><sup>109, 139</sup> electrolyte have been tested with the Li-S battery  
systems as gel electrolytes. Various glass ceramics are used as the solid-state electrolytes,  
such as Li<sub>2</sub>S-P<sub>2</sub>S<sub>5</sub><sup>140-142</sup> and Li<sub>2</sub>S-GeS<sub>2</sub>-P<sub>2</sub>S<sub>5</sub><sup>143</sup> glass compounds. These electrolytes make  
all-solid-state Li-S battery possible, but lower ionic conductivity might sacrifice the rate  
capability of the cell.

#### 1.6 ANODES FOR LI-S BATTERIES

Compared to cathodes and electrolytes, less attention has been paid to the  
modification of lithium metal anodes. An early research applied a 10 µm coating layer on  
the lithium anode by the UV curing method, resulting in overcharge-free behavior.<sup>144</sup>  
Lithiated silicon was also prepared by either directly contacted with lithium foil<sup>145</sup> or  
electrochemical lithiation in a Li-Si half cell.<sup>137</sup> Other high energy metal oxide anodes

coupled with the  $\text{Li}_2\text{S}$  cathode have been introduced in section 1.3.4 before.

### 1.7 WORKING TEMPERATURES FOR LI-S BATTERIES

To understand the effect of temperature on Li-S batteries, low and high testing temperatures were applied while cells were cycling.<sup>69, 146, 147</sup> The performance of Li-S cells at low temperature was worse than that at room temperature, and the battery at  $-40^\circ\text{C}$  with a low current rate exhibited five separate plateaus rather than two plateaus usually found at room temperature.<sup>146</sup> The polysulfide intermediates at low temperature seem “frozen”, and each electrochemical reaction could be observed independently. High-temperature performance of the Li-S battery is somewhat poor in comparison with room-temperature performance.<sup>69</sup> The reason might be the serious active material dissolution strengthened at high temperature.

### 1.8 WORKING VOLTAGE WINDOWS FOR LI-S BATTERIES

In most cases, the Li-S batteries are operated within a voltage window of 1.5 V – 3.0 V. Two discharge plateaus and two charge plateaus can be seen at moderate C rates in ether-based electrolytes. However, the kinetics of the upper and the lower plateau are quite distinct. The upper plateau involves the transformation from sulfur to long-chain polysulfides, and this step is very fast.<sup>36</sup> By utilizing only the upper plateau, the rate capability of the Li-S battery can be very high ( $6.3 \text{ A g}^{-1}$ ) with stable cyclability.<sup>123</sup> A Li-S flow cell without the ion-selective membrane was designed by adopting the same strategy, and  $\text{Li}_2\text{S}_8$  served as a catholyte in the cell, delivering steady energy for more than 2000 cycles.<sup>15</sup>

The lower plateau, which is slow in kinetics, involves the electrochemical reaction to generate solid  $\text{Li}_2\text{S}$  from the  $\text{Li}_2\text{S}_4$  produced at the end of the upper plateau. Su *et al.*<sup>10</sup> conceived a recharge approach to control the charge capacity for only utilizing the lower plateau at  $\sim 2 \text{ V}$  (Figure 1.12). Thus, the redox reaction can be confined in the

solid-stage region, leading to highly reversible capacity output for extended cycles. The cyclability with an extremely low capacity degradation rate of 0.002% per cycle up to 500 cycles can be obtained. Additionally, high Coulombic efficiency can be realized even without the addition of  $\text{LiNO}_3$  in the electrolyte.

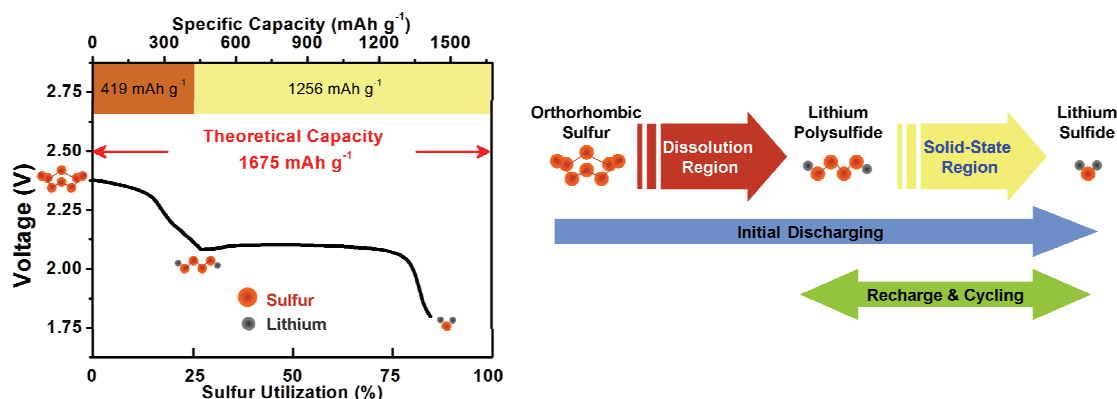


**Figure 1.12.** Schematic diagrams illustrating the recharge strategy for elongating the cycle life of Li-S cells. Reprinted from ref. 10.

## 1.9 OBJECTIVES FOR THIS DISSERTATION

The primary objectives of my dissertation are to solve the issues persistently remaining with Li-S batteries. The most critical challenge is the polysulfide dissolution and migration during cycling. Novel materials designs, new cell configurations, and recharge strategy are adopted to tackle the problem originated from soluble polysulfides. Accordingly, after describing the general experimental methods in Chapter 2, Chapter 3 introduces a facile *in-situ* sulfur deposition route to synthesize sulfur-carbon composites that have a carbon-wrapped sulfur structure, which can not only enhance the active material utilization but also improve the capacity retention.

A self-weaving sulfur-CNT composite made by a one-step synthesis and self-assembly behavior is shown in Chapter 4. High-rate capability and superior

cyclability are obtained due to the highly conductive CNT network, which offers abundant electron pathways and traps dissolved active material. In addition, this composite is binder-free, which could eliminate the use of toxic NMP solvent during regular electrode fabrication in Li-ion battery industry.

A new cell configuration for Li-S cells is presented in Chapters 5 & 6. In chapter 5, a free-standing MWCNT paper serves as an interlayer between the separator and cathode, functioning like a pseudo-upper current collector. As the self-weaving sulfur-CNT cathode, MWCNT as the interlayer also captures unstable polysulfides migrating from the cathode region, suppressing the loss of sulfur species. An advanced microporous bi-functional carbon interlayer is presented in Chapter 6, showing excellent cyclability for prolonged cycles. Micropores work as “polysulfide stockrooms” to ensure dissolved polysulfide anions are trapped, and these trapped polysulfide intermediates can still be reutilized in the following cycles.

Novel recharge strategies are pursued in Chapter 7 & 8. The upper plateau possesses high-rate capability, and ultra-high-rate Li-S battery can be realized by discharging/charging within the upper plateau, which can be seen in Chapter 7. This recharge operation is the origin to successfully carry out Li-S flow cell as well. Chapter 8 shows the original recharge setting to utilize only the 2 V lower plateau, leading to excellent cycle performance for over 500 cycles and extraordinarily low capacity fade. By applying this recharge strategy, LiNO<sub>3</sub>-free electrolyte could be used in the Li-S battery to get high Coulombic efficiency due to the limited production of long-chain polysulfides. Last but not least, the summary of these approaches is presented in Chapter 9.

## **Chapter 2: General experimental procedures**

### **2.1 MATERIALS SYNTHESIS**

Pristine sulfur was synthesized by mixing sodium thiosulfate ( $\text{Na}_2\text{S}_2\text{O}_3$ ; Fisher scientific) and hydrochloric acid (HCl; Fisher Scientific) in aqueous solution overnight under strong stirring, followed by filtering and washing the precipitate formed until the pH reached 7. The sulfur powder was dried overnight at 50 °C in an air-oven before use. Pristine MWCNTs were synthesized by a chemical vapor deposition (CVD) process. Microporous carbon (Black Pearl 2000; Cabot) was used as purchased. The detailed synthesis procedures will be described in the respective chapters.

### **2.2 MATERIALS CHARACTERIZATION**

The materials employed in the experiments were characterized by the following techniques. The specific characterization procedures will be described in the respective chapters.

#### **2.2.1 X-ray diffraction (XRD)**

XRD data were collected with a Philips X-ray Diffractometer (PW 1830 + APD 3520) with Cu  $K\alpha$  radiation. The phase in the collected XRD data was identified with the JCPDS files.

#### **2.2.2 Thermogravimetric analysis (TGA)**

The amount of sulfur in the composites was determined by TGA with a Perkin-Elmer TGA 7 Thermogravimetric Analyzer at a fixed heating rate in flowing air.

### **2.2.3 Scanning electron microscopy (SEM) and Transmission electron microscopy (TEM)**

The morphology of the samples was investigated with a JEOL LSM-5610 SEM, a FEI Quanta 650 SEM, a Hitachi S-5500 SEM equipped with a scanning transmission electron microscope (STEM), and a JEOL 2010F high-resolution TEM.

### **2.2.4 Energy dispersive X-ray spectroscopy (EDS)**

The elemental composition and mapping results of the samples were determined with an EDS attached to the SEM/TEM instrument.

### **2.2.5 Surface area and pore size measurements**

Multi-point Brunauer–Emmett–Teller (BET) surface area measurements were carried out with a volumetric sorption analyzer (NOVA 2000, Quantachrome) using physical adsorption/desorption of nitrogen gas at the liquid-nitrogen temperature. Pore size distributions were calculated according to the Barrett–Joyner–Halenda (BJH) method. Micropore surface area and volume were estimated by the t-plot method.

### **2.2.6 Raman spectroscopy**

A Raman microscope (Renishaw, inVia Reflex) with a 514.5 nm green laser and a  $50\times$  aperture was employed to obtain the Raman scattering spectra.

### **2.2.7 X-ray photoelectron spectroscopy (XPS)**

The samples were examined by XPS with a Kratos Axis Ultra spectrometer (Kratos Analytical) utilizing a monochromated Al K $\alpha$  X-ray source ( $h\nu = 1486.5$  eV) and a 45° take-off angle. The pressure in the analysis chamber was typically  $2 \times 10^{-9}$  torr during data acquisition. All spectra were fitted with Gaussian-Lorentzian (30% Gaussian) functions and a Shirley-type background by the deconvolution software (CasaXPS, Casa Software).

## **2.3 ELECTROCHEMICAL CHARACTERIZATION**

### **2.3.1 Cell assembly**

Electrochemical properties of the synthesized samples were evaluated with coin cells with lithium metal as a counter electrode. Sulfur cathode slurry was fabricated by mixing sulfur or the composite materials, carbon black (Super P), and polyvinylidene fluoride (PVDF; Kureha) binder in an *N*-methylpyrrolidinone (NMP; Sigma-Aldrich) solution overnight. The slurry was tape-casted onto an aluminum foil and dried in an air-oven overnight at 50 °C, followed by roll-pressing and cutting into circular electrodes. The cathode disks were dried in a vacuum oven for an hour at 50 °C before assembling the cell. The electrolyte was prepared by adding a certain amount of LiCF<sub>3</sub>SO<sub>3</sub> (Acros Organics) and LiNO<sub>3</sub> (Acros Organics) salts into a mixture of 1,2-Dimethoxyethane (DME; Acros Organics) and 1,3-Dioxolane (DOL; Acros Organics) at a 1:1 volume ratio. CR2032 coin cells were assembled with the sulfur cathodes, prepared electrolyte, interlayers (if any), polypropylene separators (Celgard), and lithium foil anodes (Aldrich).

### **2.3.2 Cycle performance and rate capability test**

All electrochemical cycling tests were performed with an Arbin battery cycler. Different voltage windows and current rates were used depending upon the experimental settings. Cycle performances were evaluated by discharging and charging the cells at a fixed current density within a fixed voltage window or charge capacity. Rate capability tests were evaluated by cycling the cells at various C rates within a fixed voltage window.

### **2.3.3 Cyclic voltammograms (CV)**

CV plots were collected with a VoltaLab PGZ 402 Potentiostat at a fixed scan rate within a fixed voltage window.

### **2.3.4 Electrochemical impedance spectroscopy (EIS)**

EIS data were obtained with a Solartron Impedance Analyzer (SI 1260 + SI 1287) from 1 MHz to 100 mHz with an AC voltage amplitude of 5 mV at the open-circuit voltage of the cells with the Li metal foil as both auxiliary and reference electrodes.

## **Chapter 3: A facile *in situ* sulfur deposition route to obtain carbon-wrapped sulfur composite cathodes for lithium-sulfur batteries**

### **3.1 INTRODUCTION**

Lithium-ion batteries have revolutionized the portable electronics industry over the past two decades, and there is immense interest to adopt lithium-ion batteries for electric vehicle applications and stationary storage of renewable energies such as solar and wind energy. For employing the lithium-ion battery technology for these applications, several important criteria such as energy density, power density, rate capability, cycle life, cost, and safety need to be considered. The current lithium-ion battery technology is based on insertion compound cathodes and anodes and is limited in energy density. They also suffer from safety concerns arising from the chemical instability of the oxide cathodes under conditions of overcharge and the high cost associated with expensive transition metals like Co.<sup>4, 5, 148</sup> Accordingly, there is immense interest to develop alternate cathode materials for lithium-ion batteries. In this regard, sulfur is an attractive cathode candidate as it offers an order of magnitude higher theoretical capacity (1675 mAh g<sup>-1</sup>) than the currently employed cathodes (< 200 mAh g<sup>-1</sup>) and operates at a safer voltage range (1.5 – 2.5 V).<sup>5, 148</sup> In addition, sulfur is abundant and inexpensive.

However, the major issue facing the sulfur cathode is its poor cycle life. The discharge process of sulfur cathodes involves the formation of intermediate polysulfide ions, which dissolve easily in the electrolyte during the charge/discharge process and result in an irreversible loss of active material during cycling;<sup>5, 20, 25, 148, 149</sup> the higher-order polysulfides (Li<sub>2</sub>S<sub>n</sub><sup>2-</sup>, 4 ≤ n ≤ 8) produced during the initial stage of the discharge process are soluble in the electrolyte and move toward the lithium metal anode,

where they are reduced to lower-order polysulfides.<sup>26, 27</sup> The formation of the final discharge product  $\text{Li}_2\text{S}$  involves the plating of dense layers on the cathode surface, which blocks the penetration of lithium ions and the transfer of electrons or even breaks the integrity of the cathode structure, leading to poor cyclability.<sup>31, 32</sup> Moreover, sulfur is an insulator with a resistivity of  $5 \times 10^{-30} \text{ S cm}^{-1}$  at  $25 \text{ }^\circ\text{C}$ ,<sup>18</sup> resulting in a poor electrochemical utilization of the active material. Although the addition of conductive carbon could improve the overall electrode conductivity, the core of sulfur particles which have little or no contact with conductive carbon will still be highly resistive. In this regard, improving the conductivity by increasing the fraction of sulfur in contact with carbon is critical. Additionally, the loss of active material from the dissolution of polysulfides should be avoided or suppressed during the charge/discharge process.

Several approaches have been pursued to overcome these problems, such as forming sulfur-carbon composites with carbon black or nanostructured carbon that have led to much improved performances.<sup>36-38, 40, 51, 60, 71, 77, 150, 151</sup> For example, a mesoporous carbon framework filled with amorphous sulfur with the addition of polymer has been found to exhibit a high reversible capacity of approximately  $1000 \text{ mAh g}^{-1}$  after 20 cycles.<sup>36</sup> However, most traditional methods to synthesize sulfur-carbon composites include processing by a sulfur melting route,<sup>36, 37, 40, 60, 71, 77, 150, 151</sup> resulting in high manufacturing costs due to additional energy consumption. Also, several reports have noted that the sulfur content in the sulfur-carbon composites synthesized by the sulfur melting route is limited to a relatively low value in order to obtain acceptable electrochemical performance, leading to a lower overall capacity of the cathodes.<sup>37, 40, 71, 150, 151</sup> Moreover, synthesizing homogeneous sulfur-carbon composites through conventional heat treatment is complicated. In the conventional synthesis of sulfur-carbon composites, sulfur is first heated above its melting temperature, and the

liquid sulfur is then diffused to the surface or into the pores of carbon substrates to form the sulfur-carbon composites.<sup>36, 37, 40, 60, 71, 77, 150, 151</sup> A subsequent high-temperature heating step is then required to remove the superfluous sulfur on the surface of the composites,<sup>37, 71, 77, 150</sup> leading to a waste of some sulfur. Thus, the conventional synthesis by the sulfur melting route may not be a practical scale-up approach to obtain a uniform industry-level sulfur-carbon composite although good performances have been realized with them.

A sulfur deposition method to synthesize a core-shell carbon/sulfur material for lithium-sulfur batteries has been reported by Wang *et al.*<sup>38</sup> Although it exhibited good cyclability and rate capability, their sulfur deposition process is very sensitive and need to be carefully controlled during synthesis; otherwise, a composite with poor electrochemical performance is produced. Therefore, the objective of our study is to develop an easily scalable chemical synthesis approach to synthesize sulfur-carbon composites with low manufacturing cost. Accordingly, we present here a facile sulfur deposition route to synthesize sulfur-carbon composites, which not only offers a low-cost approach for large-scale production but also produces high-purity active material.

## 3.2 EXPERIMENTAL

### 3.2.1 *In situ* sulfur deposition synthesis of sulfur-carbon composites

The synthesis process for the sulfur-carbon composite by the *in situ* sulfur deposition route is illustrated in Figure 3.1, and the *in situ* sulfur deposition in aqueous solution involves the following reaction:



First, 0.02 mole of sodium thiosulfate ( $\text{Na}_2\text{S}_2\text{O}_3$ , Fisher scientific) was completely dissolved in 750 mL of deionized (DI) water by stirring. Then, 0.1 g of commercial

conductive carbon black with a diameter of 30 – 60 nm (Super P) was suspended in the above solution by adding a small amount of isopropyl alcohol ( $C_3H_8O$ , Fisher scientific) under ultrasonic vibrations. The reason for adding isopropyl alcohol is that it enhances the wetting of the hydrophobic carbon nanoparticles in the aqueous solution. A 2 mL of hydrochloric acid (HCl, Fisher Scientific) was then slowly added to the solution to precipitate the sulfur onto the surface and into the interspaces of the nano-sized carbon black. During the *in situ* sulfur deposition reaction, the sulfur particles grow to a thermodynamically favored size and the carbon nanoparticles in the composite self-assemble, become interconnected with each other, and finally wrap the sulfur. After allowing the reaction mixture to stir for 24 h, the product was filtered and washed several times with DI water, ethanol, and acetone. The sulfur-carbon composite thus collected was dried in an air-oven at 50 °C for 24 h. The sulfur content in the composite was determined by thermogravimetric analysis (TGA) with a Perkin-Elmer TGA 7 Thermogravimetric Analyzer at a heating rate of 5 °C/min from 30 to 300 °C with flowing air. During this process, all the sulfur volatilizes and the sulfur content could be obtained from the observed weight loss because there is no loss related to the carbon black at this temperature range. The sulfur-carbon composites with 75 wt. % sulfur as confirmed by the TGA data were employed for further experiments.

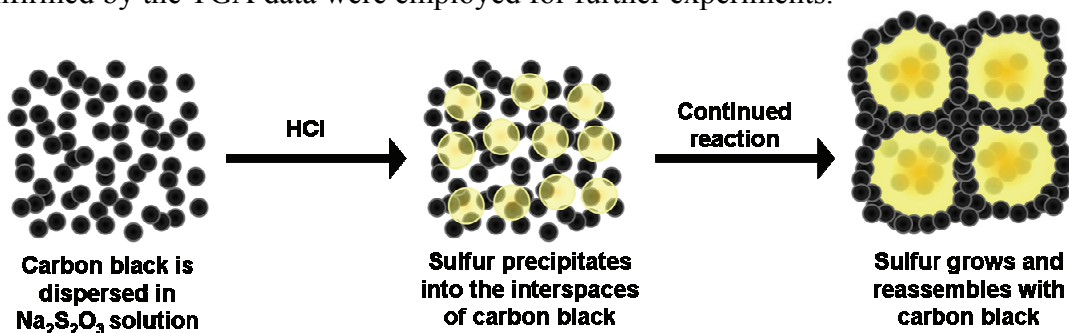


**Figure 3.1.** Scheme illustrating the *in situ* sulfur deposition route to obtain the sulfur-carbon composite.

Wang *et al.*<sup>65</sup> used a similar solution-based reaction to obtain sulfur, but the carbon was attached to the surface of the sulfur particles by an extra mixing process after the precipitation of sulfur. In other words, only part of the sulfur was slightly connected with the conductive carbon, resulting in a low utilization of the active material. In contrast, the *in situ* sulfur deposition route used in our study ensures that sulfur contacts with the carbon black closely due to the heterogeneous nucleation of sulfur. In order to have a comparison, pure sulfur was also synthesized by the same reaction route, but carbon black was added after sulfur was precipitated.

### **3.2.2 Structural and microstructure characterizations**

The synthesized samples were characterized with a Philips X-ray Diffractometer (PW 1830 + APD 3520) with Cu K $\alpha$  radiation between 10° and 70° at a scan rate of 0.04 °/s. The microstructure and morphology of the samples were examined with a JEOL JSM-5610 and a FEI Quanta 650 scanning electron microscope (SEM) and a JEOL JEM-2010F transmission electron microscope (TEM). The composition of the sulfur-carbon composite was also determined with an energy dispersive spectrometer (EDS) attached to the TEM instrument.

### **3.2.3 Cell assembly**

The sulfur-carbon composite thus obtained was individually mixed with 10 wt. % of Super P carbon and 10 wt. % of polyvinylidene fluoride (PVDF, Kureha) binder in an *N*-methylpyrrolidinone (NMP, Sigma-Aldrich) solution. The well-mixed slurry was tape-casted onto a sheet of aluminum foil and the film was dried in a convection oven at 50 °C for 24 h, followed by pressing with a roller and punching out circular electrodes of a 0.5 inch diameter. The cathode electrode disks were dried in a vacuum oven at 50 °C

for an hour before assembling the cell. Similar electrodes with the same overall amount of Super P carbon and binder were also fabricated with the as-synthesized pure sulfur under the same conditions. Next, 1.0 M LiCF<sub>3</sub>SO<sub>3</sub> (Acros Organics) salt was added to a mixture of 1,2-Dimethoxyethane (DME, Acros Organics) and 1,3-Dioxolane (DOL, Acros Organics) (1:1, v/v) and stirred for 5 min to prepare the electrolyte. The CR2032 coin cells were then assembled with the prepared cathode disks, prepared electrolyte, Celgard polypropylene separators, lithium foil anodes, and nickel foam current collectors. The cell assembly was conducted in a glove box filled with argon.

### **3.2.4 Electrochemical characterizations**

The cyclic voltammetry (CV) data were collected with a VoltaLab PGZ 402 Potentiostat at a scan rate of 0.05 mV/s between 3.5 and 1.0 V. The reference electrode is lithium (Li/Li<sup>+</sup>, -3.045 V vs. NHE). The charge-discharge profiles, cyclability, and rate capability were assessed with an Arbin battery cycler. All cells were rested for 30 minutes before electrochemical cycling. The cells were then discharged to 1.5 V and charged to 2.8 V for one full cycle. An additional charge condition of achieving a capacity of 1C ( $C = 1675 \text{ mAh g}^{-1}$ , the mass is based on the sulfur content in cathodes) was set for the pure sulfur cathode to avoid the infinite charging because the charge plateau would never reach 2.8 V due to the severe shuttle effect.<sup>31,32</sup> After cycling, coin cells were opened in the glove box to retrieve the cycled cathodes and examined by SEM to investigate their morphological changes. Electrochemical impedance spectroscopy (EIS) measurements were performed with a Solartron Impedance Analyzer (SI 1260 + SI 1287) in the frequency range of 1 MHz to 100 mHz with an AC voltage amplitude of 5 mV.

### 3.3 RESULTS AND DISCUSSION

#### 3.3.1 XRD, SEM, TEM and EDS studies

Figure 3.2 compares the X-ray diffraction (XRD) patterns of the pure sulfur, sulfur-carbon composite, and carbon black. The Super P carbon black, showing no sharp crystalline peaks, has amorphous structure. The pure sulfur and sulfur-carbon composite exhibit peaks perfectly matching with those of pure orthorhombic sulfur (JCPDS 00-008-0247). The sulfur-carbon composite shows much higher peak intensities than the pure sulfur as the dispersed nanoparticles of carbon black act as numerous deposition sites for elemental sulfur, leading to a favorable precipitation environment. This *in situ* sulfur deposition route thus provides an efficient means to produce high-purity sulfur composites.

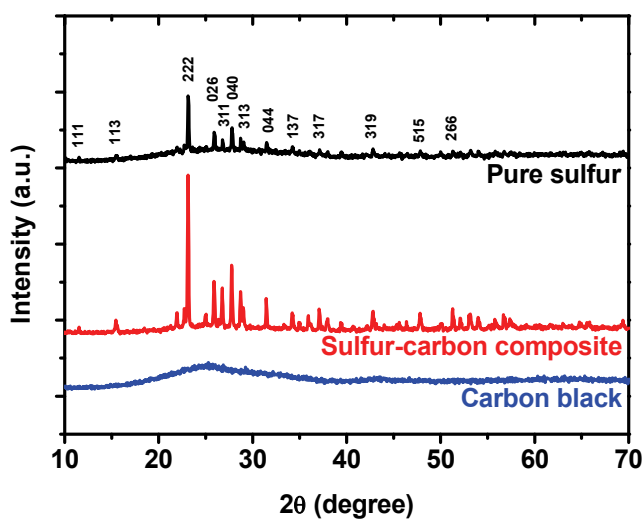


**Figure 3.2.** XRD patterns of the pure sulfur, sulfur-carbon composite, and carbon black.

The microstructure of the carbon black, pure sulfur, and sulfur-carbon composite are shown in Figure 3.3. The particle size of spherical carbon black is less than 100 nm. The pure sulfur contains glue-like particles with a diameter of few microns. Figure 3.3(c)

presents the structure of the sulfur-carbon composite in which sulfur particles are uniformly distributed throughout the network structure formed by carbon black. Carbon black partially embeds in the sulfur, and the remainder wraps around the matrix sulfur as a protective layer. This network structure confirms close contact between the conductive carbon and sulfur, providing not only excellent electron pathways for the insulating sulfur but also many adsorbent points to avoid the loss of the soluble polysulfides into the electrolyte. The TEM images in Figure 3.4(a) and 3.4(b) show that the carbon black nanoparticles in the sulfur-carbon composite are chain-like, which effectively enhances the conductivity of the composite material.<sup>37</sup> The elemental analysis of the sulfur-carbon composite carried out by EDS is shown in Figure 3.4(c), demonstrating the existence of both sulfur and carbon.

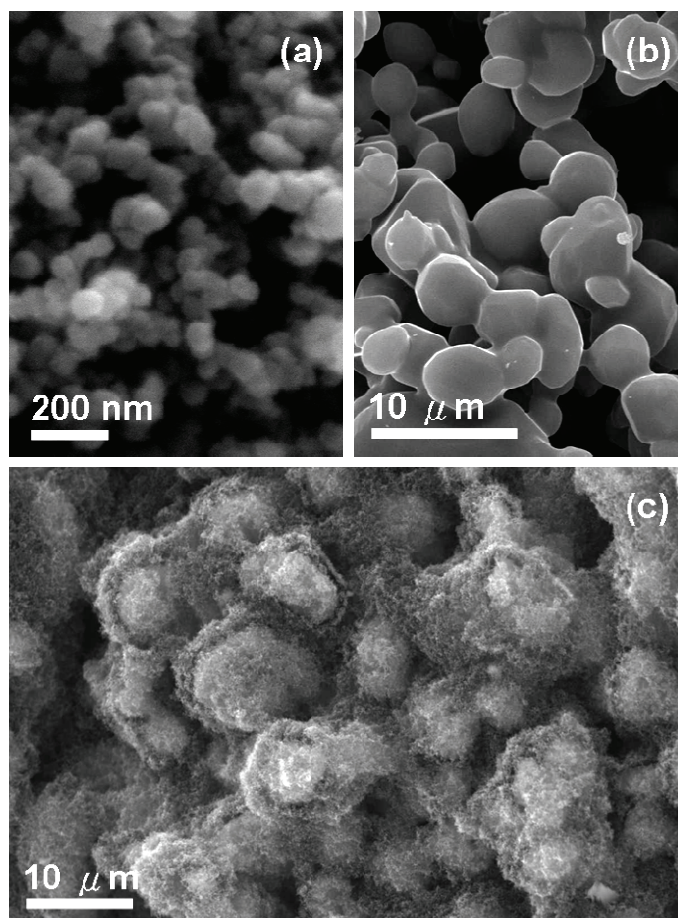


**Figure 3.3.** SEM images of the (a) carbon black, (b) pure sulfur, and (c) sulfur-carbon composite with carbon-wrapped sulfur network structure.

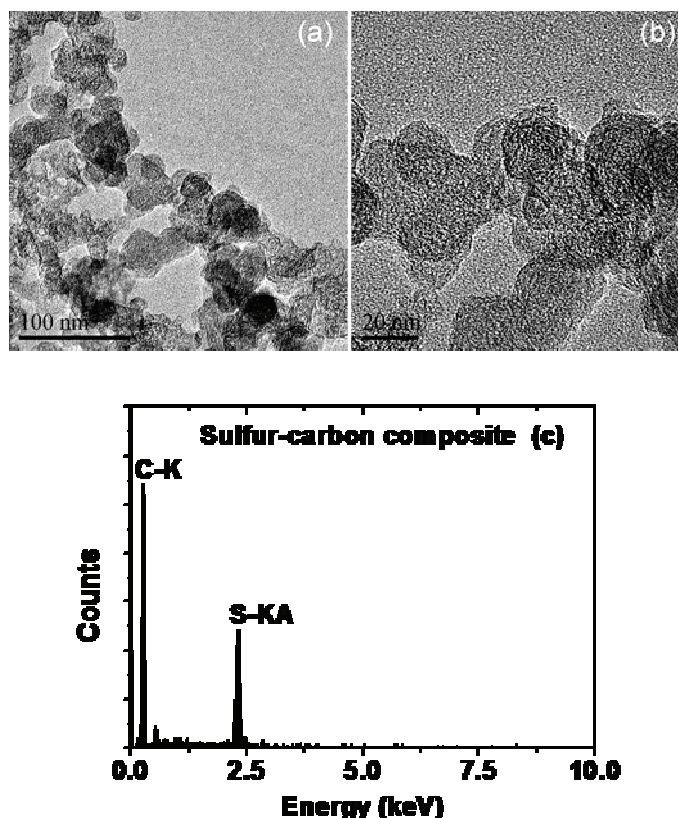


**Figure 3.4.** (a) Low and (b) high magnification TEM images of the sulfur-carbon composite and (c) EDS analysis of (b) showing the existence of both sulfur and carbon.

### 3.3.2 Electrochemical properties

To understand the reduction/oxidation reactions of the sulfur-containing cathodes in Li-S batteries, a CV test was conducted with the CR2032 coin cells. For the pure sulfur cathode, two sharp cathodic peaks located at 2.3 and 2.0 V are observed in the first discharge process in Figure 3.5(a), corresponding to the reduction of elemental sulfur to soluble polysulfides and then to the insoluble  $\text{Li}_2\text{S}$ , respectively. Several anodic peaks occur continuously with similar current density from 2.3 to 3.0 V as the potential scans to the charging voltage. These oxidation peaks occurring in a broad voltage range show the consumption of much more energy than that of regular cases, suggesting poor charging

efficiency and severe polarization due to the shuttle effect in Li-S batteries. In the subsequent cycles, both the reduction peaks shift to lower potential ranges compared to that in the first cycle, indicating a discharge overpotential after recharging. The current densities of both the reduction peaks also drop in the second and third cycles, indicating the irreversible capacity fade of the as-synthesized pure sulfur cathode. The CV profile of the sulfur-carbon composite cathode synthesized by the *in situ* sulfur deposition route is shown in Figure 3.5(b). The CV patterns in the first three cycles almost overlap each other in contrast to that found with the pure sulfur cathode in Figure 3.5(a), indicating the excellent cyclability of the sulfur-carbon composite cathode. A small anodic shift of the first reduction peak (Peak I) is observed in the second and third cycles compared to that in the first cycle. This may be due to the higher adsorbing energy between carbon black and sulfur in the first cycle compared to that in the subsequent cycles.<sup>71</sup> The oxidation reaction can be divided into two overlapping peaks (Peak III and IV), representing the formation of  $\text{Li}_2\text{S}_n$  ( $n > 2$ ) and the final oxidized active sulfur ( $\text{Li}_2\text{S}_8$  or  $\text{S}_8$ ), respectively.

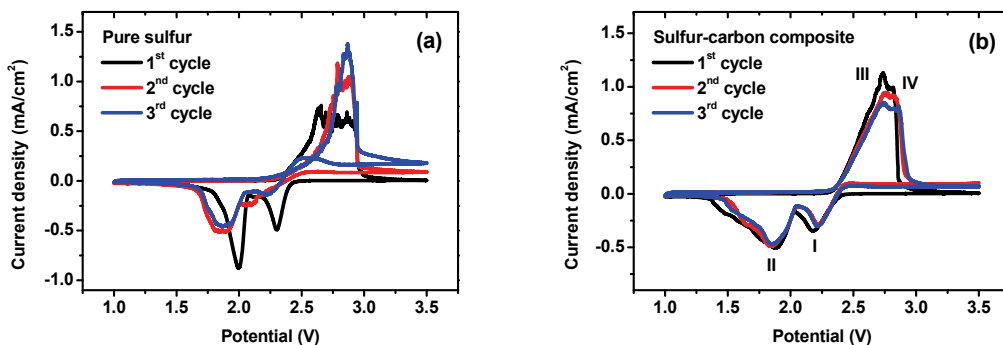


**Figure 3.5.** Cyclic voltammetry plots of the cathodes fabricated with the (a) pure sulfur and (b) sulfur-carbon composite at a scan rate of  $0.05 \text{ mV s}^{-1}$  under a voltage window of  $1.0 - 3.5 \text{ V}$  (vs.  $\text{Li}^+/\text{Li}$ ).

The first charge/discharge profiles of the pure sulfur and sulfur-carbon composite cathodes are shown in Figure 3.6(a). In the discharge profile, the two discharge plateaus

(Plateau I and II) are related to the two peaks (Peaks I and II) mentioned with the CV data. In the charge profile, the two plateaus (Plateau III and IV) of the sulfur-carbon composite cathode correspond to the two oxidation reactions exhibited in the CV plots as well. The terminal states of the charge process in the pure sulfur and sulfur-carbon composite cathodes are quite distinct. The charge process in the sulfur-carbon composite cathode ends with a sharp voltage raise when the cell voltage reaches 2.8 V. In contrast, the charge process in the pure sulfur cathode shows a typical shuttle behavior even after the charge capacity reaches over 1 C,<sup>26, 27, 32</sup> leading to poor charge efficiency and loss of active material. The sulfur in the pure sulfur cathode resembles glue-like particles, where sulfur connects one another and forms many inactive regions without contact with conductive carbon. These inactive portions are freely dissolved in the electrolyte without any confinement from the adsorption of carbon black during cycling. The adsorption of the polysulfides in the carbon-wrapped sulfur network structure of the sulfur-carbon composite appears to prevent the soluble polysulfides from migrating toward the anode region, thereby efficiently suppressing the shuttle effect at a low current density (C/20) during charging.

Figure 3.6(b) displays the discharge profiles at various cycle numbers of the pure sulfur and the sulfur-carbon composite cathodes. The upper discharge plateau of the pure sulfur cathode continuously shrinks as the cycle number increases, which is consistent with the diminished reduction peaks in Figure 3.5(a). This indicates the irreversible loss of active material in the pure sulfur cathode. After the 30<sup>th</sup> cycle, the discharge capacity is less than half of the initial capacity, showing poor cyclability. In contrast, the sulfur-carbon composite cathode has overlapping upper plateaus in the first three cycles, showing excellent electrochemical reversibility. The discharge capacity of the

sulfur-carbon composite cathode after the 30<sup>th</sup> cycle has a retention rate of 78%, which is much higher than that found with the pure sulfur cathode.

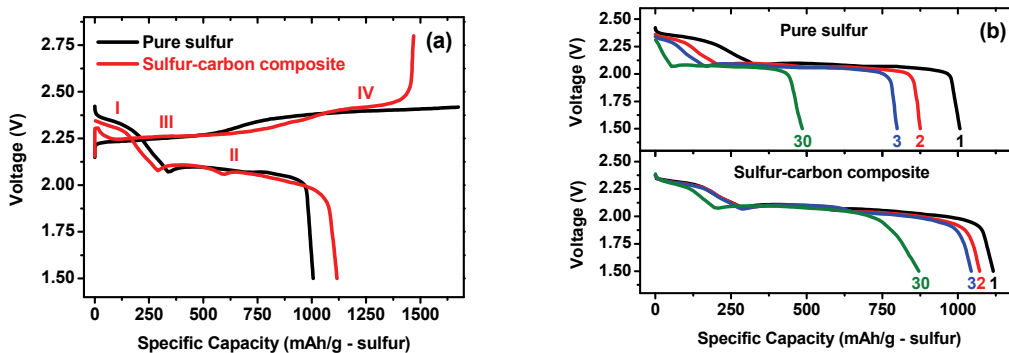


**Figure 3.6.** (a) First charge/discharge profile and (b) discharge curves at various cycles of the pure sulfur and sulfur-carbon composite cathodes cycled at 1.5 – 2.8 V (vs. Li<sup>+</sup>/Li) at a rate of C/20.

The cyclabilities of the pure sulfur and sulfur-carbon composite cathodes are compared in Figure 3.7(a). The sulfur-carbon composite cathode has a higher first discharge capacity of 1116 mAh g<sup>-1</sup> compared to 1006 mAh g<sup>-1</sup> for the pure sulfur cathode, implying that improved active material utilization can be achieved when sulfur is well-distributed in the carbon network structure due to the increased contact area between conductive carbon black and insulating sulfur. The reversible discharge capacity of the sulfur-carbon composite cathode after the 50<sup>th</sup> cycle is 777 mAh g<sup>-1</sup>. This reversible capacity value largely exceeds that of the pure sulfur cathode, indicating the superior cyclability of the sulfur-carbon composite cathode. The cycle life plots of the sulfur-carbon composite cathode at various rates are shown in Figure 3.7(b). As previously encountered, the first discharge capacity decreases with increasing current density or C rate. At a rate of C/4, the reversible discharge capacity after 50 cycles still remains at 697 mAh g<sup>-1</sup>, representing a 82% capacity retention. This excellent cycle

performance makes the sulfur-carbon composite cathode a promising candidate for high rate practical Li-S batteries.

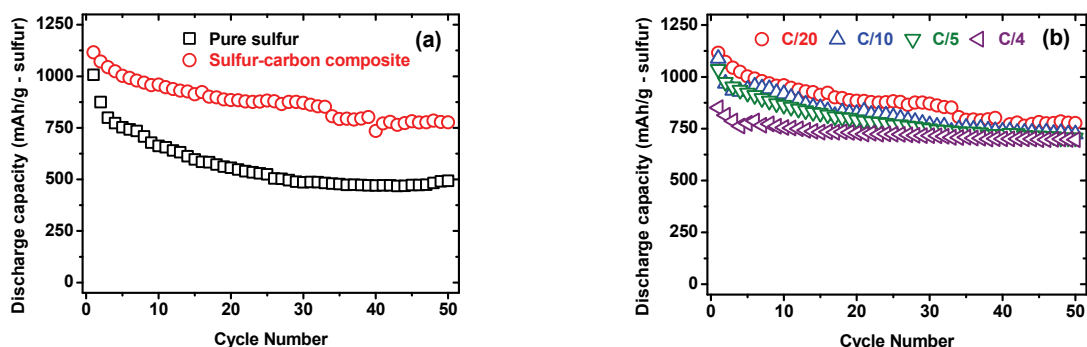


**Figure 3.7.** Comparison of the cyclability of the (a) pure sulfur and sulfur-carbon composite cathodes at a rate of C/20 and the (b) sulfur-carbon composite cathode at various C rates.

### 3.3.3 SEM and EIS analysis of cycled electrodes

To investigate the morphological change of the cathode after the charge/discharge process, the cycled cathodes were removed from coin cells after 25 cycles. Figure 3.8(a) and 3.8(b) illustrate the morphology of the pure sulfur and sulfur-carbon composite cathodes before cycling. The sulfur particles are fairly evenly distributed on the flat cathode surface. Figure 3.8(c) and 3.8(d) show the surface microstructure of the pure sulfur and sulfur-carbon composite cathodes after the 25<sup>th</sup> cycle. The sulfur-carbon composite cathode still maintains a relatively flat surface, implying the electrochemical process has limited impact on the cathode structure during cycling. This result indicates that the reduction/oxidation process of the active sulfur is effectively localized to the carbon-wrapped sulfur network structure. In contrast, a porous structure is formed in the case of the pure sulfur cathode after 25 cycles. The pore size resembles the particle size of the as-synthesized pure sulfur, indicating that the active sulfur continuously leaches out during the charge/discharge process and pores are gradually formed in the cathode

structure. These pores could develop into macroscopic cracks after many cycles due to the irreversible  $\text{Li}_2\text{S}$  plating on those areas, causing structural failure.<sup>31</sup> In other words, sulfur particles have been distributed throughout the cathode by a conventional mixing process with the carbon black in case of the pure sulfur cathode, and this structure cannot prevent the dissolution of polysulfides, resulting in poor electrochemical performance. In contrast, a conductive carbon-wrapped sulfur network structure produced by the *in situ* sulfur deposition route in the case of the sulfur-carbon composite not only maintains the structural integrity but also suppresses the migration of soluble polysulfides from the carbon matrix.

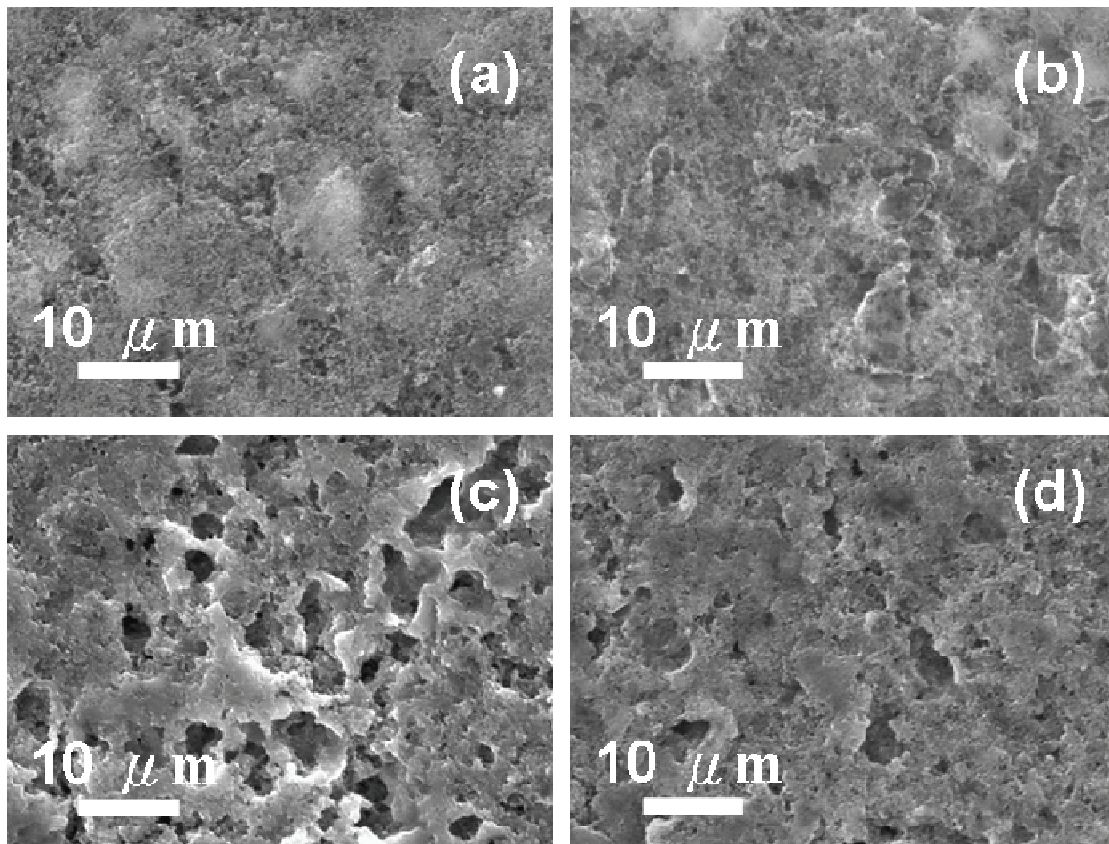


**Figure 3.8.** SEM images of the (a) pure sulfur and (b) sulfur-carbon composite cathodes before cycling and the (c) pure sulfur and (d) sulfur-carbon composite cathodes after cycling at  $C/5$  rate for 25 cycles.

To understand the reason for the superior electrochemical performance of the sulfur-carbon composite synthesized by the *in situ* sulfur-deposition route, EIS measurements were carried out with the coin cells. The Nyquist profiles of the pure sulfur and sulfur-carbon composite cathodes and the equivalent circuits are shown in Figure 3.9.  $R_e$  refers to the resistance of electrolyte,  $R_{ct}$  refers to the charge transfer resistance between the interfaces of carbon/sulfur/electrolyte,  $W_o$  refers to the Warburg impedance, and CPE refers to the constant phase element.<sup>152</sup> The resistance of electrolyte was estimated from the intersection of the front end of semicircles with the  $Z'$  axis, which is similar for both the cathodes. The diameter of the impedance semicircles is related to the charge transfer resistance, which is a measure of the difficulty involved for charges crossing the boundary between the electrode and electrolyte. Before cycling, the sulfur-carbon composite cathode has a slightly lower charge transfer resistance value than the pure sulfur cathode, which is expected considering its higher first discharge capacity compared to that of the pure sulfur cathode. The close contact between the conductive carbon black and the insulating sulfur lowers the resistance for electrons transferring across the interface between them. In the subsequent cycles (1<sup>st</sup>, 25<sup>th</sup>, and 50<sup>th</sup>), the charge-transfer resistance of the pure sulfur cathode grows much larger than that found with the sulfur-carbon composite cathode. The main reason for this is the porous structure of the cycled pure sulfur cathode. Electrons passing across the boundary between conductive carbon and active material are impeded by the irreversible formation of the  $Li_2S$  layer in the pores.<sup>31</sup> The EIS measurements thus reveal that the sulfur-carbon composite cathode exhibits better electronic conductivity and lithium-ion transport than the pure sulfur cathode due to the stable network structure of carbon black wrapping around the sulfur. The impedance of the sulfur-carbon composite after 50<sup>th</sup> cycles does

not increase much, suggesting that the network structure maintains its integrity during the cycling process.

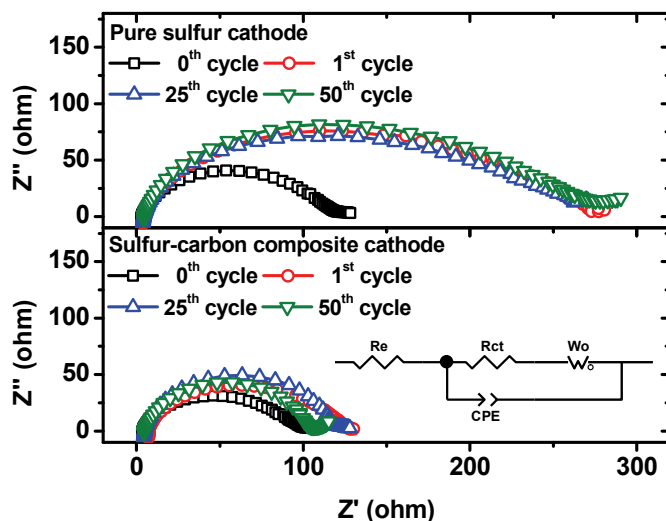


**Figure 3.9.** Electrochemical impedance spectra of the pure sulfur and sulfur-carbon composite cathodes before and after cycling at C/5 rate.

### 3.4 CONCLUSIONS

An *in situ* sulfur deposition route has been developed by the heterogeneous nucleation of sulfur onto conductive carbon black (Super P) from a solution-based reaction of sodium thiosulfate with hydrochloric acid. This facile synthesis method can produce high-purity sulfur-carbon composites for large-scale manufacturing. The sulfur-carbon composite thus produced exhibits discharge capacities of, respectively, 1116 mAh g<sup>-1</sup> in the first cycle and 777 mAh g<sup>-1</sup> after 50 cycles. Even after 50 cycles at a higher rate of C/4 (419 mA g<sup>-1</sup>), the reversible capacity is still 697 mAh g<sup>-1</sup>, which translates to a capacity retention of 82%. The excellent cycle performance of this sulfur-carbon composite can be attributed to the conductive carbon-wrapped sulfur network structure, which not only decreases the charge transfer resistance but also helps

maintaining the integrity of the electrode structure during cycling. The carbon black matrix also plays a protective role as an adsorbent agent to keep the soluble polysulfides within the electrode structure, avoiding the unwanted shuttle effect during charging. We believe this facile *in situ* sulfur deposition route to obtain sulfur-carbon composites possessing good electrochemical performance could enhance the feasibility of practical Li-S batteries.

## Chapter 4: Self-weaving sulfur-carbon composite cathodes for high rate lithium-sulfur batteries

### 4.1 INTRODUCTION

Increasing global energy demand and environmental concerns are becoming one of the greatest challenges facing humankind in the 21<sup>st</sup> century. Faced with the reality of limited fossil fuel resources and their environmental consequences, use of rechargeable batteries such as lithium-ion batteries for transportation applications is drawing much attention. However, the high cost, safety concerns, and limited energy density associated with the currently available insertion-compound electrodes (*e.g.*, layered LiCoO<sub>2</sub>, spinel LiMn<sub>2</sub>O<sub>4</sub>, and olivine LiFePO<sub>4</sub> cathodes and graphite anode) remain to be an impediment to adopt them.<sup>4, 5, 153</sup> Development of alternative low-cost, abundant electrode materials with high energy and power densities is critical for widely employing rechargeable batteries for transportation. Rechargeable lithium-sulfur batteries are attractive in this regard as sulfur is abundant and exhibits an order of magnitude higher theoretical capacity (1675 mAh g<sup>-1</sup>) with a two-electron electrochemical reaction compared to the currently used cathodes.<sup>20, 25, 36</sup> However, poor active material utilization, rate capability, and cyclability resulting from the high electrical resistivity of sulfur ( $5 \times 10^{-30}$  S·cm<sup>-1</sup>) and dissolution of intermediate discharge products (polysulfides Li<sub>2</sub>S<sub>x</sub> with  $2 < x \leq 8$ ) into the electrolyte during the charge-discharge process remain to be major obstacles to employ the Li-S batteries.<sup>7, 18, 26, 27, 32</sup>

Various sulfur-carbon composites have been designed in recent years to overcome these difficulties,<sup>36, 40, 51, 55-57, 60, 62, 65, 72, 77, 81, 82</sup> and conductive carbon materials, especially carbon with porous structure, could not only improve the electrical conductivity but also trap part of the soluble polysulfides during cycling.<sup>36, 40, 51, 60, 62, 72, 81</sup>

However, most of the previously reported composites have only shown improvements in low rate capability ( $< C/2$ ) and cyclability. He *et al.*<sup>72</sup> developed a bimodal porous carbon imbided with sulfur for high rate Li-S batteries, but the specific capacity was somewhat sacrificed due to a trade-off between capacity and high C rates. Jayaprakash *et al.*<sup>51</sup> reported porous hollow carbon-sulfur composites showing high rate capability up to 3C, but without continuous cycling tests at high rates.

Here we report a self-weaving sulfur/multi-wall carbon nanotube (MWCNT) composite cathode with unique structural/morphological and outstanding performance advantages over other sulfur composites for high rate rechargeable lithium-sulfur batteries. Carbon nanotubes have been used as a component in electrodes to enhance the rate capability of lithium-ion batteries.<sup>154-156</sup> The incorporation of carbon nanotubes provides abundant electron pathways, nano-scale reaction sites, and excellent mechanical strength to accommodate the volume changes of active material.<sup>55-57, 77, 82</sup> Moreover, carbon nanotubes exhibit a self-weaving behavior when being fabricated as a flexible film,<sup>79, 80, 157</sup> which enables binder/current collector-free electrode processing and eliminates the hazardous n-methyl-2-pyrrolidone (NMP) used in the conventional slurry casting method. Several sulfur-carbon nanotube composite cathodes synthesized by conventional methods (*e.g.*, sulfur melting route) have shown improved electrochemical performance, but they derive benefits only from the high electrical conductivity of carbon nanotubes. Our strategy utilizes the advantageous characteristics of MWCNTs to synthesize sulfur-MWCNT composite cathodes by a scalable *in situ* sulfur deposition method,<sup>29</sup> which is distinctly different from a recent study of binder-free sulfur cathodes by Aurbach's group.<sup>81</sup> They used a sulfur-impregnated carbon fiber cloth as the cathode material, but the binder-free characteristic was inherited from the purchased carbon substrate, which was not discussed in detail. Our composite cathodes are prepared

without other carbon additives, binders, or current collectors and fabricated into large, robust, flexible film electrodes. The rate capability and cyclability of the composite electrodes thus produced are significantly improved, which enhance the commercialization potential of Li-S batteries.

## **4.2 EXPERIMENTAL**

### **4.2.1 Synthesis**

Raw MWCNTs with a diameter of 10 – 20 nm prepared by a chemical vapor deposition (CVD) process were used in this study. To synthesize the self-weaving sulfur-MWCNT composite cathode, two batches of 75 mg of MWCNTs were separately dispersed in two 0.5 L of 0.03 M  $\text{Na}_2\text{S}_2\text{O}_3$  (Fisher Scientific) solutions by high-power ultrasonication for 15 minutes with the addition of 20 mL of isopropyl alcohol to each to mitigate the hydrophobic behavior of the MWCNTs and 0.75 mL of Triton X-100 (10% solution, VWR) to each as a dispersant. Additionally, Triton X-100 can minimize the dissolution of polysulfides due to the coating protection from its polyethylene glycol (PEG) chains.<sup>65</sup> 1.65 and 1.8 mL of HCl (Fisher Scientific) were then dropped into the two dispersions independently and stirred strongly for 18 h at room temperature to synthesize the sulfur-MWCNT composites. The products were vacuum-filtered and washed three times each with deionized water, ethanol, and acetone. The two self-weaving sulfur-MWCNT composite cathodes thus formed were flexible films with a diameter of 2.5 inches and a thickness of 40 – 50  $\mu\text{m}$  after drying for 24 h at 50 °C in an air-oven, which could be peeled off the filter membrane for subsequent experiments.

### **4.2.2 Materials characterizations**

The amount of sulfur in the composites was determined by thermogravimetric analysis (TGA) with a Perkin-Elmer TGA 7 Thermogravimetric Analyzer from 30 to 300

°C in flowing air at a heating rate of 10 °C/min. X-ray diffraction (XRD) patterns were recorded with a Philips X-ray Diffractometer (PW 1830 + APD 3520) with Cu K $\alpha$  radiation from 20° to 60° at a scan rate of 0.05°/s. The microstructures of the samples were examined with a Hitachi S-5500 scanning electron microscope (SEM) and a FEI Quanta 650 SEM. The elemental mapping results were performed with an energy dispersive spectrometer (EDS) attached to the FEI Quanta 650 SEM.

#### **4.2.3 Electrochemical measurements**

The self-weaving sulfur-MWCNT composite samples were cut as circular cathode disks of a 0.25 inch diameter without additional current collectors. A 1.85 M LiCF<sub>3</sub>SO<sub>3</sub> (Aldrich) solution was prepared with a mixture of 1,2-Dimethoxyethane (DME, Acros) and 1,3-Dioxolane (DOL, Acros) (1:1, v/v) as the electrolyte for cyclic voltammetry (CV) measurements. A 0.1 M LiNO<sub>3</sub> (Acros) salt was also added into the electrolyte to improve the Coulombic efficiency during cycling.<sup>62</sup> CR2032 coin cells were assembled with the self-weaving sulfur-MWCNT composite cathodes, the prepared electrolyte, Celgard polypropylene separators, lithium metal anodes, and nickel foam spacers in a glove box filled with argon. A pure sulfur cathode with a large amount of conductive carbon black (Super P carbon : sulfur = 3 : 2 by wt.) was fabricated with polyvinylidene fluoride (PVDF, Kureha) binder and an aluminum current collector and then assembled into coin cells as control experiments. The discharge/charge profiles and cycle data were obtained with an Arbin battery cycler. The C rates specified in this study are based on the mass and theoretical capacity of sulfur (1675 mA g<sup>-1</sup>). The CV data were collected with a VoltaLab PGZ 402 Potentiostat at a scan rate of 0.3 mV/s in the potential range of 2.8 – 1.5 V. The electrolyte absorption ability of the cathode material was estimated by soaking

the cathode film in the electrolyte solvent (DOL/DME, v/v = 1), removing it, and measuring the decrease in the volume of the electrolyte.

## **4.3 RESULTS AND DISCUSSION**

### **4.3.1 Fabrication, structure, and microstructure**

The fabrication process of the sulfur-MWCNT composite electrodes is shown in Figure 4.1. The first step is ultrasonically separating the intertwining MWCNT bundles in a dilute aqueous solution of sodium thiosulfate to separate the MWCNTs individually from the twisted cluster, followed by depositing sulfur onto them with the addition of hydrochloric acid. The sulfur tends to deposit onto the MWCNTs rather than nucleating by itself due to the low activation energy involved with heterogeneous nucleation. After allowing the deposition reaction to proceed overnight, the sulfur-MWCNT composite thus obtained was vacuum-filtered and washed. During the filtration process, a uniform and flexible sulfur-MWCNT composite film was formed because of its self-weaving behavior and it could be easily peeled off from the filter membrane after drying. This fabrication process of the sulfur-MWCNT cathode is tunable, scalable, and carried out in a water-based solution at room temperature without involving extra heat treatment or the use of toxic NMP; therefore, it is a green chemical synthesis/fabrication approach. In addition to being a low-cost and environmentally benign fabrication process, the elimination of cathode current collectors reduces the net weight of the electrodes and increases the energy density of the battery.

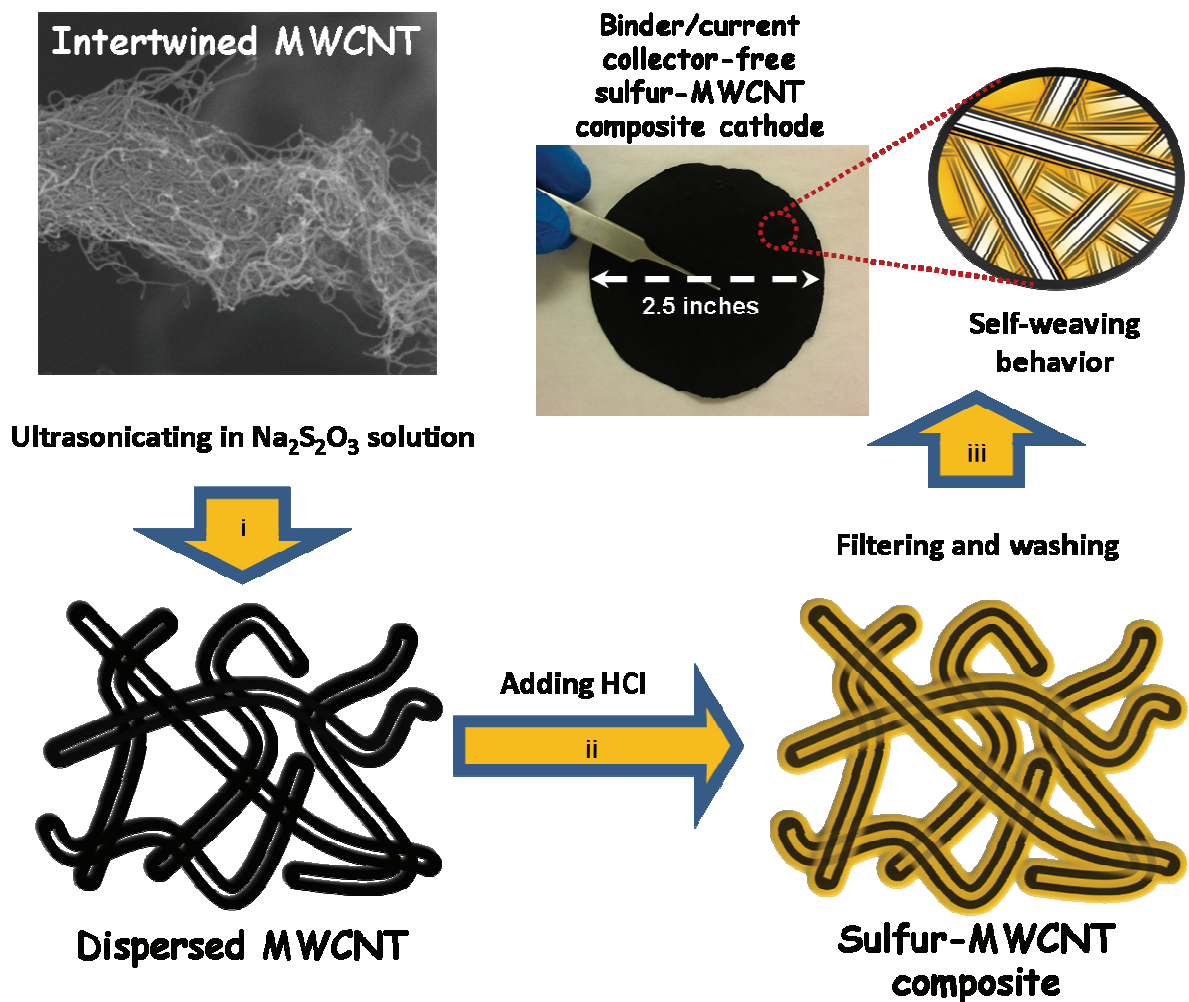


**Figure 4.1.** Schematic fabrication process of a self-weaving sulfur-MWCNT composite cathode synthesized by an *in situ* sulfur deposition method. Three simple steps to synthesize binder/current collector-free sulfur-MWCNT composite cathodes: (i) dispersion of MWCNTs, (ii) sulfur nucleation (yellow) onto MWCNTs, and (iii) vacuum filtration, washing, and then drying.

The self-weaving sulfur-MWCNT composite cathodes with 60 and 37 wt. % MWCNTs (denoted hereafter as S-CNT-A and S-CNT-B, respectively) were further investigated in this work. The sulfur content in the composites was determined by TGA (Figure 4.2). The observed weight loss in the TGA is only due to the evaporation of

sulfur since no obvious weight loss was found with the pristine MWCNTs at the same temperature range. The X-ray diffraction XRD pattern of the pristine MWCNTs indicates an amorphous structure without any sharp peaks (Figure 4.3), while those of the composite cathodes show crystalline peaks corresponding to elemental orthorhombic  $\alpha$ -sulfur  $S_8$  (JCPDS 00-008-0247), indicating the high purity and well-crystallized nature of the deposited sulfur during the heterogeneous nucleation process.

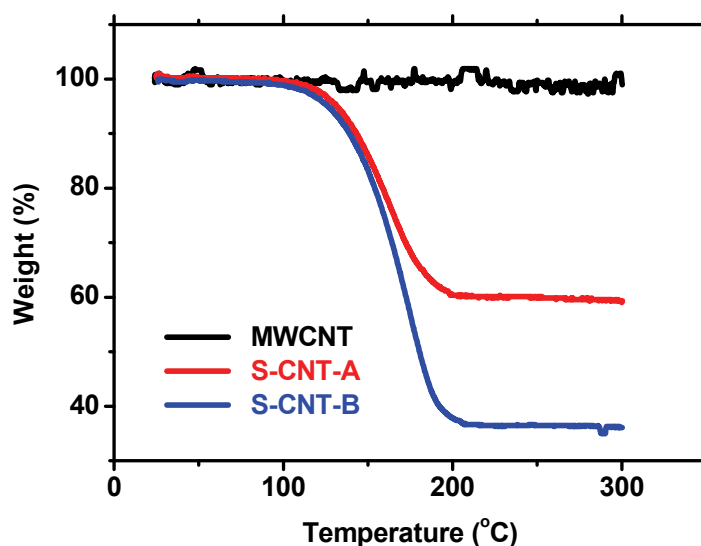


**Figure 4.2.** Thermogravimetric analysis of pristine MWCNTs and the self-weaving sulfur-MWCNT composites in flowing air with a heating rate of 10 °C/min, showing 40 wt. % sulfur in the S-CNT-A cathode and 63 wt. % sulfur in the S-CNT-B cathode.

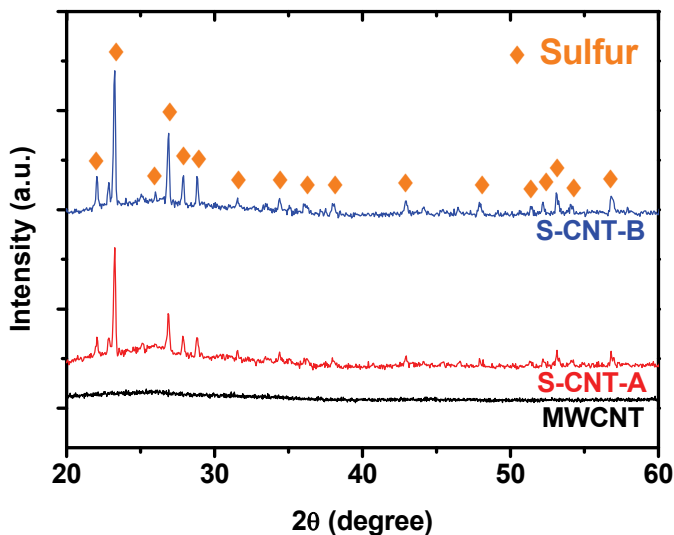


**Figure 4.3.** XRD patterns of pristine MWCNTs and the self-weaving sulfur-MWCNT composite cathodes. While the pristine MWCNTs show an amorphous structure, the sulfur in the composite cathodes is well-crystalline.

The morphology of the sulfur-MWCNT composites was examined by SEMs. The MWCNTs have a tortuous shape as seen in Figure 4.4(a), which is beneficial for the self-weaving process and fabricating a binder-free film. The SEM image of the surface of the S-CNT-A composite electrode is shown in Figure 4.4(b), in which sulfur could not be easily observed as large particles; however, sulfur is covering the entire MWCNT framework as indicated by the EDS mapping analysis in Figure 4.4(c), *i.e.*, the carbon nanotubes are embed in sulfur, forming an inseparable complex. The conductive MWCNTs act as a structural skeleton and support the integrity of the electrode. Moreover, the interwoven structure of the composites could absorb  $26 \mu\text{L}/\text{cm}^2$  of electrolyte, preserving the electrolyte and active materials within the MWCNT matrix.

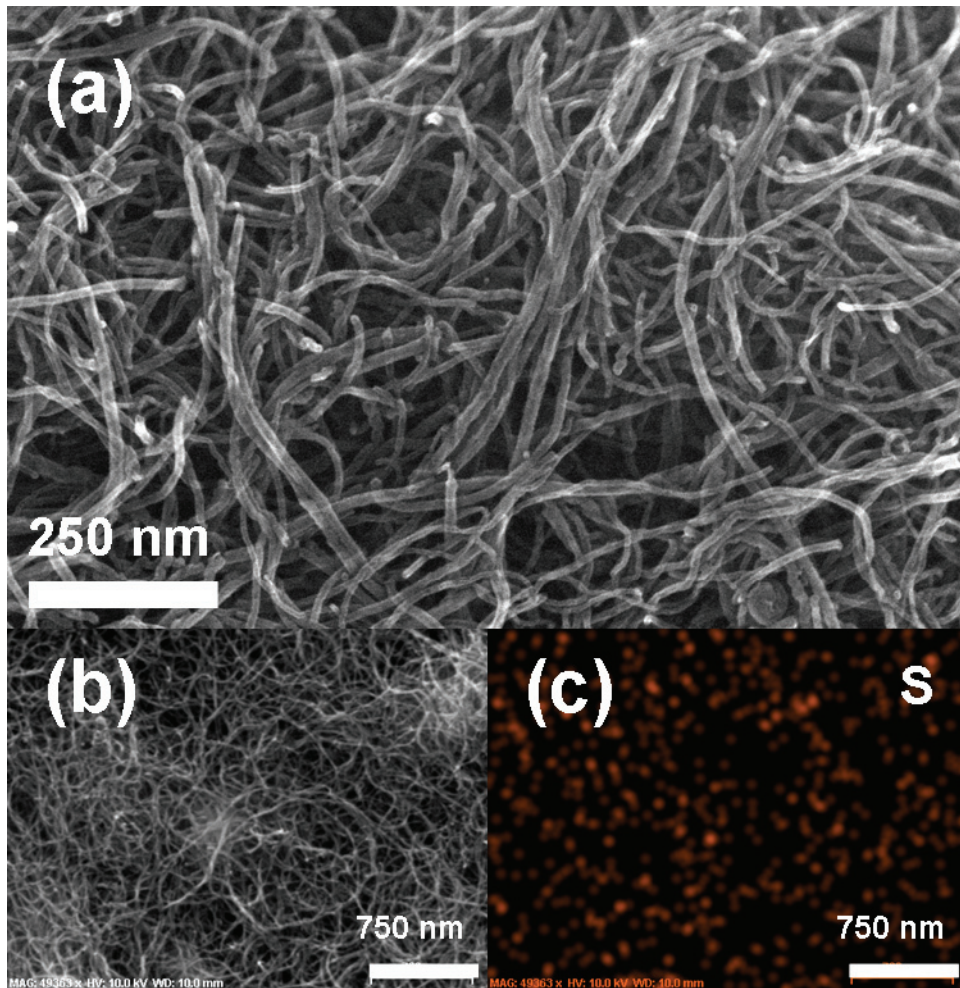
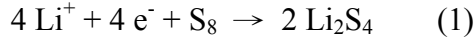


**Figure 4.4.** SEM images and EDS mapping of the self-weaving sulfur-MWCNT composite (S-CNT-A) cathode: (a) High-resolution SEM image of MWCNTs in the S-CNT-A cathode, exhibiting the self-weaving behavior of winding MWCNTs, (b) surface morphology of the S-CNT-A cathode sample, and (c) elemental sulfur distribution in (b).

### 4.3.2 Electrochemical performance

There are two typical plateaus in both the discharge (Plateau I and II) and charge (Plateau III and IV) profiles of the sulfur-MWCNT composite cathode (Figure 4.5(a)). The first discharge Plateau I from 2.3 to 2.0 V is attributed to the reduction of elemental sulfur to the soluble lithium polysulfides as shown in reaction 1 below:



This is a half-electron charge transfer per sulfur atom, contributing about 25% of the total specific capacity. The second discharge Plateau II at about 2 V is due to the further reduction of lithium polysulfides to  $\text{Li}_2\text{S}$  as shown in reaction 2 below:



This accounts for a one and a half electron charge transfer per sulfur, contributing the remaining 75% of the specific capacity. The first charge Plateau III between 2.3 and 2.35 V represents the oxidation reaction from the solid  $\text{Li}_2\text{S}$  to  $\text{Li}_2\text{S}_n$  ( $n > 2$ ), and the second charge Plateau IV represents the final oxidation of the polysulfides. The two cathodic (I, II) and anodic (III, IV) peaks in the cyclic voltammogram (CV) shown in Figure 4.5(b) resemble the two discharge (I, II) and charge (III, IV) plateaus. The first cathodic Peak I in the second cycle is located at a slightly higher voltage than that found after the first cycle, indicating a decrease in polarization. After the first discharge/charge process, the active materials rearrange to a favorable configuration with the lowest resistance in the MWCNT network, thus reducing the overpotential in the subsequent cycles. The CV profiles for the first 3 cycles have no significant change in voltage or current, showing the excellent electrochemical stability of the composite cathodes.

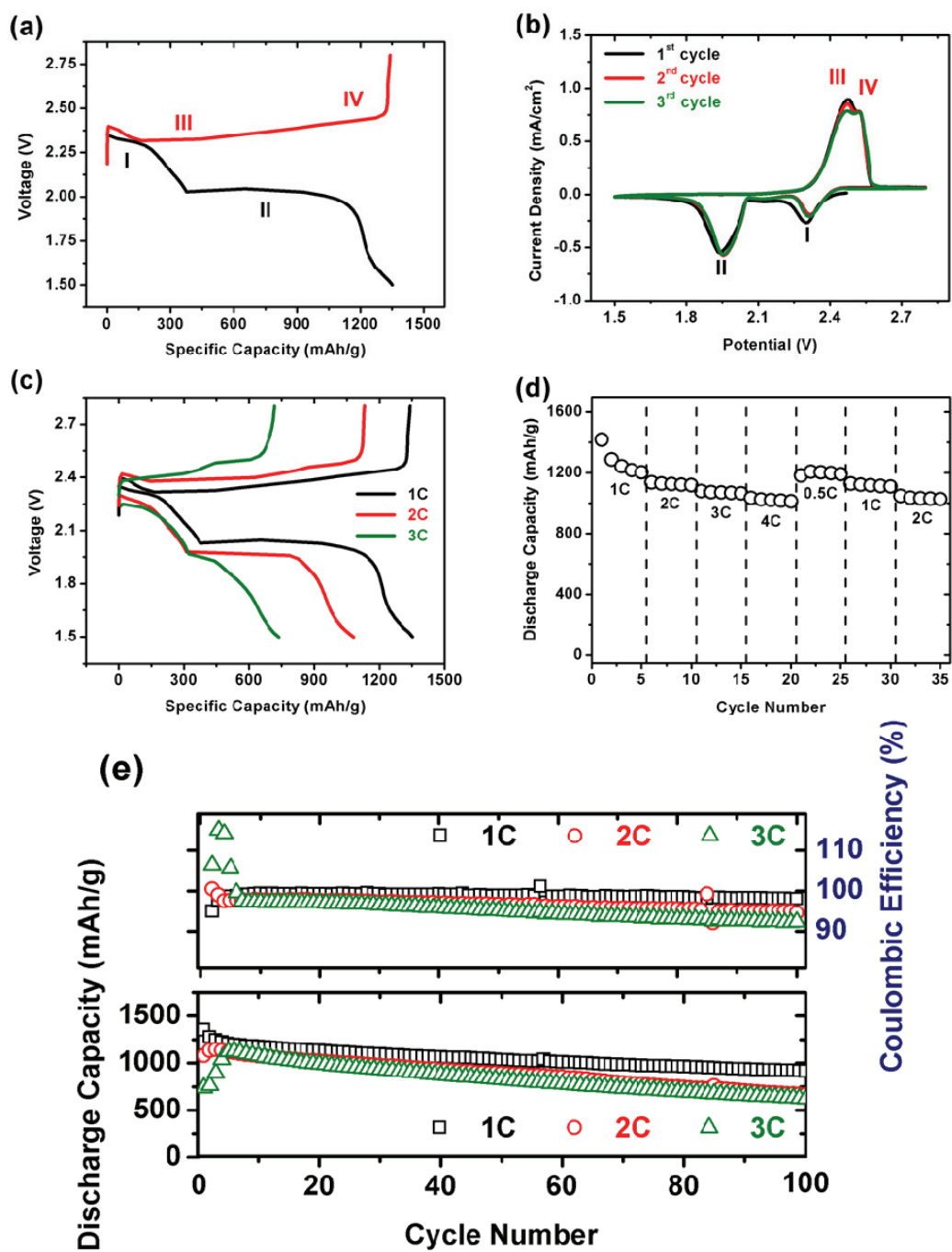


**Figure 4.5.** Electrochemical measurements of the self-weaving sulfur-MWCNT composite cathodes: (a) Discharge/charge profiles of S-CNT-A at 1C rate, (b) CV plots of S-CNT-A at a scan rate of 0.3 mV/s between 2.8 and 1.5 V during the first 3 cycles, (c) first discharge/charge profiles of S-CNT-A at 1C, 2C, and 3C rates, (d) rate capability

of the S-CNT-A cathode at various C rates, and (e) high-rate cycle performance (bottom half) and Coulombic efficiency (upper half) of the S-CNT-A cathode at 1C, 2C, and 3C rates for 100 cycles. The C rate is calculated based on the mass and theoretical specific capacity of sulfur ( $C = 1675 \text{ mA g}^{-1}$ ).

The first discharge/charge plateaus of the S-CNT-A sample at various rates are shown in Figure 4.5(c). The upper plateau shrinks only slightly with increasing discharge current density, representing the rate-independent reduction reaction of  $\text{S}_8/\text{Li}_2\text{S}_4$ . The major difference among the cathodes discharged at different rates is that the lower plateau is shortened and the polarization increases with increasing C rate. Due to the slow kinetics of reaction 2 occurring at the lower plateau,<sup>36</sup> the conversion of soluble polysulfides into solid  $\text{Li}_2\text{S}$  is largely influenced by the reaction rate. Therefore, incomplete conversion of lithium sulfide is observed at high C rates, resulting in lower active material utilization in Li-S cells at high rates. The rate capability profile of the S-CNT-A cathode is shown in Figure 4.5(d). The Li-S battery with the composite electrode could be charged/discharged at rates as high as 4C ( $6.7 \text{ Ah g}^{-1}$ ), while still maintaining a high specific capacity of at least  $1012 \text{ mAh g}^{-1}$  without obvious capacity fading. The discharge capacity of the cell is able to recover and reach a capacity of over  $1200 \text{ mAh g}^{-1}$  after the C rate returns from 4C to 0.5C, showing excellent cyclability under various conditions.

The cyclability profiles of the S-CNT-A electrode are shown in Figure 4.5(e). The S-CNT-A cathode exhibits a first discharge capacity of  $1352 \text{ mAh g}^{-1}$  at 1C rate ( $C = 1675 \text{ mA g}^{-1}$ ). After 100 cycles, the S-CNT-A cathode maintains a reversible capacity of  $915 \text{ mAh g}^{-1}$ . Even at a higher rate of 2C, the S-CNT-A cathode shows an excellent initial capacity of  $1080 \text{ mAh g}^{-1}$ . The average energy density of the S-CNT-A sample cycled for 100 cycles calculated based on the total mass of cathode is  $852 \text{ Wh kg}^{-1}$  at 1C rate,  $716 \text{ Wh kg}^{-1}$  at 2C rate, and  $648 \text{ Wh kg}^{-1}$  at 3C rate. As the C rate increases, the first

discharge capacity decreases due to the decreased utilization of active material at higher reaction rates.<sup>158</sup> At the higher rates of 2C and 3C, the specific capacity of the S-CNT-A cathode increases during the initial stages (first 5 cycles) in contrast to that found at 1C rate. This trend could be ascribed to the incomplete utilization of the active materials at high rates. The active materials in the composite self-rearrange during initial cycling, and thereby the inactive cores of sulfur become exposed to the electrolyte and are able to be reutilized in the subsequent cycles. In addition, the average Coulombic efficiencies of the S-CNT-A cathode at the various rates investigated are higher than 96%, indicating excellent electric/electrochemical efficiency in the Li-S cell. During the first five cycles, the S-CNT-A cathode cycled at 3C shows Coulombic efficiency even higher than 100%, which is due to the increasing utilization of the cores of the active materials during the initial cycles. Although the 3C rate translates to a full discharge or charge in 20 minutes, the real discharge/charge times are always shorter than the calculated ones because 100% active material utilization is never realized in Li-S batteries. The actual average charge time for S-CNT-A is only 11.6 minutes at 3C rate, demonstrating an impressive potential for ultra-fast charging.

To investigate if the excellent high-rate performance is favored by the large amount of carbon in the cathode, a pure sulfur cathode with the same carbon : sulfur ratio of 3 : 2 by wt. was investigated as a control experiment. Although the high-rate cyclability profiles of the pure sulfur cathode display acceptable initial discharge capacities (Figure 4.6), a sudden drop with 23 – 26% capacity loss occurs after the first cycle. This indicates that high carbon loading does not guarantee the good electrochemical performance of sulfur cathodes because the large amount of active material dissolution and loss cannot be avoided. Figure 4.7 shows the cyclability of the S-CNT-B cathode with higher sulfur loading at various rates up to 2C. The S-CNT-B

cathode obtains a first discharge capacity of as high as  $942 \text{ mAh g}^{-1}$  at 1C rate, and has a capacity retention rate of about 79% after 50 cycles. The specific capacity is lower than that of the S-CNT-A cathode due to incomplete active material utilization resulting from less conductive MWCNT addition. However, the cycle stability is still excellent without the capacity drop found with the pure sulfur cathode, demonstrating that the good capacity retention found is mainly due to the special network structure of the self-weaving sulfur-MWCNT composite cathodes.

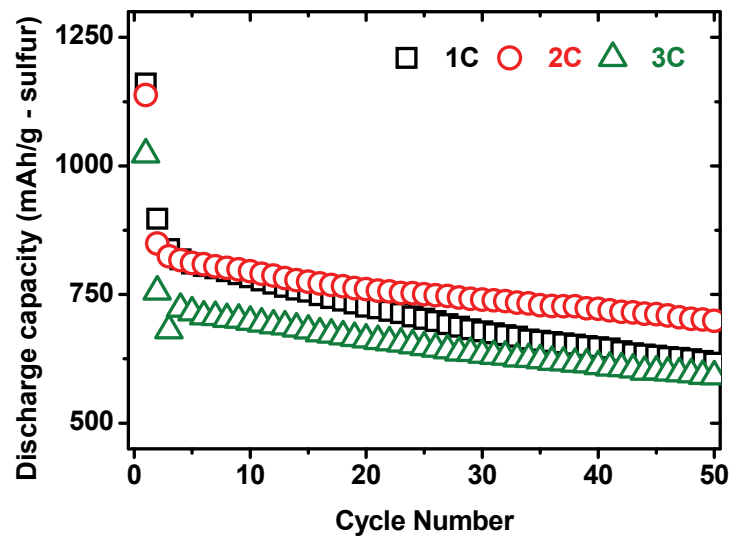


**Figure 4.6.** High-rate cycle performance of pure sulfur cathodes (carbon : sulfur = 3 : 2 by wt.) at 1C, 2C, and 3C rates. A severe capacity drop occurs after the first cycle.

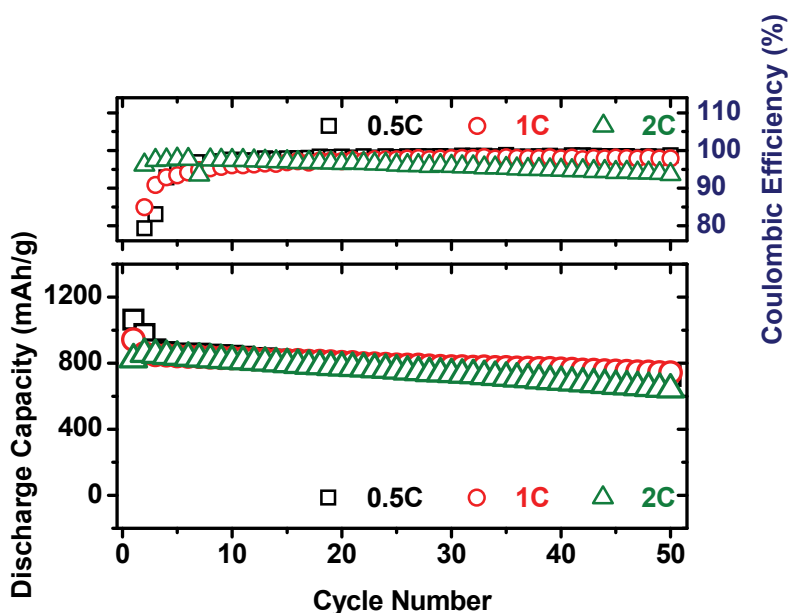


**Figure 4.7.** High-rate cycle performance (bottom half) and Coulombic efficiency (upper half) of the S-CNT-B cathode at 0.5C, 1C, and 2C rates.

### 4.3.3 Microstructure after cycling

The microstructure images and elemental mapping analysis of the self-weaving sulfur-MWCNT composite cathodes after cycling are shown in Figure 4.8. After 50 cycles, the composite cathode cycled at 2C still resembles the MWCNT network grid containing the active materials within the electrode. The active materials are captured into the nano-sized interspaces of the MWCNT skeleton as observed in Figure 4.8(a). With excellent mechanical strength, the flexible MWCNT framework is able to endure the volume expansion of the active materials during cycling.<sup>35</sup> Compared to the composite cathode before cycling (Figure 4.4(b)), the cathode surface becomes dense after cycling (Figure 4.8(b)), indicating the self-rearrangement behavior of the active materials during charging/discharging. If the active material covers onto some disjunctive conductors like carbon black particles, the cathode resistance will largely raise.<sup>33</sup> In

contrast, the MWCNTs in the composite here are interlaced with a length of over a few microns, so the conductivity of the electrode is not seriously affected, facilitating fast charge transfer during the electrochemical reaction. A portion of MWCNT network can be observed without the trapping active material, which is due to the lower sulfur content of the S-CNT-A cathode. The elemental mapping shown in Figure 4.8(c) indicates that sulfur is still uniformly distributed throughout the cathode structure after 50 reversible reduction/oxidation reactions, ensuring the cycling stability in lithium-sulfur batteries.<sup>55,</sup>  
<sup>60</sup> The unique structure of the MWCNT network offers three advantages: (i) enormous conductive paths and nanoscale electrochemical reaction sites, facilitating high specific capacities at high rates, (ii) a strong skeleton to accommodate the structural integrity of cathodes during cycling, and (iii) good absorption of the electrolyte and dissolved polysulfides, leading to good cycle stability. As a result, the self-weaving sulfur-MWCNT composite cathodes maintain a well-distributed morphology and retain sufficient reaction sites for electrochemical reactions, leading to excellent high-rate cycle performance.

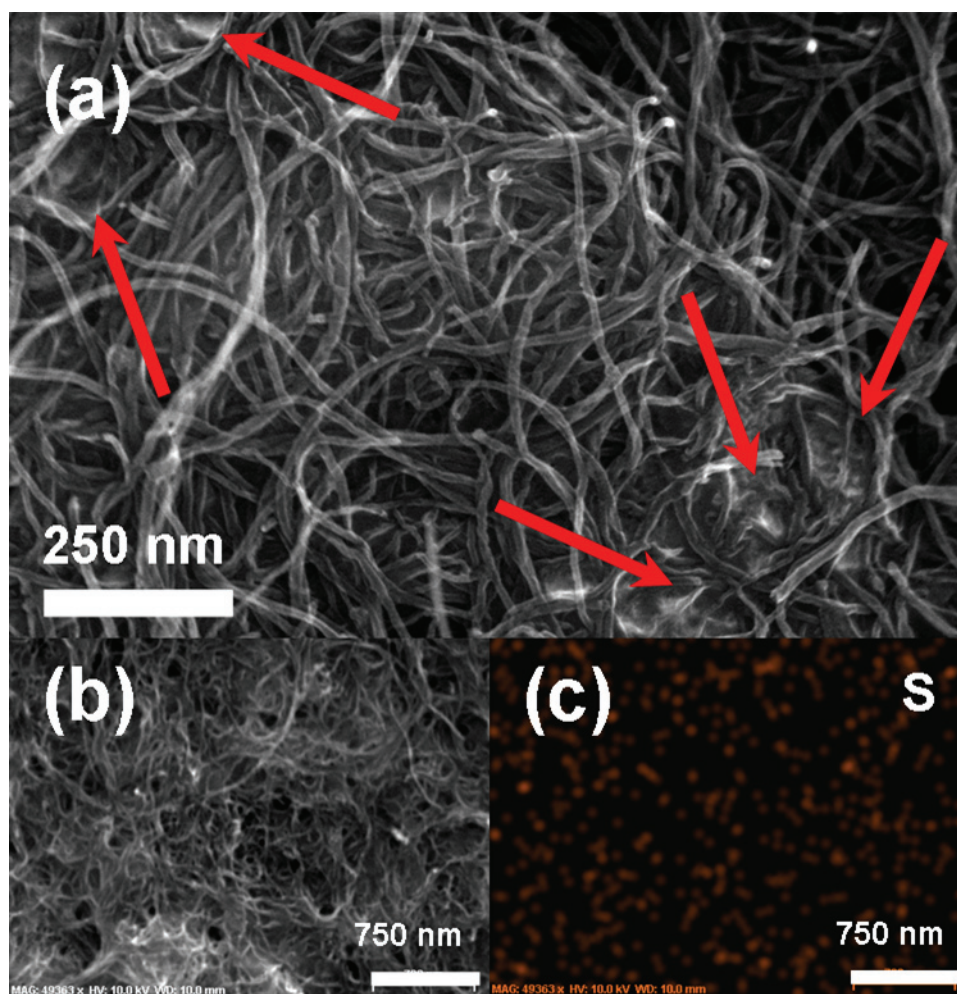


**Figure 4.8.** SEM images and EDS mapping of the S-CNT-A cathode after the 50<sup>th</sup> cycle at 2C rate: (a) High-resolution SEM image of the S-CNT-A cathode, where the active materials are captured into the interspaces of the MWCNT network (red arrows), (b) surface morphology of the cycled S-CNT-A cathode with a dense structure, and (c) elemental sulfur distribution in (b), revealing a homogeneous distribution of sulfur in the cathode and the structural stability after cycling.

#### 4.4 CONCLUSIONS

In summary, we developed a robust, flexible self-weaving sulfur-MWCNT composite cathode for rechargeable Li-S batteries via a scalable *in situ* sulfur deposition synthesis and a vacuum filtration process. The binder/current collector-free electrode is

formed due to the self-weaving nature of the MWCNTs, and the elimination of binders and cathode current collectors lowers the cost and toxicity associated with electrode manufacturing. The MWCNTs help retaining the integrity of the electrode structure during extended cycling and provide numerous electrical and ionic pathways during the electrochemical reaction, facilitating fast charge-discharge. Moreover, the soluble polysulfide intermediates formed are confined within the electrode structure during cycling because of the good electrolyte-absorption ability of the sulfur-MWCNT composite cathodes, avoiding the irreversible loss of the active materials. These excellent characteristics of the binder/current collector-free sulfur-MWCNT composite cathodes lead to high specific capacity with extraordinarily high-rate cyclability. The self-weaving sulfur-MWCNT composite approach is a promising strategy to make the rechargeable lithium-sulfur batteries a commercial reality.

## **Chapter 5: A new approach to improve cycle performance of rechargeable lithium-sulfur batteries by inserting a free-standing MWCNT interlayer**

### **5.1 INTRODUCTION**

Successful development of energy storage technologies is critical to sustain our growth and progress as a society. The commercialization of zero-emission electric vehicles (EVs) will significantly decrease the volume of harmful pollutants produced by fossil fuel combustion, but it requires well-designed onboard batteries that must be safe, powerful, easy to manufacture, and be capable of enduring many cycles under a variety of operating conditions.<sup>5,6</sup> The batteries in the current portable electronics and for EVs must also satisfy the growing capacity demands for extended operating durations. The perennial issue remains that the typical insertion oxide cathodes (e.g., LiCoO<sub>2</sub>, LiMn<sub>2</sub>O<sub>4</sub>, and LiFePO<sub>4</sub>) for lithium-ion batteries suffer from limited capacity. As a result, the currently available high-capacity anode materials are underutilized because the oxide cathode capacities are limited to  $< 200 \text{ mAh g}^{-1}$ ,<sup>8</sup> prompting the investigation of next-generation of cathode technologies, *e. g.*, S and O<sub>2</sub> cathodes.<sup>6</sup> Since it is much easier to adapt the existing battery components to accommodate the solid sulfur materials than to reinvent the battery to utilize O<sub>2</sub> gas, sulfur is an ideal cathode material with a high theoretical gravimetric capacity (1675 mAh g<sup>-1</sup>) and energy density ( $\sim 2500 \text{ Wh kg}^{-1}$ ).<sup>159</sup>

Although sulfur cathodes have relatively large theoretical energy density, realizing their full capacity is difficult due to a notoriously poor active material utilization in Li-S cells, which stems from the low conductivity ( $5 \times 10^{-30} \text{ S cm}^{-1}$  at 25 °C) of sulfur.<sup>18</sup> Moreover, the intermediate polysulfides that form during the discharge/charge processes are easily soluble in the electrolyte.<sup>20</sup> The higher-order polysulfide ions (Li<sub>2</sub>S<sub>n</sub><sup>2-</sup>,  $2 < n \leq 8$ ) formed shuttle in the electrolyte between the anode and cathode,

leading to a rapid decline in Coulombic efficiency.<sup>26</sup> These shuttling species may be further converted into insulating lithium sulfide, which is then electroplated onto the lithium anode, resulting in an irreversible capacity fade.<sup>31,33</sup> Many approaches have been explored to tackle the drawbacks of sulfur cathodes, such as synthesizing carbon-sulfur composites<sup>36,51,55</sup> and applying surface coatings of conductive polymers.<sup>85,91</sup> The studies have shown promising improvements in Li-S batteries, but the material processing steps are often elaborate and costly, limiting the feasibility of manufacturing a viable lithium-sulfur cell.

In this study, we present a facile solution by inserting a bi-functional, conductive, porous multiwall carbon nanotube (MWCNT) paper between the cathode and the separator, which leads to an enhancement in both the specific capacity and cyclability of Li-S batteries. This free-standing MWCNT paper was first fabricated by an ultrasonic dispersion of synthesized MWCNTs, followed by a simple vacuum filtration without the addition of binders. After this simple treatment, a large piece of MWCNT paper was formed spontaneously and was easily peeled off the filtration membrane.<sup>79, 157</sup> A schematic illustration of this design of the lithium-sulfur cell configuration can be seen in Figure 5.1. The insertion of the MWCNT film in lithium-sulfur cells plays a key role in reducing the interfacial resistance in sulfur cathodes, and has the added advantage of localizing the polysulfides in the electrolyte, thus avoiding the unwanted migration and diffusion of the dissolved species to the anode. Former studies have demonstrated that carbon nanotubes are excellent substrates for growing sulfur-carbon nanotube composite materials with improved cycle performance.<sup>55</sup> Carbon nanotubes have not only superior electrically conductive network, but also a high tensile strength that stabilizes the cathode structure. This stability is especially critical to accommodate the severe volume change

that occurs in sulfur cathodes and prevent the structural failure in the electrodes during the discharge/charge process.<sup>31, 35</sup>

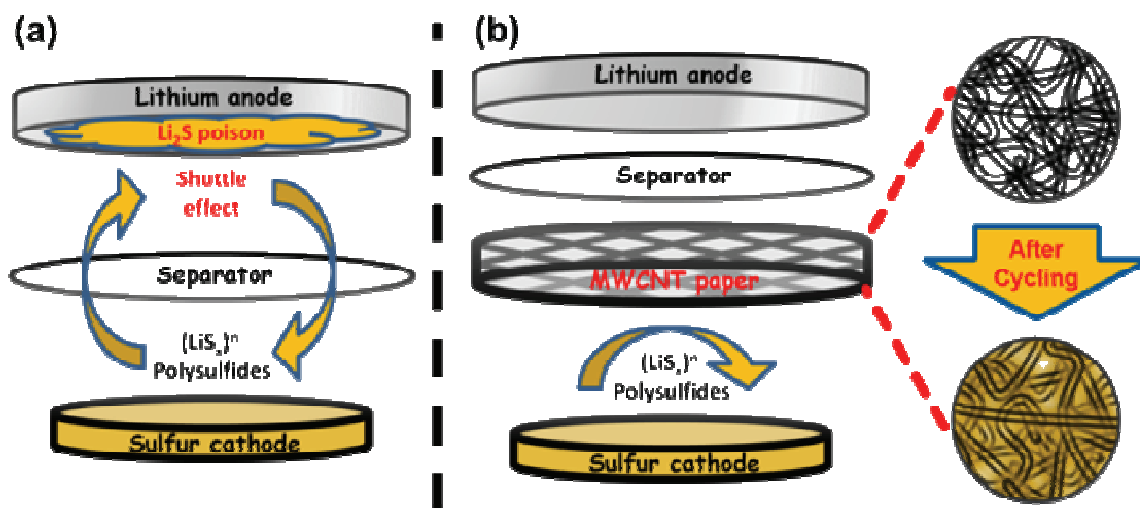


**Figure 5.1.** A schematic cell configuration of rechargeable Li-S batteries: (a) traditional configuration with severe shuttle effect and  $\text{Li}_2\text{S}$  poison problems and (b) new configuration with the MWCNT interlayer.

In addition, we found that not all carbon nanotubes have the ability to form free-standing films through a “self-weaving” behavior. By the same method, a different type of commercial MWCNT with an absolutely straight tube structure failed to form a binder-free film. The tube shapes could be visualized with a scanning transmission electron microscope (STEM), and Figure 5.2 reveals that the as-synthesized MWCNT exhibits distinct curvature while the commercial MWCNT is straight. The bent structure of MWCNTs may occur when partial defects occur on the graphene walls or when the MWCNTs have a few graphene layers constituting the tube due to the low elastic modulus. The unique properties of curved walls allow the MWCNTs to easily intertwine with one another.<sup>79</sup> Figure 5.3 shows the Raman spectra of the commercial MWCNTs with straight tubes and as-synthesized MWCNTs with curved tubes, where the ratio

between the relative intensities of the D-band ( $I_D$ , at  $1340\text{ cm}^{-1}$ ) and G-band ( $I_G$ , at  $1570\text{ cm}^{-1}$ ) are compared.<sup>160</sup> The  $I_D/I_G$  value is an index of the degree of graphitization and can be used to estimate the number of defects in carbon nanotubes. The  $I_D/I_G$  is 0.95 for the as-synthesized MWCNTs; in contrast, the commercial MWCNTs possess a smaller  $I_D/I_G$  value of 0.34, indicating a lack of defects located in the lattice on the wall or edge, which leads to a mostly straight tube shape. In fact, the bent structure in MWCNTs may only exist when partial defects occur on the graphene walls, which is essential to the self-weaving behavior. The unique property of curved walls allows the MWCNTs to easily intertwine with one another. In a previous report, the  $I_D$  of the free-standing MWCNT anode film was even higher than its  $I_G$  ( $I_D/I_G > 1$ ).<sup>79</sup> For the purposes of this study, the  $I_D/I_G$  ratio was maintained at a sufficiently low level as to obtain the necessary degree of graphitization for superior electrical conductivity.

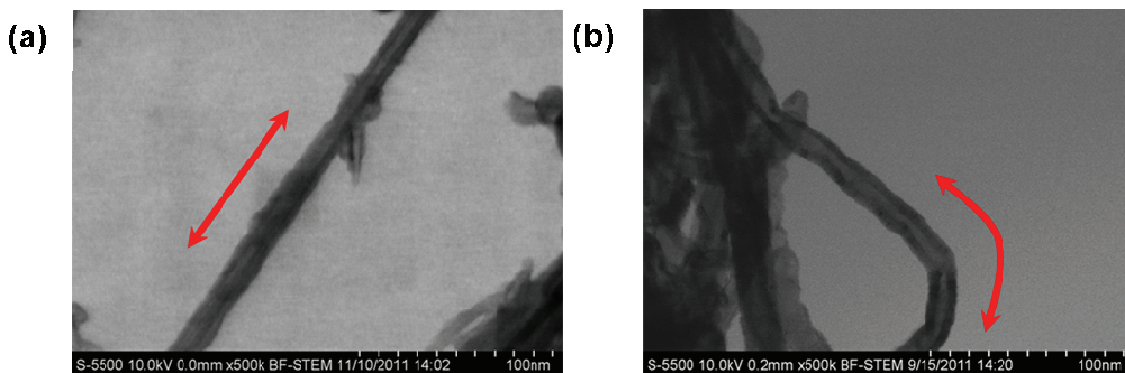


**Figure 5.2.** Scanning transmission electron microscopy (STEM) images of two different MWCNTs: (a) commercial MWCNTs with a straight tube structure and (b) as-synthesized MWCNTs with a curved tube structure used in this study.

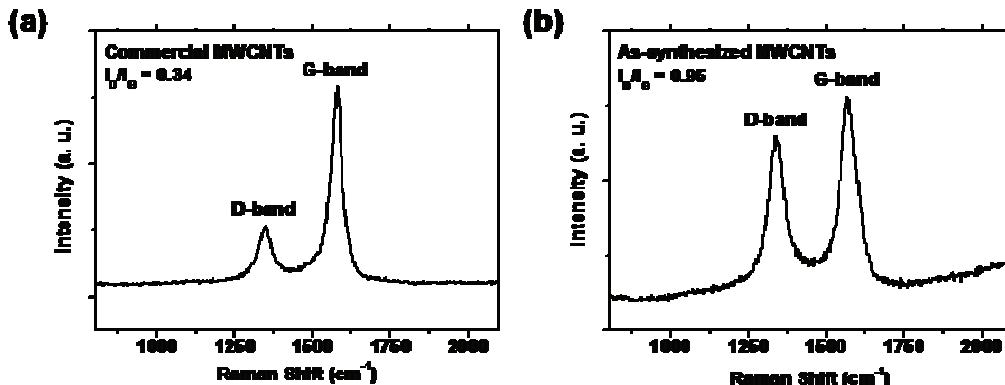


**Figure 5.3.** Raman spectra of (a) commercial MWCNTs and (b) as-synthesized MWCNTs used in this study. The defect level of MWCNTs can be evaluated by the  $I_D/I_G$  ratio.

## 5.2 EXPERIMENTAL

### 5.2.1 Synthesis and interlayer fabrication

Pristine MWCNTs with a diameter of 10 – 20 nm were synthesized by a chemical vapor deposition (CVD) process. To fabricate the free-standing MWCNT paper, 75 mg of the as-synthesized MWCNTs were dispersed in 750 mL of deionized water by high-power ultrasonication for 15 minutes with the addition of 20 mL of isopropyl alcohol to wet the MWCNTs. The products were collected by vacuum filtration and washed with deionized water, ethanol, and acetone several times. The free-standing MWCNT paper thus formed was a flexible film after drying for 24 h at 50 °C in an air-oven, which could be easily peeled off the filter membrane. The binder-free MWCNT paper was then punched out in circular disks with a 3/8 inch diameter, 40 – 50 micron thickness, and around 0.6 – 0.8 mg mass for the interlayer in lithium-sulfur cells. Commercial MWCNTs with a similar diameter and length were used as purchased from Nanostructured & Amorphous Materials, USA. Pure sulfur for the active material of sulfur cathodes was synthesized first by mixing sodium thiosulfate ( $\text{Na}_2\text{S}_2\text{O}_3$ ; Fisher

scientific) and hydrochloric acid (HCl; Fisher Scientific) in aqueous solution for 24 h under strong stirring, followed by filtering and washing the precipitate formed until the pH reached 7. The sulfur powder was dried for 24 h at 50 °C in an air-oven before use.

### **5.2.2 Microstructure and elemental analysis**

The microstructure images of the samples were taken with a FEI Quanta 650 scanning electron microscope (SEM) and a Hitachi S-5500 SEM equipped with a scanning transmission electron microscope (STEM). The elemental mapping results were examined with an energy dispersive spectrometer (EDS) attached to the FEI Quanta 650 SEM. A Raman microscope (Renishaw, inVia Reflex) with a 514.5 nm green laser and a 50 × aperture was employed to obtain the Raman scattering spectra.

### **5.2.3 Electrochemical analysis**

The as-synthesized sulfur powder was mixed with 20 wt. % of carbon black (Super P) and 10 wt. % of polyvinylidene fluoride (PVDF; Kureha) binder in an *N*-methylpyrrolidinone (NMP; Sigma-Aldrich) solution. The well-mixed slurry was tape-casted onto a sheet of aluminum foil and the film was dried in a convection air-oven for 24 h at 50 °C, followed by pressing with a roller and punching out circular electrodes of a 1/4 inch diameter. The cathode electrode disks were dried in a vacuum oven for an hour at 50 °C before assembling the cell. A 1.85 M LiCF<sub>3</sub>SO<sub>3</sub> solution was prepared with a mixture of 1,2-Dimethoxyethane (DME; Acros) and 1,3-Dioxolane (DOL; Acros) (1:1, v/v) as the electrolyte. LiNO<sub>3</sub> salt (Acros) was added into the electrolyte to enhance the Coulombic efficiency of the cells during high rate cycle testing. CR2032 coin cells were assembled with the pure sulfur cathodes, prepared electrolyte, MWCNT interlayers, Celgard polypropylene separators, lithium metal anodes, and nickel foam spacers in a glove box filled with argon. The discharge/charge profiles and cycle life data were

obtained with a battery cycler (Arbin Instruments). The C rates specified in this study are based on the mass and theoretical capacity of sulfur ( $1675 \text{ mA g}^{-1}$ ). Electrochemical impedance spectroscopy (EIS) data were collected with a Solartron Impedance Analyzer (SI 1260 + SI 1287) from 1 MHz to 100 mHz with an AC voltage amplitude of 5 mV at the open-circuit voltage of the coin cells. The cyclic voltammetry (CV) data were collected with a VoltaLab PGZ 402 Potentiostat at a scan rate of 0.2 mV/s in the potential range of 2.8 – 1.5 V by measuring the cell with a  $\text{LiNO}_3$ -free electrolyte.

## 5.3 RESULTS AND DISCUSSION

### 5.3.1 Electrochemical characterizations

Figure 5.4(a) shows the cyclability profile of the Li-S batteries with and without the insertion of the MWCNT paper. With the MWCNT interlayer, the initial discharge capacity of the cell is  $1446 \text{ mAh g}^{-1}$ , which is 86% of the theoretical capacity of sulfur, and more than twice that of the raw lithium-sulfur cell ( $671 \text{ mAh g}^{-1}$ ). Electrochemical impedance spectroscopy (EIS) is a powerful tool to investigate the internal resistance of Li-S batteries.<sup>11</sup> The diameter of the semicircular portions of the curves in Figure 5.4(b) represents the charge transfer resistance ( $R_{ct}$ ), which is mainly generated at the interface between the electrode and the electrolyte.<sup>11</sup> After the addition of the MWCNT paper, the  $R_{ct}$  value is dramatically decreased from 277 to  $38 \text{ } \Omega \text{ cm}^2$  (calculated after the electrode area normalization). The conductive interlayer acts as a pseudo-upper current collector, reducing the effective resistance from the highly insulating sulfur cathodes. Therefore, the huge enhancement in the active utilization can be attributed to the electrode surface in nanoscale contact with the conductive network of the MWCNT paper, which allows electrons to flow freely through the cathode and accelerates the kinetics of the electrochemical reactions.

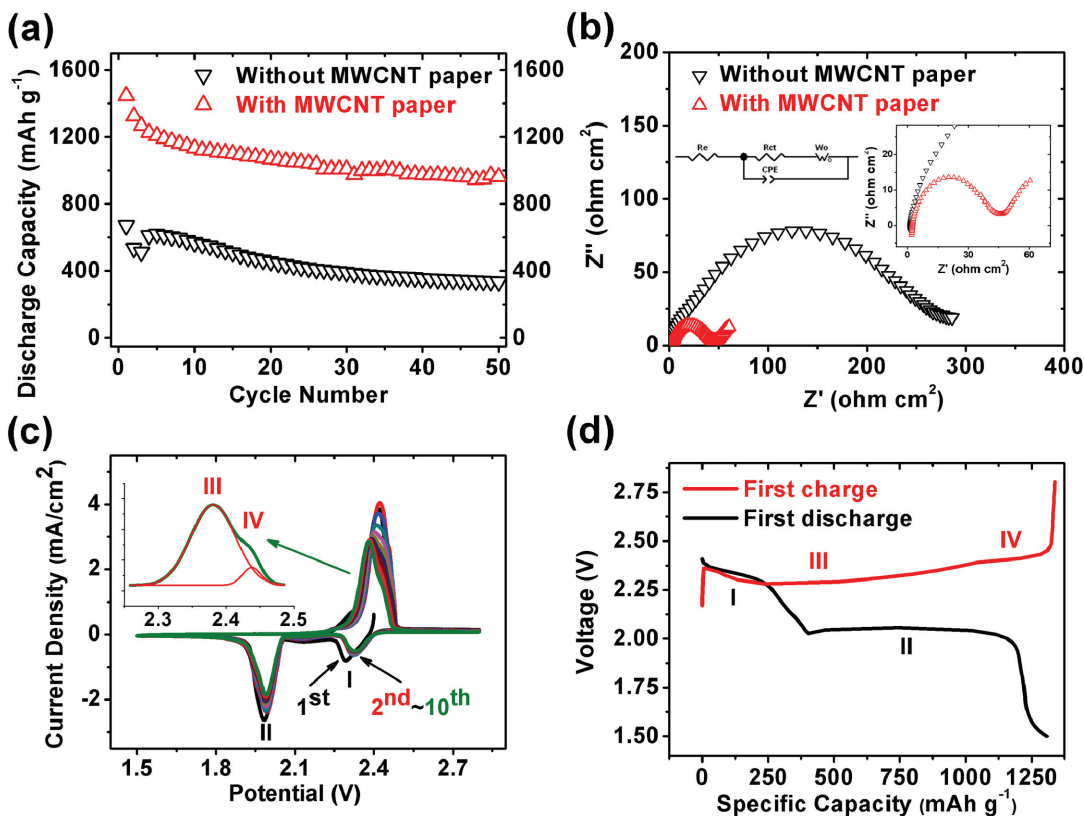


**Figure 5.4.** Electrochemical data of the Li-S cells: (a) cyclability of the cells at C/5 rate, (b) area-normalized Nyquist plots of the cells measured before cycling, (c) CV plots of the modified cell (first 10 cycles), and (d) discharge/charge profiles of the modified cell at 1C rate.

The lithium-sulfur cell with the MWCNT interlayer (Figure 5.4(a)) also exhibits excellent cycling stability, with the specific capacity remaining high at  $962 \text{ mAh g}^{-1}$  after the 50<sup>th</sup> cycle at a current density of  $335 \text{ mA g}^{-1}$  (C/5,  $C = 1675 \text{ mA g}^{-1}$ ). In contrast, the raw lithium-sulfur cell shows only  $\sim 330 \text{ mAh g}^{-1}$  after 50 cycles under the same cycling conditions. The cyclic voltammetry (CV) scans of the Li-S battery with the MWCNT interlayer (Figure 5.4(c)) nearly overlap for the first ten cycles without any obvious change in peak intensities or locations, demonstrating the excellent cycle stability of this system. The slight overpotential of the first reduction peak (I) is eliminated after the first

cycle due to the rearrangement of active sulfur from its original positions to more energetically stable sites with lower resistance. The two reduction peaks (I & II) are consistent with the two discharge plateaus (I & II) in the discharge/charge profiles (Figure 5.4(d)). Similarly, the two oxidation peaks (III & IV) correspond to the two charge plateaus (III & IV) as well. Plateau I is attributed to the reduction of elemental sulfur ( $S_8$ ) to soluble polysulfides ( $Li_2S_4$ ). Plateau II is regarded to correspond to the formation of solid  $Li_2S$ , and Plateau III represents the backward reaction from  $Li_2S$  to  $Li_2S_4$ . Plateau IV is ascribed to the oxidation of  $Li_2S_4$  to  $Li_2S_8/S$ . This two-step electrochemical reaction observed in the discharge and charge processes is typical of Li-S batteries.<sup>7, 11</sup> A small discharge plateau is found at the end of the discharge process, which can be ascribed to the irreversible reduction of  $LiNO_3$  in the electrolyte.<sup>130</sup>

### 5.3.2 Morphological change during cycling

To further investigate the reason why a simple porous interlayer can considerably advance the performance of the Li-S battery cells, an ex situ scanning electron microscope (SEM) analysis was carried out on cycled electrodes. The microstructure image of the as-synthesized free-standing MWCNT paper with a porous structure is shown in Figure 5.5(a), where circuitous carbon nanotubes interlace. Porosity of the interlayer is important because electrolyte must permeate through the layer to allow electrochemical reactions to proceed in the cathode. Also, the tortuous pores in the paper can localize the polysulfide species diffusing from the cathode and the MWCNT skeleton is able to endure the volume change of trapped active material during cycling due to its unique mechanical properties. The appearance of the MWCNT film covering the electrode after 100 cycles (Figure 5.5(b)) demonstrates a build-up of the active material, indicating that the carbon nanotubes act as a matrix to capture and retain the polysulfide

species by electrochemical deposition at the end of discharge/charge and work as second redox reaction sites. By inspection, it is clear that the tube size swelled after cycling as shown in Figure 5.5(d) compared to that before cycling as exhibited in Figure 5.5(c), which proves the excellent capability of the MWCNTs to trap polysulfides. Figure 5.5(e) indicates the elemental mapping of the cycled electrode covered by the MWCNT paper, where sulfur is distributed homogeneously throughout the MWCNT interlayer. Although a portion of the active material might form an agglomeration in the interlayer network (Figure 5.6), electrons can still easily pass through the insulating bulk via the MWCNTs penetrating inside the inactive region to activate discharge/charge reactions. Dispersing active material in the sturdy conductive framework homogeneously is key to ensuring the cycle stability of Li-S batteries,<sup>31, 33, 55</sup> and the design of the interlayer allows the cathode region to maintain a stable structure with trapped polysulfide species.

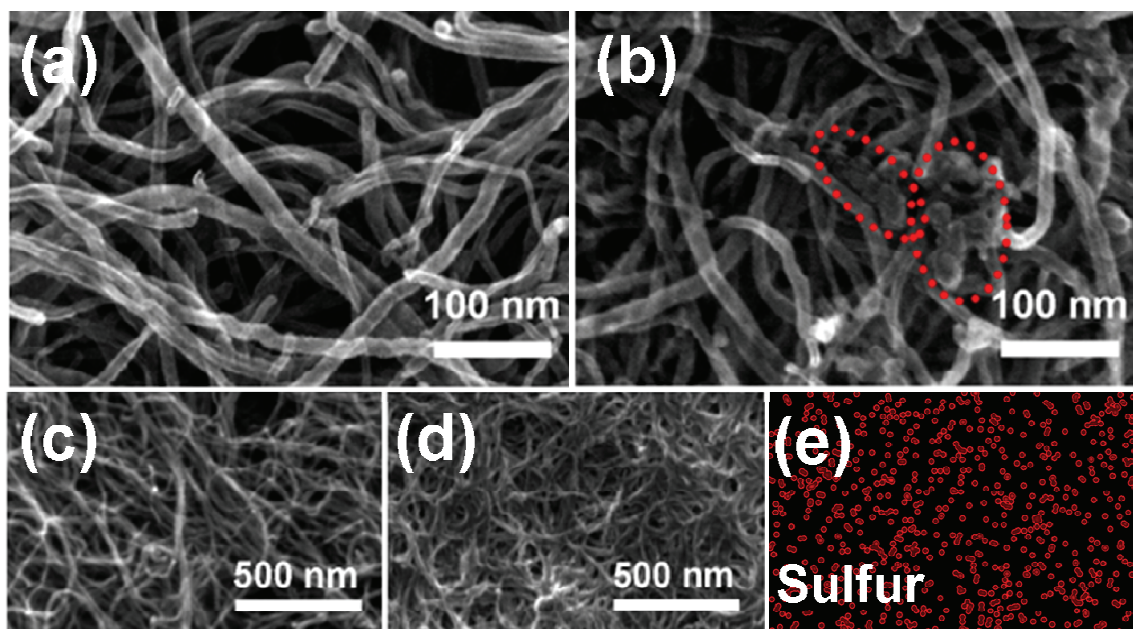


**Figure 5.5.** Morphology of the MWCNT paper: (a) before cycling and (b) after 100 cycles at 1C rate, (c) raw tube structure before cycling, (d) swollen tube structure after cycling, and (e) elemental mapping of (c).

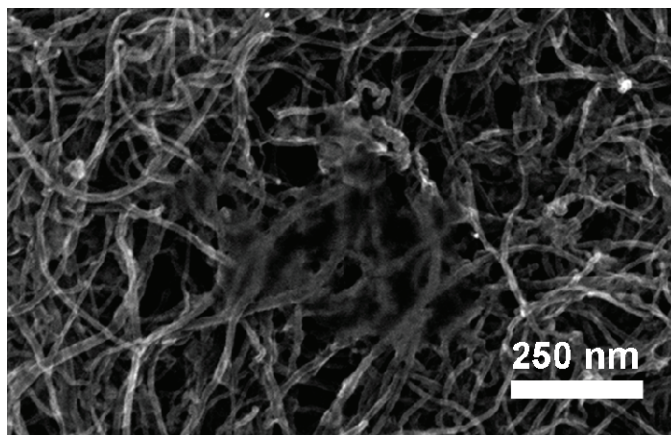


**Figure 5.6** Morphology of the free-standing MWCNT paper covering sulfur electrodes after 50 cycles at  $C/2$  rate, illustrating the embedding of the agglomerated active material within the MWCNTs.

### 5.3.3 Cycle performance

The Li/MWCNT interlayer/S battery system also performs well in high rate applications. At discharge/charge rates of  $C/2$  and  $1 C$ , the cells maintain high capacities of  $855$  and  $804 \text{ mAh g}^{-1}$ , respectively, after 100 cycles (Figure 5.7). Our design effectively enhances the rate performance of lithium-sulfur cells. The highly conductive MWCNT interlayer effectively promotes rapid electrochemical reactions in Li-S batteries due to the descending interfacial resistance and abundant reaction sites introduced from the MWCNTs. As a result, the insertion of a MWCNT paper is a facile configuration modification in Li-S batteries to improve the rate capability.

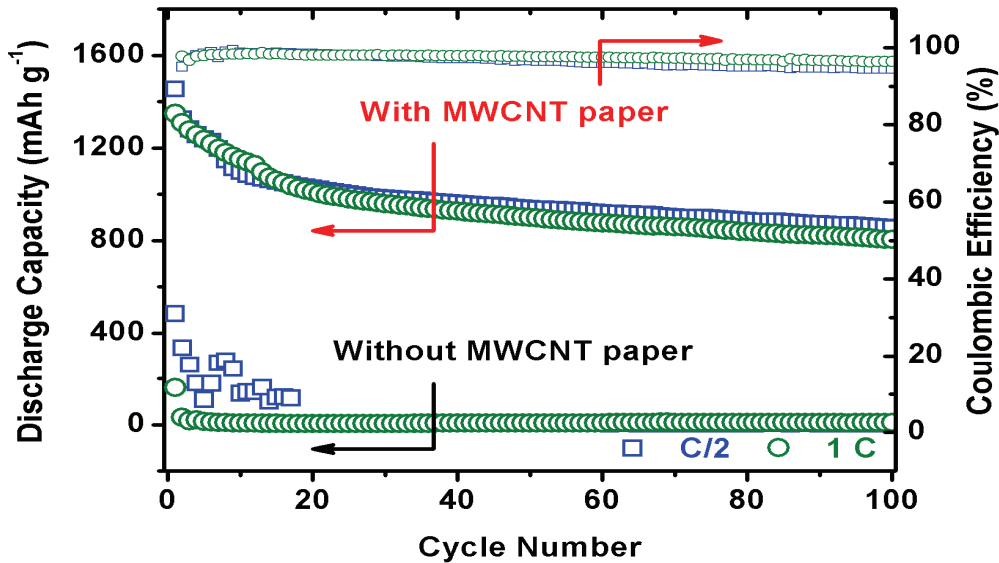


**Figure 5.7.** High-rate cycle performance and Coulombic efficiency of the lithium-sulfur cells with and without the MWCNT interlayer.

The Coulombic efficiency, which is calculated by dividing the discharge capacity by the previous charge capacity, could be improved by the incorporation of nitrate salts into the electrolyte.<sup>26</sup> With the addition of 0.1 M LiNO<sub>3</sub> salt, the Coulombic efficiency increases to 98% (Figure 5.8). Nitrate anions are a proven passivator of lithium metal anodes, which mitigates issues arising with corrosion and shuttle effect from the migrating polysulfides.<sup>34</sup> The average Coulombic efficiency of lithium-sulfur cells with the MWCNT interlayer at C/2 and 1 C is above 96% for 100 cycles (Figure 5.7). Charge efficiency and high-speed charging are two critical factors for EV batteries, and the improvement in Coulombic efficiency and superb high rate cycle performance presented here boost the prospects of the Li-S battery as a promising candidate for EV applications.

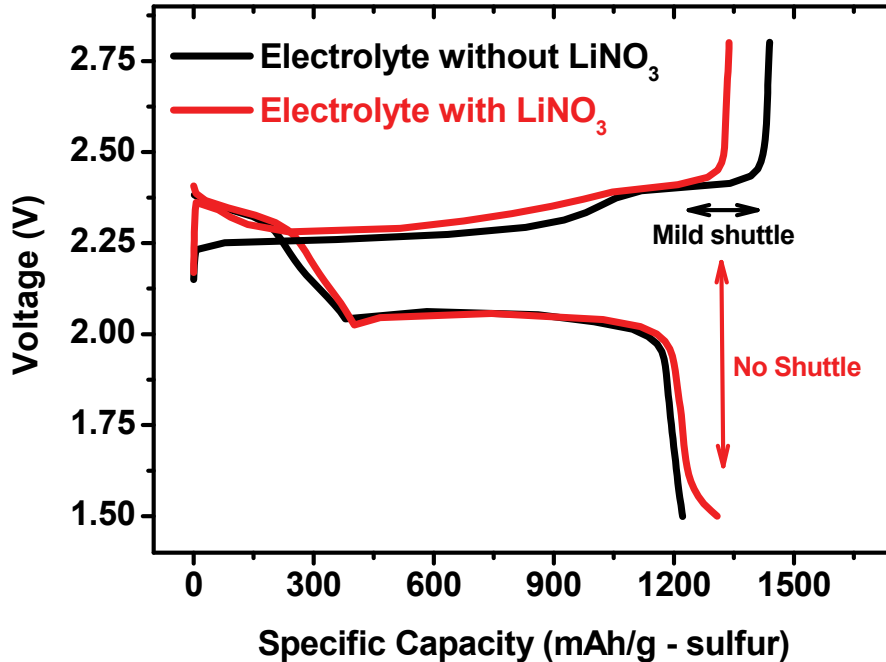


**Figure 5.8.** Discharge/charge profiles of the Li/MWCNT interlayer/S battery with different electrolytes cycled at 1 C. The addition of  $\text{LiNO}_3$  in the electrolyte improves the Coulombic efficiency (the ratio of discharge capacity to charge capacity) of lithium-sulfur cells up to 98%.

#### 5.4 CONCLUSIONS

In conclusion, the novel configuration of inserting a free-standing MWCNT paper in the Li-S battery significantly enhances both the specific capacity and cycle stability. This study demonstrates that complex synthesis and surface modification are not necessary to achieve high-performance Li-S cells. The conductive MWCNT interlayer as a pseudo-upper current collector not only reduces the charge transfer resistance of sulfur cathodes significantly, but also captures the migrating active material at the end of cycles. The increased electrical conductivity promotes efficient active material utilization and stable high rate battery performance with long cycle life. In addition, the porous MWCNT paper offers the advantage of serving as an excellent matrix to retain and

accommodate dissolved intermediate polysulfides. The design of inserting a conductive carbon interlayer in Li-S batteries is a feasible new approach, and it can be modified with other types of functional carbon materials to further optimize the battery performance.

## Chapter 6: Lithium-sulfur batteries with a microporous carbon paper as a bi-functional interlayer

### 6.1 INTRODUCTION

The early-stage research in lithium-sulfur batteries was initiated three decades ago,<sup>20, 25</sup> but the spotlight did not return to this battery system until there was a renewed interest in electric vehicles (EVs) in recent years. The major impediments to the development of Li-S batteries are low active material utilization, poor cycle life, and low charge efficiency.<sup>7</sup> The poor utilization of active material results from the insulating sulfur, which hinders the electron transfer during electrochemical reactions. Also, sulfur molecules form easily-dissolved polysulfide intermediates with lithium ( $\text{Li}_2\text{S}_x$ ,  $2 < x \leq 8$ ) in the electrolyte, resulting in severe capacity fade.<sup>32, 33</sup> The soluble polysulfides shuttling between the anode and cathode lead to low Coulombic efficiency.<sup>26, 27</sup> Thus, improving the conductivity of the sulfur cathode and maintaining/reutilizing soluble polysulfides within the cathode structure are critical to develop a viable Li-S system.

Employing sulfur-carbon composites and applying conductive polymer surface modification are the main approaches in laboratories around the world to realize high capacity and improved cycle life.<sup>29, 36, 37, 40, 44, 51, 62, 81, 86, 91, 102, 150</sup> Both approaches enhance the electrical conductivity of the cathode and suppress the loss of soluble polysulfide intermediates during cycling and thereby improve the active material utilization and cyclability. In addition, the issue of low Coulombic efficiency has been resolved by the addition of lithium nitrate to the electrolyte.<sup>34, 62</sup> As discussed, the major stream of Li-S battery research has focused on the modification “inside” of the cathode and electrolyte, but the design “outside” of the cathode such as cell configuration could be a new strategy for improving the performance of Li-S batteries.

Based on the fact that porous carbon plays a key role, both as electron pathways and as traps for dissolved polysulfide species, we present here an insertion of an electrolyte-permeable microporous carbon paper (MCP) between the separator and cathode disk to improve the electrochemical performance of Li-S cells. This design of cell configuration can effectively decrease the resistance of sulfur cathodes, resulting in an enhancement of active material utilization. Additionally, the carbon interlayer with micropores used in this study facilitates the absorption of soluble polysulfides shuttling in the electrolyte and makes them available to be reutilized even during long cycles. This bi-functional carbon interlayer can be treated as a second current collector for accommodating the migrating active material from sulfur cathodes. This novel approach not only simplifies the battery processing without elaborate synthesis of composites and surface chemistry modification, but also improves the capacity and cycle life, thereby promoting the practicality of Li-S batteries.

## **6.2 EXPERIMENTAL**

### **6.2.1 Synthesis and characterizations**

The MCP samples were prepared by mixing conductive carbon black with high surface area (Black Pearls<sup>®</sup> 2000, CABOT) and polytetrafluoroethylene binder at a 3:2 mass ratio with a small amount of isopropyl alcohol in a mortar, followed by roll-pressing and cutting into circular films. The microstructure of the samples was examined with a FEI Quanta 650 SEM and a JEOL JEM-2010F transmission electron microscope (TEM). Brunauer–Emmett–Teller (BET) surface area measurements were carried out with a volumetric sorption analyzer (NOVA 2000, Quantachrome) using physical adsorption/desorption of nitrogen gas at the liquid-nitrogen temperature. Pore

size distributions were calculated according to the Barrett-Joyner-Halenda (BJH) method. Micropore surface area and volume were estimated by t-plot method.

### **6.2.2 Cell assembly**

Sulfur cathode slurry was fabricated by mixing 70 wt. % of precipitated sulfur, 20 wt. % of carbon black (Super P), and 10 wt. % of polyvinylidene fluoride (PVDF; Kureha) binder in an *N*-methylpyrrolidinone (NMP; Sigma-Aldrich) solution overnight. The slurry was tape-casted onto an aluminum foil and dried in an air-oven for 24 h at 50 °C, followed by roll-pressing and cutting into circular electrodes. The cathode disks and MCP interlayers were dried in a vacuum oven for an hour at 50 °C before assembling the cell. The electrolyte was prepared by adding 1.85 M LiCF<sub>3</sub>SO<sub>3</sub> (Acros Organics) and 0.1 M LiNO<sub>3</sub> (Acros Organics) salts into a mixture of 1,2-Dimethoxyethane (DME; Acros Organics) and 1,3-Dioxolane (DOL; Acros Organics) at a 1:1 volume ratio. CR2032 coin cells were assembled with the sulfur cathodes, prepared electrolyte, MCP interlayers, polypropylene separators (Celgard), and lithium foils (Aldrich).

### **6.2.3 Electrochemistry**

Electrochemical impedance spectroscopy (EIS) data were obtained with a Solartron Impedance Analyzer (SI 1260 + SI 1287) from 1 MHz to 100 mHz with an AC voltage amplitude of 5 mV at the open-circuit voltage of the cells with the Li metal foil as both auxiliary and reference electrodes. Discharge/charge profiles and cycle data were collected with a programmable battery cycler (Arbin Instruments). The CV plots were collected with a VoltaLab PGZ 402 Potentiostat at a scan rate of 0.2 mV/s in the voltage window of 2.8 – 1.5 V. Morphological characterization and elemental mapping of the MCP samples before and after cycling were carried out with a Hitachi S-5500 SEM equipped with an energy dispersive spectrometer (EDS).

## 6.3 RESULTS AND DISCUSSION

### 6.3.1 Cell configuration of the Li / MCP interlayer / S battery

The battery configuration of a Li-S cell with a bi-functional microporous carbon interlayer is displayed in Figure 6.1(a). The conductive carbon interlayer has to be placed between the separator and cathode in order to capture the migrating polysulfides ( $\text{Li}_2\text{S}_x$ ) from the cathode during electrochemical reactions, but without contacting the lithium anode. Here we employ pure sulfur powder as the active material to make conventional sulfur cathodes instead of using specialized composites or adopting any surface chemistry modification in order to demonstrate that the observed improvement in cyclability is only contributed by the carbon interlayer. Figure 6.1(b) shows the scanning electron microscope (SEM) image of the MCP used in this study as the interlayer. It can be seen that the carbon particles in the film is nano-sized, which is able to provide subtle surface contact with the sulfur cathode to reduce the electrical resistance. In addition, the interlayer surface is highly porous, resulting in good electrolyte penetration during cycling. The particle size of the carbon nanoparticles in the MCP ranges between 20 – 40 nm (Figure 6.1(c)), and no mesopores with a diameter  $> 5$  nm can be found in the carbon.

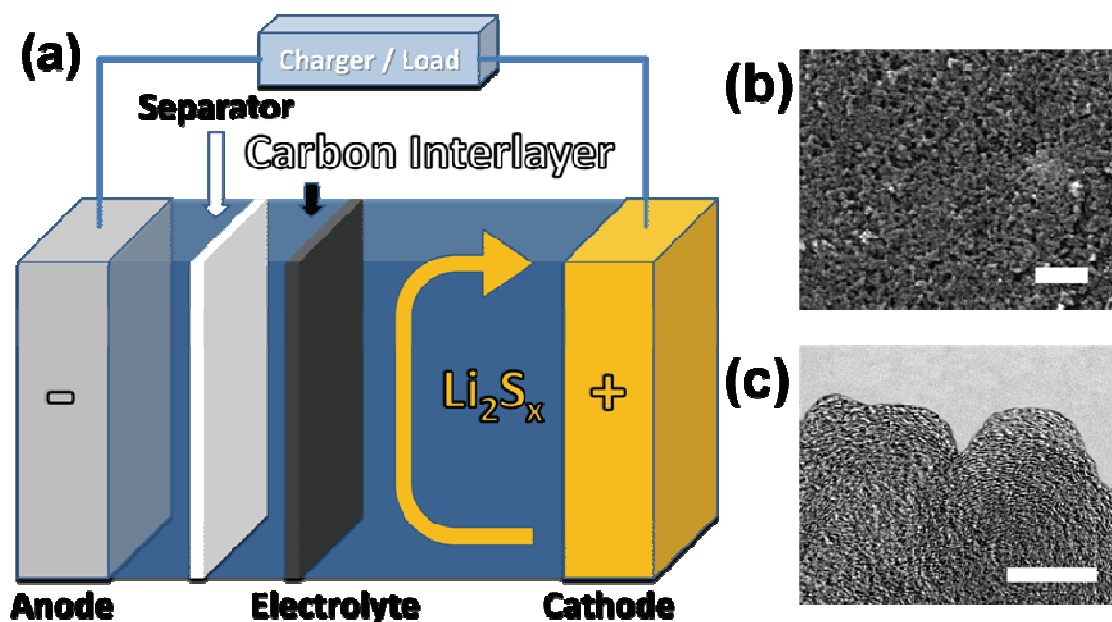


**Figure 6.1.** Scheme and morphology of the MCP employed in the Li-S battery. (a) Schematic configuration of a Li-S cell with a bi-functional carbon interlayer with micropores inserted between the sulfur cathode and the separator, (b) SEM image of the surface of the MCP, and (c) TEM image of the microporous carbon particles. The scale bars in b and c represent, respectively, 500 and 10 nm.

### 6.3.2 Pore-filling process of the MCP interlayer during cycling

The nitrogen adsorption/desorption isotherms of MCP as the interlayer in Li-S batteries before and after cycling is displayed in Figure 6.2(a). It can be seen that both the microporous carbon powder and MCP exhibit mixed type I and type II isotherms, respectively, for low relative pressure ( $P/P_0$ ) and high  $P/P_0$ .<sup>161, 162</sup> The raw microporous carbon powder and MCP have certain nitrogen adsorption below the relative pressure of  $P/P_0 < 0.1$ , indicating the existence of micropores.<sup>161</sup> The rise after  $P/P_0 > 0.9$  represents the integral porosity of MCP contributed by the interspaces between the carbon nanoparticles, offering abundant channels for liquid electrolyte. The amount of mesopores is limited because of the gentle adsorption slope at  $P/P_0 = 0.1 - 0.9$ . The MCP

as the interlayer after cycling shows almost zero adsorption at the micropore region, demonstrating that these micropores are filled during the discharge/charge of the Li-S cells. A depletion of the hysteresis loop is found in the cycled MCP, also indicating a portion of mesopores are filled. The total surface area of pristine MCP is as high as  $695 \text{ m}^2 \text{ g}^{-1}$  (65% contributed by micropores), but that of the MCP after cycling is only  $61 \text{ m}^2 \text{ g}^{-1}$  due to the filling of the pores in the interlayer. The total pore volume of MCP after 100 cycles is as low as  $0.288 \text{ cm}^3 \text{ g}^{-1}$  (no micropore volume), which is much less than that of pristine MCP ( $1.194 \text{ cm}^3 \text{ g}^{-1}$ ;  $0.215 \text{ cm}^3 \text{ g}^{-1}$  for micropore volume). Figure 6.2(b) exhibits the pore size distributions of the MCP samples, where all specimens have no obvious pores with a diameter over 5 nm. These curves end at the pore diameter below 1.4 nm due to the limitation of the analyzer. The microporous/small-mesoporous peak of the MCP almost vanishes after cycling, implying that the migrating active polysulfides might be captured and fill these pores during the electrochemical cycling.

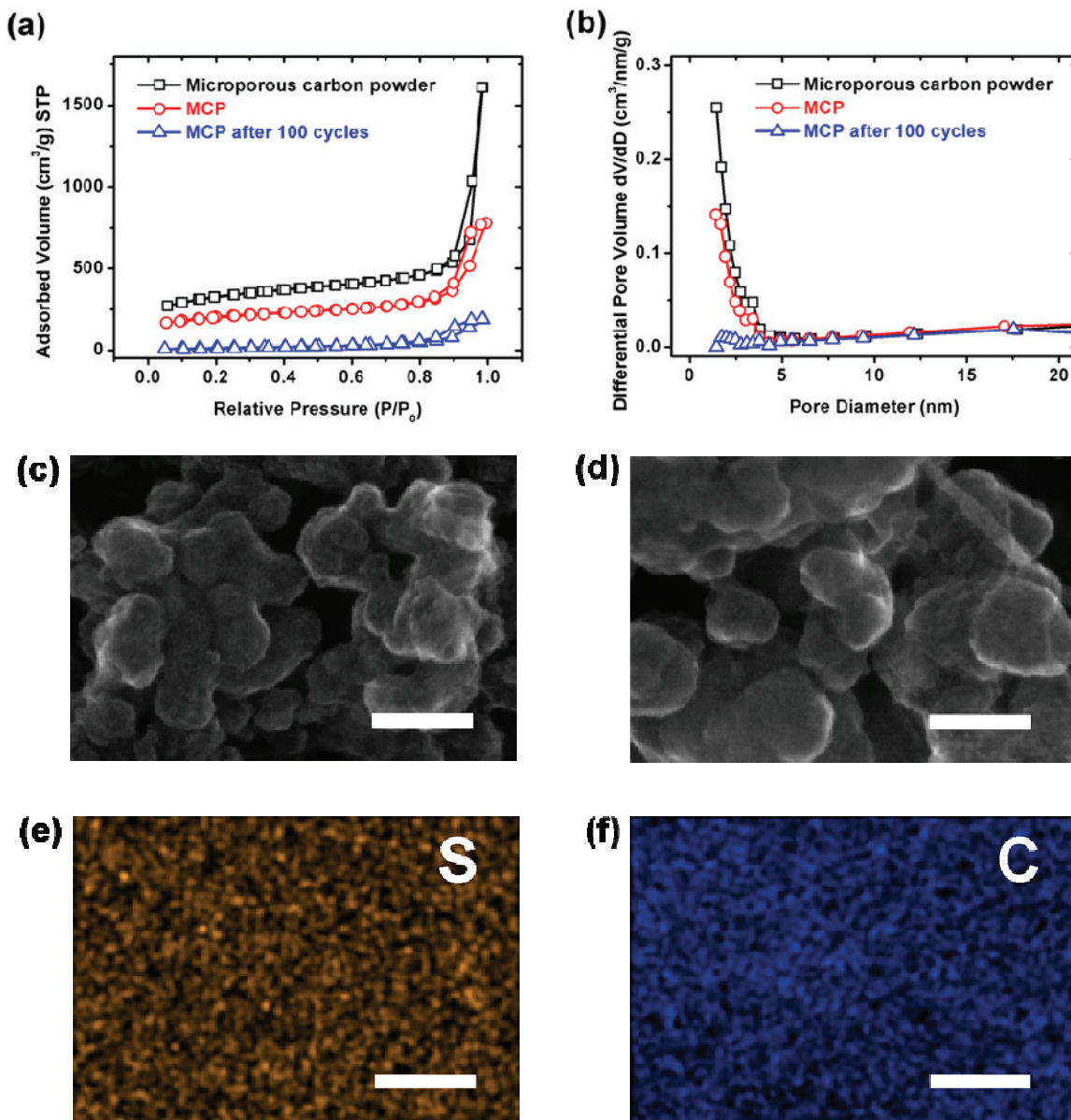


**Figure 6.2.** Nitrogen adsorption/desorption analysis, SEM images, and EDS mapping results of the MCP: (a) Isotherms and (b) pore size distributions of the microporous carbon powder, MCP, and MCP as an interlayer in the Li-S cell at 1C rate after 100 cycles. SEM images of the MCP (c) before cycling and (d) after cycling. Elemental mapping of (e) sulfur and (f) carbon in (d). The scale bars in c-f represent 50 nm.

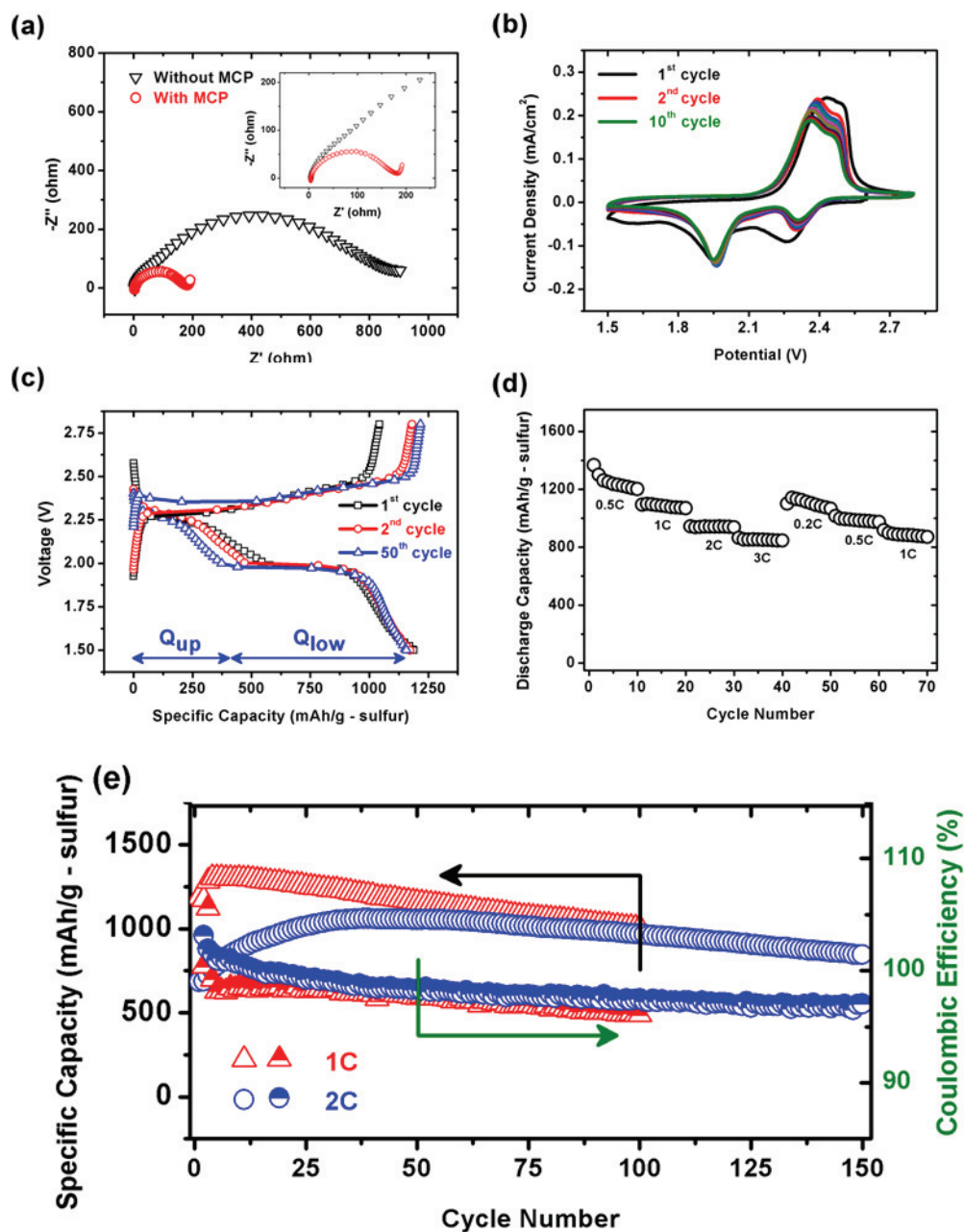
### **6.3.3 Surface morphology and elemental analysis of the MCP interlayer**

Figure 6.2(c) and 6.2(d) compare the SEM images of the MCP interlayer surface towards the cathode before and after cycling. Pristine MCP in Figure 6.2(c) exhibits a morphology of glue-like particles composed of microporous carbon and binder. The MCP after 100 cycles still has spherical morphology with individual microporous carbon particles, showing that the dissolved active material is probably absorbed by the pores in the interlayer rather than forming large insulating sulfur/lithium sulfide inactive layers. This feature is critical because irreversible capacity loss would occur if active material agglomerates and non-uniformly covers the cathode, which can block charge transfer reactions and ion transport in the cell.<sup>32,33</sup> The surface porosity of the MCP after cycling is still maintained, which guarantees the infiltration of electrolyte. Figure 6.2(e) and 6.2(f) display the elemental mapping results of the MCP interlayer after cycling. Sulfur signal is found all-over the carbon interlayer and distributed homogeneously, ensuring a superior reutilization of the active material and reversibility. Moreover, it is noteworthy to mention that the carbon signal is also well-distributed and strong in the interlayer, indicating that the conductive carbon is not severely covered by sulfur/sulfides and leading to good conductivity in the cathode region even for long cycles.

### **6.3.4 Electrochemical performance of the Li-S batteries with the MCP interlayer**

To analyze the impact of the MCP as the carbon interlayer in Li-S batteries, impedance analysis was performed to compare the cells with and without the MCP interlayer before cycling (Figure 6.3(a)). The impedance of Li-S batteries located in the high frequency region is regarded as the charge transfer resistance of the cell.<sup>11</sup> The impedance semicircle shrinks significantly by about 79% after the insertion of the MCP, demonstrating a dramatic decrease in the charge transfer resistance of the battery. Here, the MCP interlayer works as an upper current collector for the low-conductivity sulfur

cathode, enhancing the active material utilization and thereby raising the specific capacity of the cell. Figure 6.3(b) shows the cyclic voltammograms (CV) of the cell with the MCP for the first ten cycles. Two cathodic peaks at around 2.3 and 2.0 V and the two overlapped anodic peaks at around 2.35 and 2.45 V are typical of Li-S cells with carbon-based cathodes.<sup>29, 51</sup> The overpotential of the first cathodic peak disappears after the first cycle possibly due to the rearrangement of the migrating active material to electrochemically favorable positions. The discharge/charge profiles in Figure 6.3(c), exhibiting two discharge plateaus and two closely-spaced charge plateaus, are consistent with the CV plots. The upper discharge plateau represents the transformation of sulfur into long-chain polysulfides and the lower discharge plateau represents the conversion of short-chain polysulfides ( $\text{Li}_2\text{S}$ ), which are reminiscent in the charge plateaus as well.<sup>7</sup> The discharge capacity values of the cell at the first, second, and 50<sup>th</sup> cycle at 1C rate are identical except for the length ratio between the upper ( $Q_{\text{up}}$ ) and lower ( $Q_{\text{low}}$ ) plateaus. A much higher  $Q_{\text{low}}/Q_{\text{up}}$  ratio of 2.10 can be observed in the cell after 50 cycles compared with that after the first cycle ( $Q_{\text{low}}/Q_{\text{up}} = 1.06$ ). As the representative microporous carbon-sulfur composite cathodes exhibit only the lower discharge plateau during cycling,<sup>37, 40</sup> the stretching  $Q_{\text{low}}$  corresponds to the capacity contribution from the micropores-trapped active material. Additionally, it appears that the active material needs to take a few cycles to reach a steady state in the cathode region to offer stable electrochemical performance because of the solubility of the intermediate lithium polysulfides in the electrolyte.<sup>81</sup> The inactive core of sulfur cannot be reutilized until it becomes exposed to the electrolyte after the initial cycles at high C rates,<sup>158</sup> which is evident in the second cycle where the discharge capacity is even higher than the first charge capacity (Figure 6.3(c)).



**Figure 6.3.** Electrochemical measurements of Li-S batteries: (a) EIS plots of Li-S cells with and without MCP, (b) CV scans, (c) discharge/charge profiles at various cycles, (d) rate capability up to 3C, and (e) cycle life and Coulombic efficiency of the cell with MCP at 1C and 2C for long cycles.

The rate capability of the cell with the MCP is shown in Figure 6.3(d). The C rates specified in this study are based on the mass and theoretical capacity of sulfur (1C = 1675 mA g<sup>-1</sup>). The first discharge capacity is as high as 1367 mAh g<sup>-1</sup>, demonstrating the assistance of the effective carbon interlayer in enhancing the conductivity and active material utilization. The cell with the MCP could be cycled up to 3C while maintaining a capacity above 846 mAh g<sup>-1</sup> for 70 cycles. As exhibited in Figure 6.3(e), the cyclability at 1C rate retains over 1000 mAh g<sup>-1</sup> after 100 cycles, converting a retention rate of 85% with an average Coulombic efficiency of 97.6%. The charge efficiency of the first two cycles is higher than 100% due to the reutilization of the sulfur core in the cathode as the cell is cycled. The reutilization of the inactive core of the active material is generally found in the Li-S system, especially at high C rates during the initial cycles. At a higher rate of 2C for long cycles, the cell with the MCP exhibits 846 mAh g<sup>-1</sup> with an average Coulombic efficiency of > 98% after 150 cycles; it also shows a more considerable capacity increase during the first 40 cycles compared to the cell at 1 C rate.

### 6.3.5 Impact of pore size

We also tested another bimodal micro-/meso- porous carbon paper (micropores: ~ 1.5 nm; mesopores: ~ 6 nm) as an interlayer in lithium-sulfur cells; however, the battery performance was not as good as the one with the microporous carbon interlayer under the same conditions. Active sulfur in the battery first transforms to long-chain Li<sub>2</sub>S<sub>8</sub>, which consists of two Li-S bonds and seven S-S bonds. Both bond types have a bond length of about 2 Å,<sup>163, 164</sup> so the longest chain length estimated among the species of polysulfides (Li<sub>2</sub>S<sub>8</sub>) is around 2 nm. Therefore, much larger pores like mesopores may not trap the migrating polysulfides efficiently during cycling because of the size effect. In contrast, microporous/small-mesoporous materials possess the advantage to absorb polysulfide

intermediates due to the similar dimensions of the pores and polysulfide ions, thereby enhancing the cycling reversibility of Li-S batteries.

#### **6.4 CONCLUSIONS**

In summary, a microporous carbon interlayer has been developed to substantially improve the cycle performance of Li-S batteries. The flexible carbon paper provides fine contact with the cathode surface, offering electron pathways through the insulating sulfur/lithium sulfide and accommodating the migrating polysulfide intermediates. This bi-functional carbon interlayer with micropores/small-mesopores operates not only as an “upper current collector” to enhance the active material utilization but also as a “polysulfide stockroom” to retain the cyclability. Moreover, the cells involve only a novel cell configuration by inserting an interlayer without requiring the formation of sulfur-carbon or sulfur-polymer composites, leading to facile and low-cost manufacturing. This strategy can be extended with other potential lightweight conductive/porous interlayers, offering further improvement in Li-S batteries.

## Chapter 7: Fast, reversible lithium storage with sulfur/long-chain polysulfide redox couple

### 7.1 INTRODUCTION

As the current candidate for application in electric vehicles (EVs) and hybrid EVs, traditional lithium-ion batteries are faced with several challenges meeting the requirements of fast-charging, long cycle life, safety, low cost, and high energy density necessary for long range driving.<sup>6</sup> When charged within a short time (< 30 min), battery systems based on insertion cathodes generally sacrifice capacity, only achieving < 150 mAh g<sup>-1</sup>. To address this issue, various structural modifications, additives, and surface coatings have been explored.<sup>165-169</sup> However, the introduction of these intensive processing steps increases the cost. More recently, lithium-sulfur (Li-S) batteries have drawn attention due to their large theoretical capacity (1675 mAh g<sup>-1</sup>) and the low cost and abundance of sulfur as the cathode material.<sup>6-8, 36</sup> Although around 60 – 75% theoretical capacity and relatively stable cycle performance have been achieved through state-of-the-art electrode designs,<sup>36, 44, 51, 60, 62, 66, 81, 91, 102</sup> reaction reversibility and active material utilization remain unsatisfactory, especially at high current rates. To make Li-S batteries a reliable energy storage option for large-scale, high-rate applications such as EVs, highly reversible electrochemical reactions with short charging time must be achieved.

One of the major issues of Li-S batteries is the slow kinetics of the redox reactions at the lower plateau ( $\text{Li}_2\text{S}_4 \leftrightarrow \text{Li}_2\text{S}$ ).<sup>36</sup> As a result, 100% active material utilization is hardly realized, resulting in the incomplete conversion of end product of  $\text{Li}_2\text{S}$  and poor high-rate battery performance. This can be attributed to the fact that long-chain polysulfides ( $\text{Li}_2\text{S}_x$ ,  $8 \leq x \leq 4$ ) can easily dissolve in the liquid electrolyte and

in turn undergo sluggish phase transformations into the solid-state discharge products of  $\text{Li}_2\text{S}$ .<sup>7, 8, 36</sup> Therefore, the electrochemical reactions between  $\text{Li}_2\text{S}_4$  and  $\text{Li}_2\text{S}$  involve slow nucleation and phase transformation. Our strategy is to fully convert the first step redox reactions ( $\text{S}_8 \leftrightarrow \text{Li}_2\text{S}_4$ ; theoretical capacity =  $419 \text{ mAh g}^{-1}$ ) under controlled voltage conditions while employing a facile interlayer cell configuration. We have developed porous/conductive carbon interlayers between separators and cathodes that are able to significantly improve the cycle performance and rate capability of Li-S battery system.<sup>75, 76</sup> It has been reported that pores with different size in carbon substrates have different functions: micropores are in charge of the storage of active material, but mesopores not only accommodate polysulfide species but also facilitate Li ion transport during electrochemical reactions.<sup>45</sup> With a blended meso-/micro- porous interlayer in Li-S cells, we show that 100% theoretical capacity of the first step redox reactions and high energy density can be obtained even under high current densities, without sacrificing much the battery performance at fast charge/discharge.

## **7.2 EXPERIMENTAL**

### **7.2.1 Synthesis and materials characterizations**

The  $\text{CO}_2$ -activated BMC sample was prepared via self-assembly of a block copolymer and phloroglucinol-formaldehyde resin under acidic conditions as described in a previous report.<sup>170</sup>  $\text{CO}_2$  activation was performed by heating mesoporous carbon particles within a tube furnace under flowing  $\text{CO}_2$  ( $100 \text{ cm}^3 \text{ min}^{-1}$ ) with a heating rate of  $10 \text{ }^\circ\text{C min}^{-1}$  to  $950 \text{ }^\circ\text{C}$  for 2 h. The blended carbon interlayer was prepared by mixing the as-synthesized BMC, as-purchased high-surface-area MC (Black Pearl), and polytetrafluoroethylene (PTFE) binder at a 3:3:4 mass ratio in a mortar with the solvent of isopropyl alcohol. Then the elastic mixture was pressed as a film and cut into circular

disks as the interlayer. The microstructure and elemental analysis of the samples were acquired with a Hitachi S-5500 SEM equipped with EDX and a FEI-Titan FEG – (S) TEM microscopes. The nitrogen adsorption isotherm was measured at -196 °C (77 K) with a Quantachrome NOVA 2000 volumetric adsorption analyzer. The surface area of the samples was calculated by the BET method, and the pore size distribution plot was derived from the desorption branch of the isotherm based on the Barrett-Joyner-Halenda (BJH) model. XPS data were collected at room temperature with a Kratos Analytical spectrometer and monochromatic Al K $\alpha$  (1486.6 eV) X-ray source.

### **7.2.2 Electrochemical characterizations**

The Li-S coin cells (CR2032) were assembled with a conventional sulfur cathode (70 wt. % sulfur as the active material, 20 wt. % carbon black as the conductive agent, and 10 wt. % polyvinylidene fluoride as the binder), the as-prepared blended carbon interlayer, a Celgard separator, a lithium metal anode, and a nickel foam spacer in an Argon-filled glove box. The electrolyte was prepared by dissolving 1.85 M LiCF<sub>3</sub>SO<sub>3</sub> salt and 0.1 M LiNO<sub>3</sub> into a mixed solvent of 1,2-dimethoxyethane (DME) and 1,3-dioxolane (DOL) (1:1, v/v). The mixed solvent without the lithium salt was used as the washing fluid for cycled samples. CV scans were performed with a VoltaLab PGZ 402 Potentiostat in the voltage window of 2.8 – 2.1 V. All of the cycling data were collected with a programmable Arbin battery cycler. The C rate mentioned in the article was based on the mass of sulfur and the theoretical capacity of the S/Li<sub>2</sub>S<sub>4</sub> redox couple (1C = 419 mAh g<sup>-1</sup>).

## **7.3 RESULTS AND DISCUSSION**

### **7.3.1 Morphological analysis**

The morphology of microporous carbon (MC) and bimodal meso-/micro- porous carbon (BMC) particles are compared in Figure 7.1(a) and 7.1(b). MC has a particle size of around 20 – 40 nm, and BMC is in form of large microparticles. In the blended carbon paper, nano-sized MC tends to attach to micron-sized BMC (Figure 7.2), so most surface morphology resembles nanoparticles. Figure 7.1(c) shows a comparison of the MC-covered and uncovered BMC matrix. Abundant surface porosity is formed from the interspaces between the MC-MC and MC-BMC interfaces, which is beneficial for the permeability of the electrolyte. The mesoporosity in BMC can be observed in the high-magnification scanning electron microscope (SEM) and transmission electron microscope (TEM) images in Figure 7.1(d). The as-prepared blended carbon paper with a 1:1 weight ratio of MC and BMC was used as the interlayer configuration in Li-S cells for the following analysis.<sup>75, 76</sup>

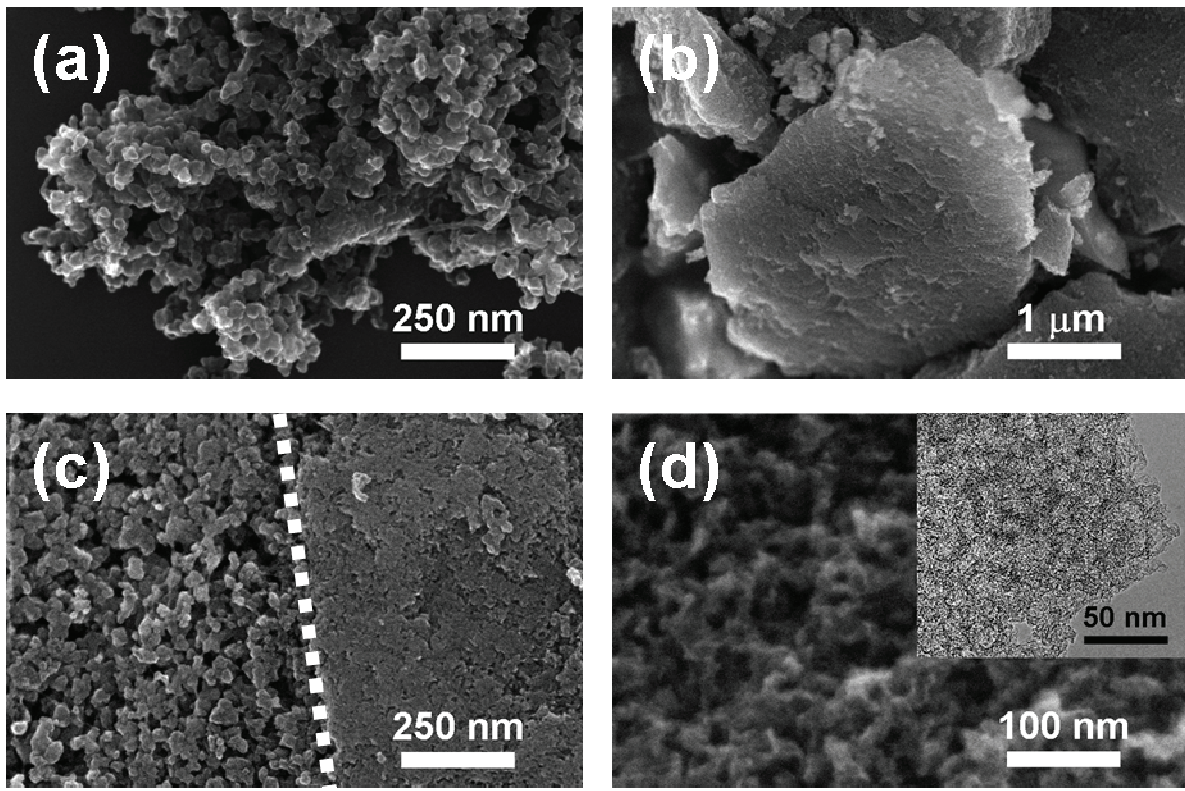


**Figure 7.1.** SEM images of (a) MC, (b) BMC, and (c) interface between MC/BMC of the blended carbon interlayer; (d) high-magnification SEM and TEM (inset) images of BMC.

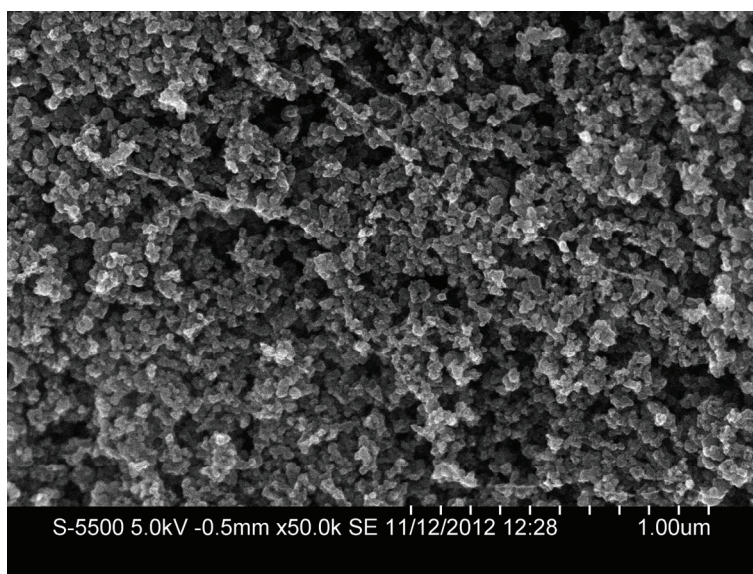


**Figure 7.2.** SEM image of BMC covered by MC particles.

### 7.3.2 Electrochemical analysis

A typical discharge plateau of the Li/blended carbon interlayer/S battery is shown in Figure 7.3. It can be seen that 100% theoretical capacity,  $419 \text{ mAh g}^{-1}$ , is realized in the first discharge plateau; however, the second plateau is far from full utilization, which is due to the slow kinetics of the reduction reactions from long-chain polysulfides to  $\text{Li}_2\text{S}$ . During the second-step redox reactions in Li-S batteries, ionic polysulfides dissolved in the electrolyte have to nucleate and transform into solid-state  $\text{Li}_2\text{S}$ ; predictably, these reactions are very sluggish. In a previous study of high-rate Li-S cells, it was shown that the upper plateau does not change significantly with increasing current densities over  $5 \text{ A g}^{-1}$ , demonstrating that the electrochemical reactions between sulfur and long-chain polysulfides are not highly rate-dependent compared to those of the lower plateau.<sup>59</sup> Accordingly, utilizing only the upper plateau by adjusting the cutoff voltage can be a promising means to create high-rate Li-S batteries.

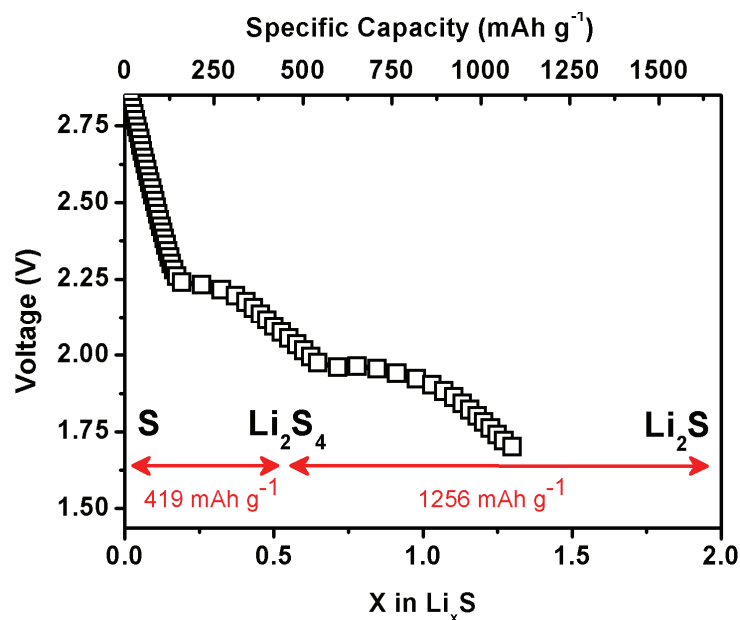


**Figure 7.3.** Initial discharge plateau profile of the Li/blended carbon interlayer/S battery.

Figure 7.4 displays the upper plateau at various C rates ( $1C = 419 \text{ mA g}^{-1}$ ). Although the current rate increases to  $5C$ , complete active material utilization can still be achieved. In addition, an impressive capacity of around  $300 \text{ mAh g}^{-1}$  is obtained under the high rate of  $10C$ , which translates to a charging/discharging time of less than 5 minutes, showing superior rate capability. However, the overpotential behavior becomes quite severe with the increase of C rate to  $20C$ , representing the kinetic limitation of this system. Cyclic voltammetry (CV) diagram with increasing scan rates can be seen in Figure 7.4(b). Typical overpotential is observed in the CV plot showing the up-shift of the anodic peaks and down-shift of the cathodic peaks with increasing rate, and the peak is barely present when the scan rate reaches  $2 \text{ mV s}^{-1}$  (about  $20C$  rate), implying incomplete electrochemical reactions at high scan rates corresponding to the kinetic limitation mentioned above. Figure 7.4(c) shows CV scans for the first 30 cycles at a rate of  $2 \text{ mV s}^{-1}$ , where the cathodic peak is located at around  $2.15 \text{ V}$  and the reversibility is

nearly perfect, demonstrating the excellent reversibility of the sulfur/long-chain polysulfides redox couple in the Li-S battery with the blended carbon interlayer configuration.

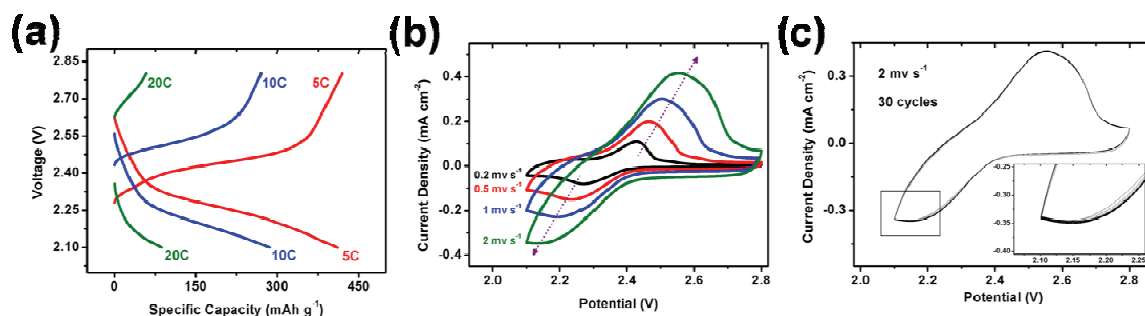


**Figure 7.4.** (a) Discharge/charge plateau profiles with a cutoff voltage of 2.1 V; (b) CV curves under various scan rates; (c) CV plot at a scan rate of 2  $\text{mV s}^{-1}$  for 30 cycles.

Figure 7.5(a) exhibits the rate capability of the Li-S batteries with and without the blended carbon interlayer. The cell performance with the interlayer is significantly improved compared to that without the interlayer. In the traditional Li-S battery, the decline in capacity is noticeable and severe during initial cycling at 1C. The comparison between the cells with and without the interlayer gives explicit evidence that the blended carbon paper plays a key role in lowering the internal cell resistance and stabilizing charge/discharge reactions.<sup>75, 76</sup> Additionally, it is worth mentioning that it is possible for the discharge capacity of the cell with the interlayer configuration to recover to over 350  $\text{mAh g}^{-1}$  at a lower discharge rate of 5C (the 41<sup>st</sup> cycle) immediately after the ultrafast cycling at 20C (the 31<sup>st</sup> to the 40<sup>th</sup> cycle), showing the reliability of this system under variable cycling conditions.

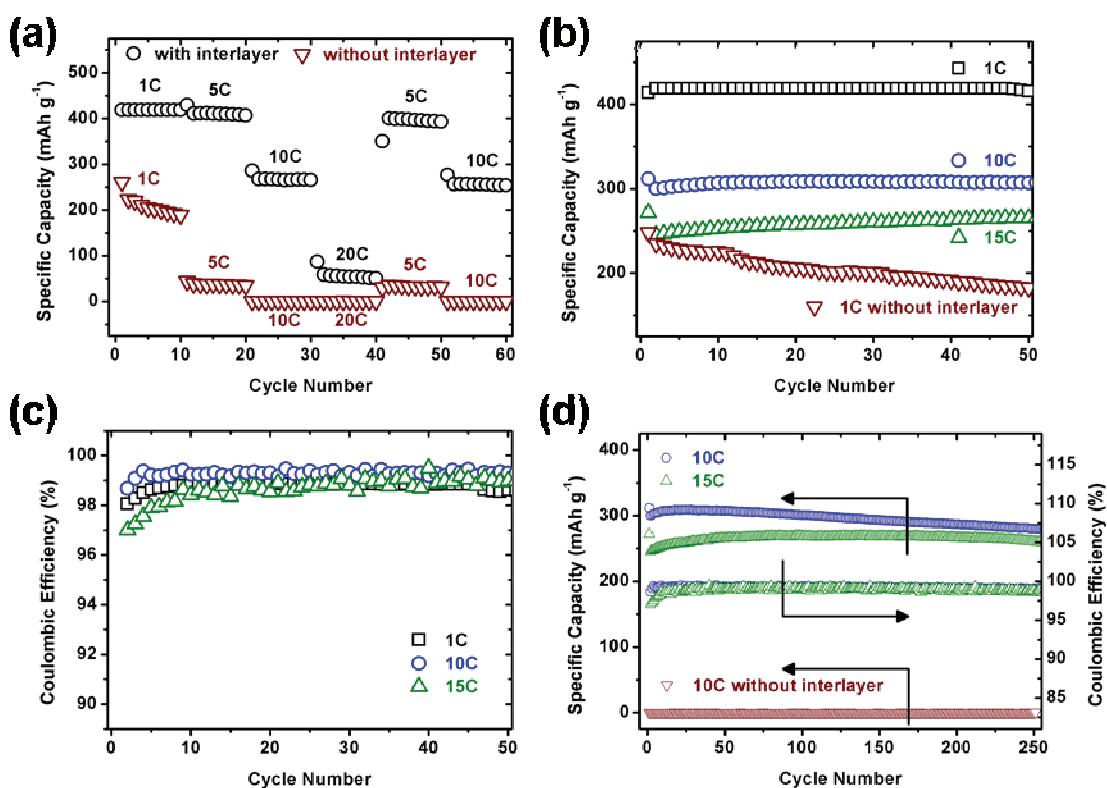


**Figure 7.5.** (a) Rate capability of the Li-S cells with and without the interlayer; (b) cyclability and (c) Coulombic efficiency of cells at different C rates; and (d) prolonged cycle performance at 10C and 15C rates.

The initial discharge/charge plateau profiles of the Li-S cells with and without the blended interlayer can be seen in Figure 7.6. Full capacity of  $419 \text{ mAh g}^{-1}$  can be obtained after the insertion of the interlayer; in contrast, the traditional cell only offers  $\sim 59\%$  sulfur utilization. Moreover, the overpotential of the modified cell is also reduced, avoiding unnecessary energy loss. Figure 7.5(b) and 7.5(c) show, respectively, the cyclability and Coulombic efficiency of the cells under different current densities for 50 cycles. The cells with the interlayer cycled at 1C, 10C and 15C show not only a high and stable capacity, but also Coulombic efficiencies after 50 cycles as high as  $98.7\% - 99.2\%$ . On the contrary, the traditional Li-S battery shows only passable first discharge

capacity, which continues to decline upon further cycling. Furthermore, capacity retention over prolonged cycling with high C rates is achieved (Figure 7.5(d)). After 250 cycles, 280 mAh g<sup>-1</sup> and 260 mAh g<sup>-1</sup> are still realized, respectively, at 10C and 15C, representing 90% and 96% capacity retention. All in all, this Li/blended carbon interlayer/S system is able to accomplish the fast and highly reversible electrochemical reactions of sulfur/long-chain polysulfides redox couple for many cycles.

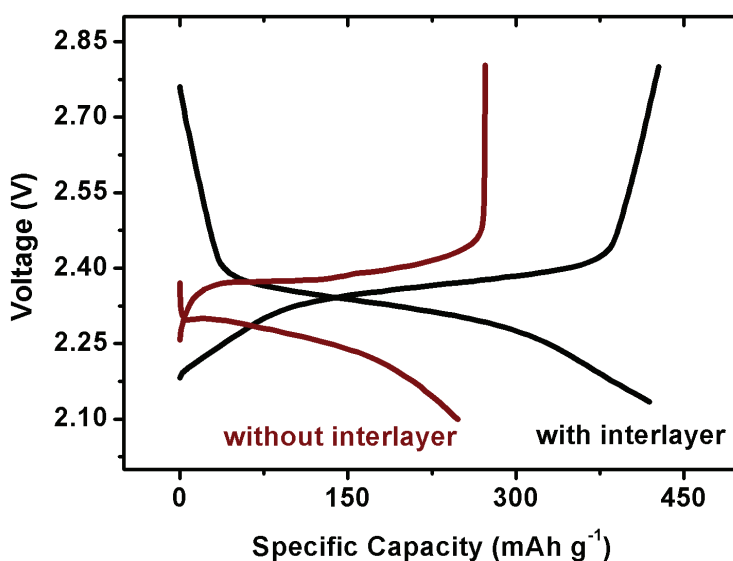


**Figure 7.6.** Initial discharge/charge profiles of the Li-S cells with and without the blended carbon interlayer.

### 7.3.3 Surface area and pore size distribution

To understand the function of the meso-/micro- porous carbon interlayer in the battery, the surface area, total pore volume, and pore size distribution of the interlayer were measured before and after cycling. As shown in Figure 7.7(a), MC (Black Pearl) presents mixed type I and type II isotherms with a Brunauer-Emmett-Teller (BET) surface area of 1095 m<sup>2</sup> g<sup>-1</sup> and a total pore volume of 2.48 cm<sup>3</sup> g<sup>-1</sup>. In contrast, BMC shows a type IV isotherm with a larger BET surface area of 1741 m<sup>2</sup> g<sup>-1</sup> and a total pore

volume of  $1.66 \text{ cm}^3 \text{ g}^{-1}$ . The blended carbon interlayer has a hybrid-shaped isotherm with a surface area of  $819 \text{ m}^2 \text{ g}^{-1}$ . The measured surface area of the interlayer is very close to the calculated value from the weight percentage of carbons (30% MC + 30% BMC). Figure 7.8 represents the pore size distribution of MC, BMC, and the blended carbon interlayer. The blended carbon interlayer shows both mesoporous and microporous characteristics, as imparted by the two raw carbon materials. After 250 cycles, the interlayer loses about 85% of the initial surface area and pore volume, which is due to the migrating long-chain polysulfides filling the pores during cycling. Washed and unwashed interlayer samples were also investigated after cycling, as shown in Figure 7.7(b). A small fraction of pores with diameters of 1.4 and 5.6 nm were detected in the washed sample, likely due to a trace amount (less than  $0.05 \text{ cm}^3 \text{ g}^{-1}$ ) of lithium salts recrystallized from the electrolyte and some unstable polysulfide species. This indicates that the majority of the soluble active material is effectively-captured by the pores in the blended carbon interlayer during cycling.

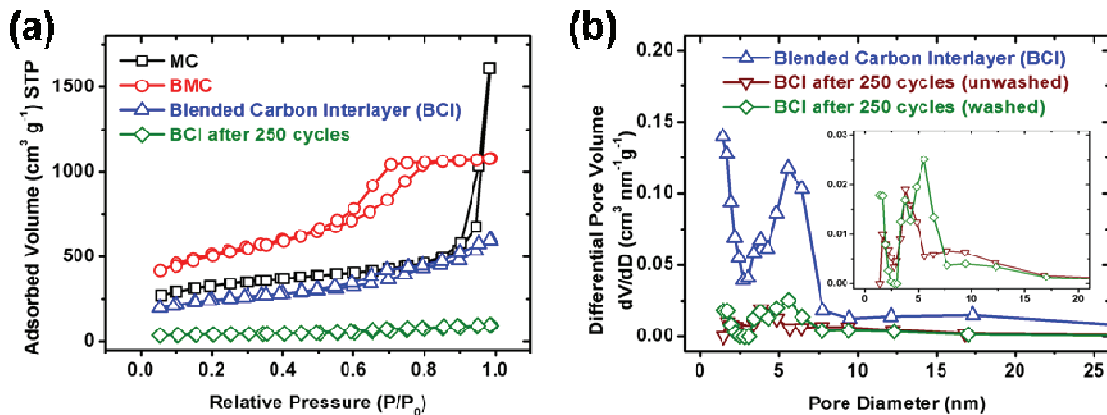


**Figure 7.7.** (a) Isotherms of MC, BMC, and the blended carbon interlayer before and after cycling; (b) pore size distributions of the blended carbon interlayer before and after cycling.

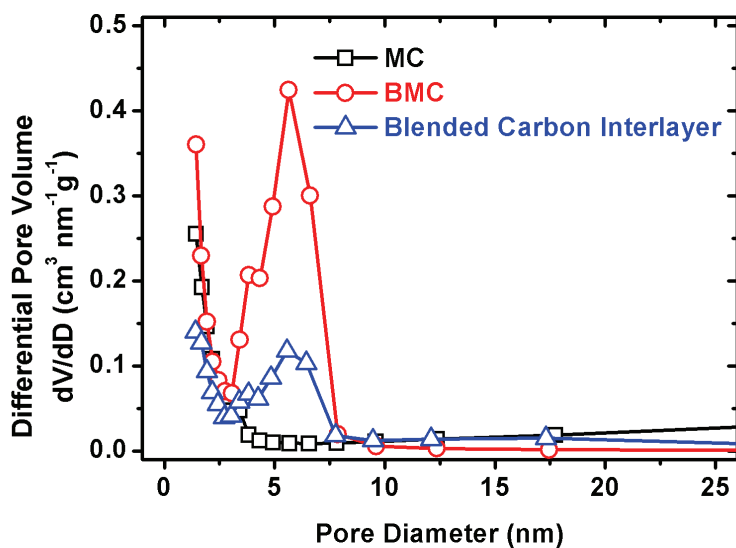


**Figure 7.8.** Pore size distribution curves of MC, BMC, and the blended carbon interlayer.

### 7.3.4 Morphological change; elemental and surface analysis

In order to further study the trapped species in the blended carbon interlayer during cycling, *ex situ* SEM and energy-dispersive X-ray (EDX) spectroscopy analyses were carried out. The interlayer sample in the discharge and charge states can be seen, in Figure 7.9(a) and 7.9(b), respectively. It is clear that the interlayer exhibits well-preserved surface porosity constructed between C-C interfaces, offering abundant electrolyte channels for electrode-electrolyte contact during cycling. Independent particles can be clearly observed in both samples, verifying that formation of thick solid films did not take place on the surface, which usually occurs in traditional Li-S systems and impedes lithium-ion transport.<sup>27, 32</sup> The peaks from elemental fluoride seen in Figure 7.9(c) and 7.9(d) originate from the binder in the interlayer. Both spectra show that active sulfur species were captured in the interlayer, and the sulfur peak of the sample after the discharge to 2.1 V is smaller than that of the charged sample due to the active material loss during SEM processing in the vacuum chamber.<sup>13</sup>

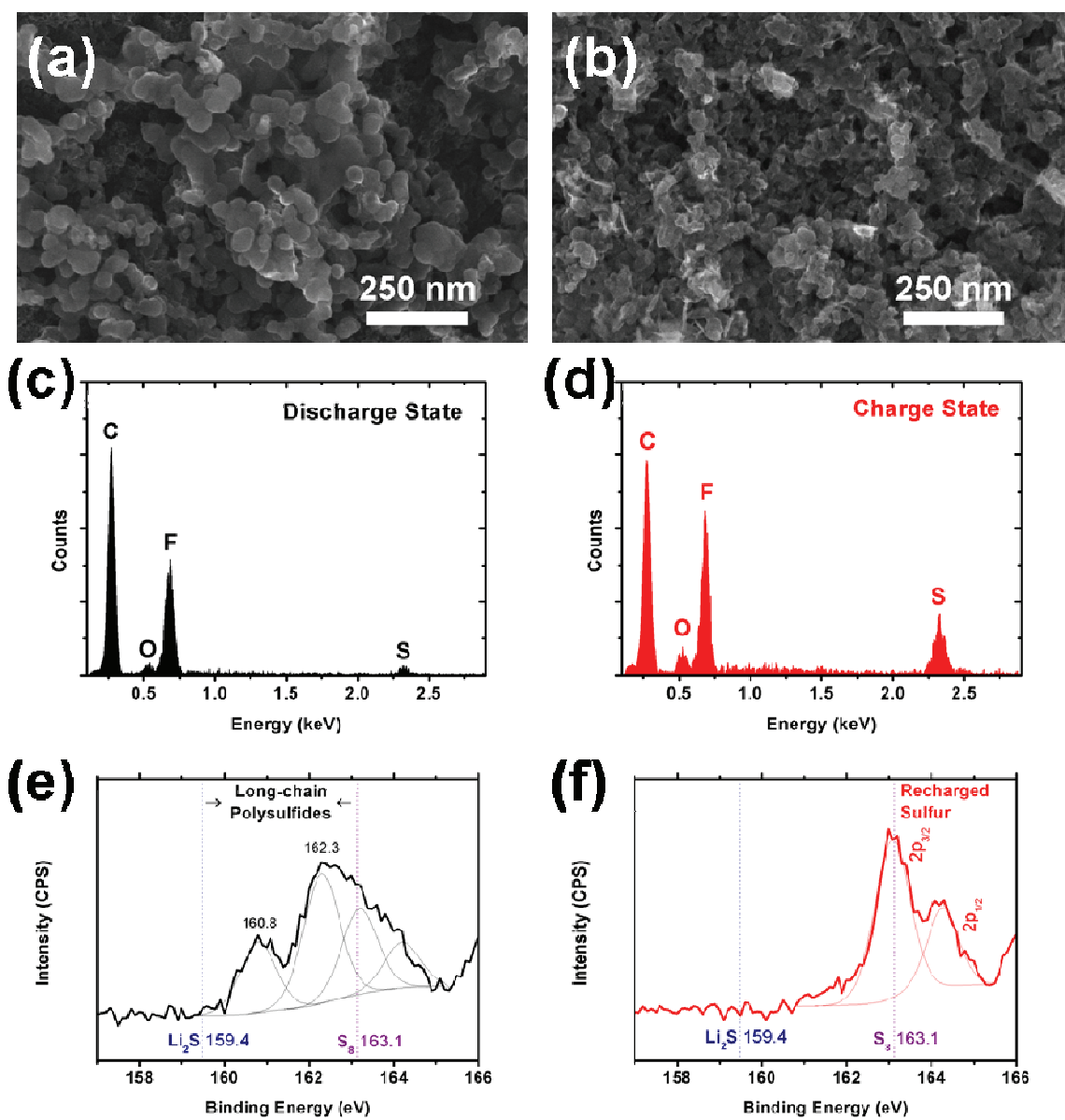


**Figure 7.9.** *Ex situ* SEM images of (a) the interlayer in discharged state and (b) the interlayer in charged state; EDX spectra of (c) the interlayer in discharged state and (d) the interlayer in charged state; XPS spectra of (e) the interlayer after discharging and (f) the interlayer after charging.

It is difficult to determine the type of sulfur species from the elemental signals in the EDX spectra, so X-ray photoelectron spectroscopy (XPS) measurements were conducted for pure sulfur, pure lithium sulfide, and the interlayer after discharging and

charging. XPS analysis has been used to determine the species of active material in the fully discharged or charged states in Li-S batteries before,<sup>91</sup> but has not been demonstrated for intermediate polysulfides. The wide-scan surveys of the cycled interlayer in Figure 7.10 display different characteristic peaks such as lithium, sulfur, carbon, oxygen and fluoride. The lithium peak comes from the precipitation of lithium salt in the electrolyte. Sulfur signals belong to active sulfur compounds trapped in the blended carbon interlayer and  $\text{LiCF}_3\text{SO}_3$  salt, and carbon peaks can be attributed to the carbon particles and binder in the interlayer. Fluoride mainly comes from the binder, as discussed previously with the EDX results. The XPS spectra of pure sulfur and lithium sulfide were used as references to determine the trapped sulfur/polysulfide compounds (Figure 7.11). Pure sulfur and lithium sulfide in the S 2p region both have two split peaks. One is from  $2p_{3/2}$  orbital, and the other is from  $2p_{1/2}$  orbital, which has a half intensity with a higher binding energy.<sup>171</sup> The strongest  $2p_{3/2}$  peaks for sulfur and lithium sulfide are located at, respectively, 163.1 eV and 159.4 eV. If there are any species of long-chain polysulfides produced during cycling, additional peaks should be observed between 159.4 eV and 163.1 eV.

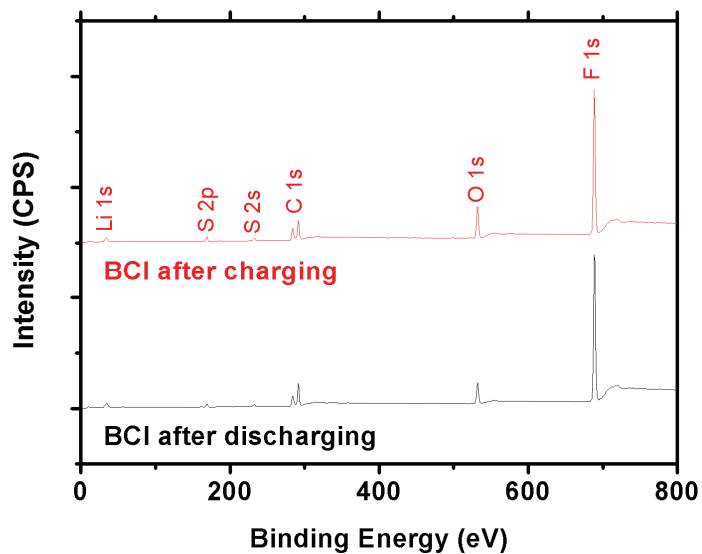


**Figure 7.10.** XPS spectra of the blended carbon interlayer (BCI) after discharging and charging.

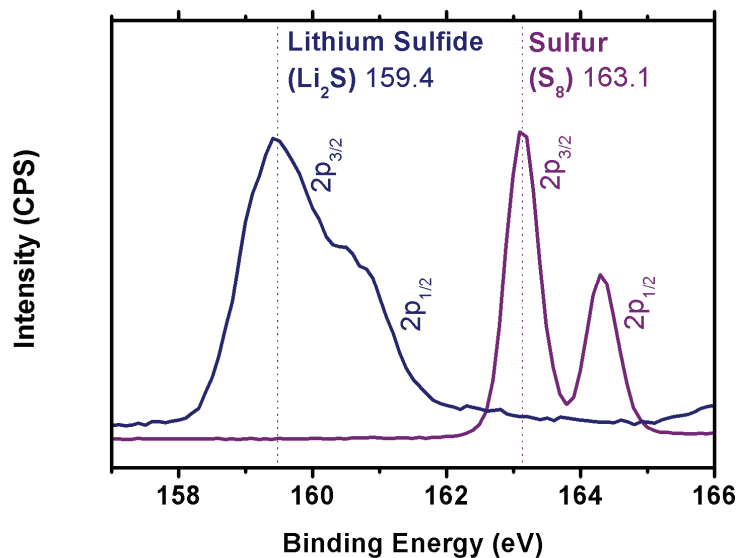


**Figure 7.11.** XPS spectra of pure sulfur and lithium sulfide.

Figure 7.9(e) and 7.9(f) represents the detailed XPS scans of the blended carbon interlayer in different stages during cycling. After discharging at 10C for 250 cycles, at

least four distinct sulfur 2p peaks can be identified in the spectra (Figure 7.9(e)). The two additional XPS peaks at 160.8 eV and 162.3 eV were neither from sulfur nor from lithium sulfide, implying that long-chain polysulfide compounds were formed at the end of the discharge process at 2.1 V. A pair of peaks near the pure sulfur signal was also detected, possibly due to the unutilized active material leftover after discharging at a high current density. In contrast, the XPS spectra of the interlayer after charging shows only the characteristic peaks of pure sulfur, representing the complete charge reaction for the Li-S cell.

#### 7.4 CONCLUSIONS

In conclusion, full capacity can be realized in the first-step electrochemical reactions at rates as high as 5C by inserting a blended carbon interlayer in the Li-S cells. Even when the current rate rises to 10C and 15C, the Li-S battery retains excellent cycle stability and high discharge capacity over 250 cycles. Thus, the kinetics of the sulfur/long-chain polysulfide redox couple ( $S_8 \leftrightarrow Li_2S_4$ ) is experimentally proven to be very fast in the Li-S system. The meso-/micro- pores in the interlayer are responsible for storing the migrating polysulfides and offering sufficient electrolyte accessibility. As a result, fast and highly reversible cathode reactions could be obtained in Li-S batteries by coupling a blended porous carbon interlayer and a low-cost conventional sulfur cathode with a controlled voltage window. This cell design offers full utilization of the sulfur/long-chain polysulfides redox couple, and is a promising strategy for high power applications.

## Chapter 8: A strategic approach to recharge Li-S batteries for long cycle life

### 8.1 INTRODUCTION

To satisfy the demand for efficient energy storage employed in electric vehicles (EVs), smart energy grids, and renewable energies, development of next-generation battery systems is an inevitable task for researchers and scientists. Lithium-ion (Li-ion) batteries have been widely applied in consumer electronics successfully for over two decades, and are being developed for other purposes such as EVs, aerospace devices, and military applications. Research into high-energy-density battery systems including Li-S and Li-air batteries is critical for the development of the next-generation of thinner, lighter, and lower cost battery systems.<sup>6</sup>

Following the cell design of commercialized Li-ion batteries, Li-S cells with solid-state sulfur cathodes are expected to receive fewer challenges than Li-air batteries with gaseous cathodes.<sup>6,8</sup> As the insulating issue of sulfur/lithium sulfide ( $\text{Li}_2\text{S}$ ) can be solved by the incorporation of conductive carbon materials, the main obstacle that remains in the Li-S battery is the dissolution of polysulfide intermediates produced during electrochemical reactions.<sup>7, 8, 21</sup> Much work has been reported to address this problem by trapping dissolved active materials in the cathode matrix; however, capacity fade is still observed even after these diverse approaches. As seen in Table 8.1, many advanced Li-S battery systems have been designed and have shown remarkable progress.<sup>39, 44, 50, 51, 62, 98, 104, 131, 172</sup> For example, high capacities of  $> 1000 \text{ mAh g}^{-1}$  (based on sulfur weight) during initial cycles and longer cycle life ( $> 100$  cycles) have been demonstrated. Nevertheless, in most cases, the discharge capacity tends to gradually decay with increasing cycle number and time. To gear the Li-S battery research toward

practical applications, other approaches should be adopted to integrate with the currently developed electrodes/systems.

Approach	First Discharge Capacity (mAh g <sup>-1</sup> )	Reversible Discharge Capacity (mAh g <sup>-1</sup> )	Current Rate (mA g <sup>-1</sup> )	Total Cycle Number	Degradation Rate per Cycle	Sulfur Loading in Electrode	Ref.
S-TiO <sub>2</sub> yolk-shell nanocomposite	1030	690	836.5 (C/2)	1000	0.033%	53 wt. % 0.4 – 0.6 mg cm <sup>-2</sup>	5
Solvent-in-salt electrolyte	1041	770	335 (C/5)	100	0.26%	48 wt. %	6
Spherical ordered mesoporous C-S nanocomposite	1070	700	1675 (1C)	100	0.35%	57 wt. %	7
Double-shelled hollow C-S sphere composite	1020	690	167.5 (C/10)	100	0.32%	45 wt. %	8
Porous hollow C-S composite	1071	974	836 (C/2)	100	0.09%	65 wt. %	9
Hollow CNF-encapsulated S cathode	~1400	730	836.5 (C/2)	150	0.48%	~1.0 mg cm <sup>-2</sup>	10
Amphiphilic surface modified hollow CNF-S composite	828	~660	836.5 (C/2)	300	0.07%	~1.0 mg cm <sup>-2</sup>	11
Ultrasound assisted S-C cathode with fluorinated ether	1195	836	230	100	0.30%	29 wt. %	12
Smaller S molecules in a microporous C/CNT matrix	1670	1142	167.5 (C/10)	200	0.16%	32 wt. %	13

**Table 8.1.** Summary of the performance of advanced Li-S battery systems.

Constraining the charge capacity or voltage window of lithium-ion batteries has been widely applied for stabilizing the cathode reactions for years. For instance, LiCoO<sub>2</sub> cathodes cannot be charged to more than 50% of their theoretical capacity (140 mAh g<sup>-1</sup>); otherwise oxygen loss from the lattice will occur and lead to chemical and structural instabilities.<sup>173</sup> In industry, safe operating charge/discharge voltages are defined

according to the stable electrochemical reaction region in the battery system to avoid overcharge/overdischarge, which might cause electrode and electrolyte decomposition. The Li-S battery is usually operated between 2.8 V and 1.5 V. If  $\text{LiNO}_3$  is added in the electrolyte for improving the Coulombic efficiency, the terminal discharge potential should be raised to over 1.7 V to prevent the irreversible reduction of  $\text{LiNO}_3$ .<sup>21, 130</sup>

Herein, we develop a simple recharge technique that can significantly enhance the cycle life of Li-S cells under long-term and repeated cycling conditions. By recharging the cell within the lower plateau ( $\text{Li}_2\text{S} \leftrightarrow \text{Li}_2\text{S}_4$ ; theoretical capacity:  $1256 \text{ mAh g}^{-1}$ , see Figure 8.1(a)), the battery performance can be improved considerably with a fade-free cyclability. The upper plateau involves oxidation-reduction reactions between soluble long-chain polysulfides and sulfur ( $\text{Li}_2\text{S}_4 \leftrightarrow \text{S}$ ; theoretical capacity:  $419 \text{ mAh g}^{-1}$ ), where the well-known shuttle effect occurs significantly, especially during charging.<sup>21, 26, 29</sup> Although the kinetic of these redox reactions are very fast,<sup>123</sup> obvious capacity fading is still found with prolonged cycles or during slow charging/discharging, even with state-of-the-art electrode designs. The reason is that when the charge/discharge processes cover the unstable dissolution region (the upper plateau), a small fraction of the active material migrates out of the electrode during every cycle and it may not be utilized again. Moreover, the highly reactive polysulfide anions could react with the electrolyte solvent, resulting in a depletion of the electrolyte,<sup>21</sup> thereby gradual capacity degradation is seen. Our approach exhibited in Figure 8.1(b) is to confine the electrochemical reactions to the solid-state region (the lower plateau) between  $\text{Li}_2\text{S}$  and  $\text{Li}_2\text{S}_4$ , and therefore, the outward diffusion of soluble long-chain polysulfides from the cathode is negligible, leading to highly stable capacity output for hundreds of cycles.

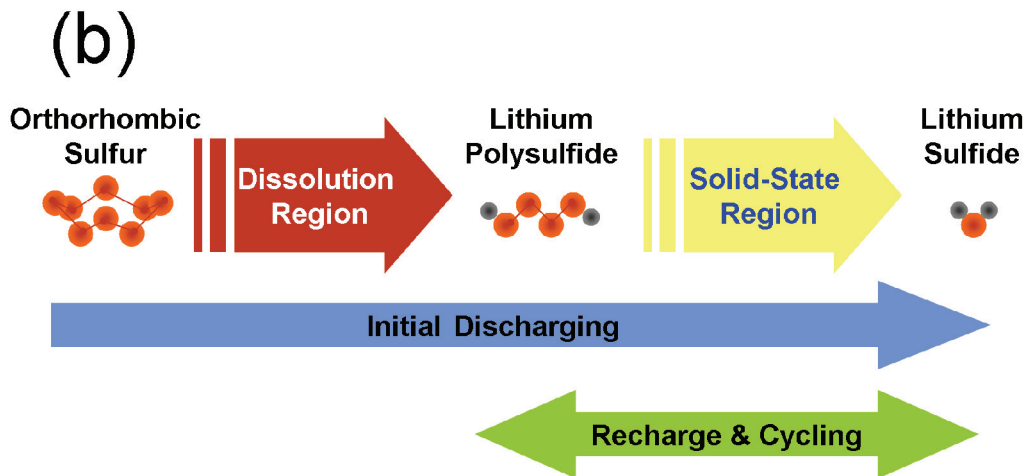
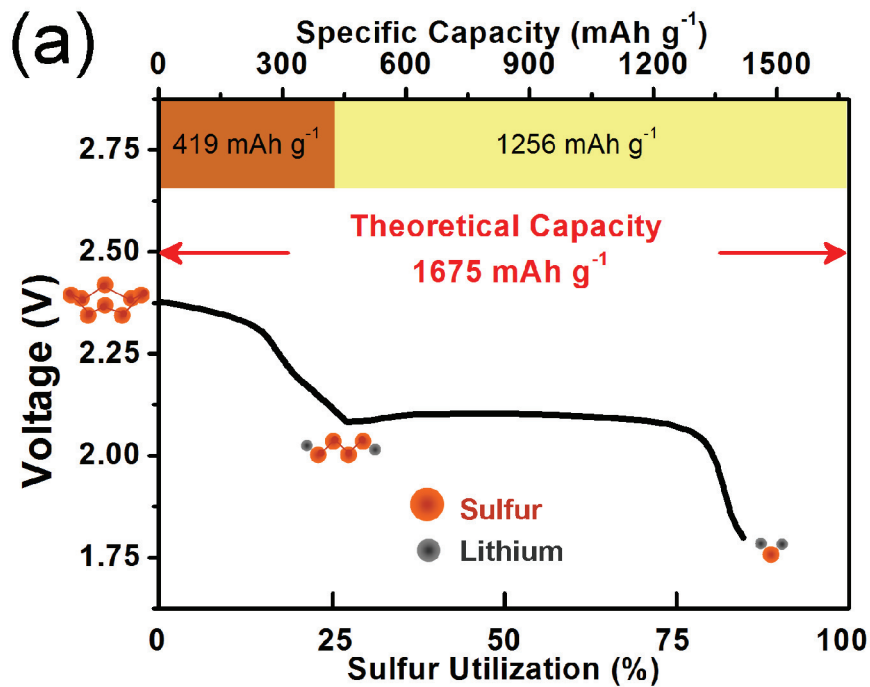


**Figure 8.1.** (a) Typical discharge profile of the Li-S battery showing an upper plateau and a lower plateau with a total theoretical capacity of  $1675 \text{ mAh g}^{-1}$ . (b) The strategic approach to recharge Li-S batteries: A full initial discharge followed by recharging and cycling within the solid-state region (the lower plateau). The lower plateau possesses a theoretical capacity of  $1256 \text{ mAh g}^{-1}$ .

## 8.2 EXPERIMENTAL

### 8.2.1 Preparation of Li-S cells with microporous interlayers

Cathode slurry was prepared by mixing 70 wt.% pristine sulfur, 20 wt.% conductive carbon black (Super P), and 10 wt.% polyvinylidene fluoride (PVDF, Kureha) polymer binder with N-methylpyrrolidinone (NMP, Sigma-Aldrich) as a mixing medium overnight. The sulfur-contained slurry was coated onto an aluminum current collector sheet by the tape casting method and then dried for 24 h at 50 °C in air, followed by roll-pressing and cutting into circular disks. The sulfur loading in the cathode disk is around 1.5 – 1.7 mg cm<sup>-2</sup>. The microporous interlayers were fabricated by mixing commercial high-surface-area carbon black with abundant micropores (Black Pearls 2000, CABOT) and polytetrafluoroethylene (PTFE) polymer binder at a 60:40 weight ratio. These materials were mixed in a mortar with a small amount of isopropyl alcohol as a mixing medium, followed by roll-pressing and cutting into circular disks. Both the cathode disks and microporous interlayers were dried in a vacuum oven for an hour at 50 °C before cell assembly. Blank electrolyte was prepared by dissolving the appropriate amount of lithium trifluoromethanesulfonate (LiCF<sub>3</sub>SO<sub>3</sub>, 98%, Acros Organics) and lithium nitrate (LiNO<sub>3</sub>, 99+%, Acros Organics) in a 1,2-dimethoxyethane (DME, 99+%, Acros Organics) and 1,3-dioxolane (DOL, 99.5%, Acros Organics) (1:1 v/v) mixture to render a 1.85 M LiCF<sub>3</sub>SO<sub>3</sub> and 0.1 M LiNO<sub>3</sub> solution. LiNO<sub>3</sub>-free electrolyte was prepared by using 1.85 M LiCF<sub>3</sub>SO<sub>3</sub> as the only lithium source in the electrolyte. The CR2032 coin cells were assembled in the sequence of sulfur cathodes, prepared electrolyte, microporous interlayers, polypropylene separators (Celgard 2400), and lithium metal anodes (Aldrich) in an Argon-filled glove box. Finally, the cell was crimped and took out of the glove box for electrochemical evaluation.

### 8.2.2 Preparation of Li/dissolved polysulfide cells

The process of fabricating the self-weaving carbon nanofiber (CNF) mat is similar to our previous approach. Commercial CNFs with curly structure (150 mg, Sigma Aldrich) were dispersed in 750 mL of de-ionized water by high-power ultrasonication for 15 minutes with the addition of 20 mL of isopropyl alcohol to wet the CNFs. The products were collected by vacuum filtration and washed with de-ionized water, ethanol, and acetone for several times. The free-standing CNF paper thus formed was a flexible film after drying for 24 h at 100 °C in air, which can be easily peeled off the filter membrane. The blank electrolyte used in the Li/dissolved polysulfide system was with 1 M  $\text{LiCF}_3\text{SO}_3$  salt instead of 1.85 M employed with the interlayer configuration. To prepare the dissolved polysulfide catholyte, sublimed sulfur powder (99.5%, Acros Organics) and an appropriate amount of lithium sulfide ( $\text{Li}_2\text{S}$ , 99.9%, Acros Organics) were added to the appropriate amount of blank electrolyte to render 1.5 M sulfur in the form of  $\text{Li}_2\text{S}_6$  in the solution. The mixture solution was heated at 45 °C in an Ar-filled glove box for 18 h to produce a dark yellow solution with moderate viscosity. Li/dissolved polysulfide in CR2032 coin cells were assembled in an Ar-filled glove box. First, 40  $\mu\text{L}$  of polysulfide catholyte was added into the CNF paper electrode, corresponding to 1.9 mg ( $1.7 \text{ mg cm}^{-2}$ ) of sulfur. Then a Celgard separator was placed on the top of the CNF electrode. A volume of 20  $\mu\text{L}$  of blank electrolyte was added onto the separator, followed by the lithium metal anode. Finally, the cell was crimped and took out of the glove box for electrochemical evaluation.

### 8.2.3 Battery test

The discharge/charge profiles and cyclability data were obtained with a programmable battery cycler (Arbin Instruments). The C rates specified in this study are based on the mass and theoretical capacity of sulfur ( $1675 \text{ mA g}^{-1}$ ). The batteries after

cell assembly were rested for an hour before the cycling test. In a regular charge setting, the cell was discharged/charged in the voltage window of 2.8 V – 1.7 V. In a modified charge setting, all of the cells were fully discharged during the initial cycle, followed by being recharged until reaching a certain value of charge capacity based upon the experimental designs. The cells for XPS measurements were fully cycled for several times, and discharged until reaching specific DoD and then stopped by the cycler program.

#### **8.2.4 Air-sensitive XPS analysis**

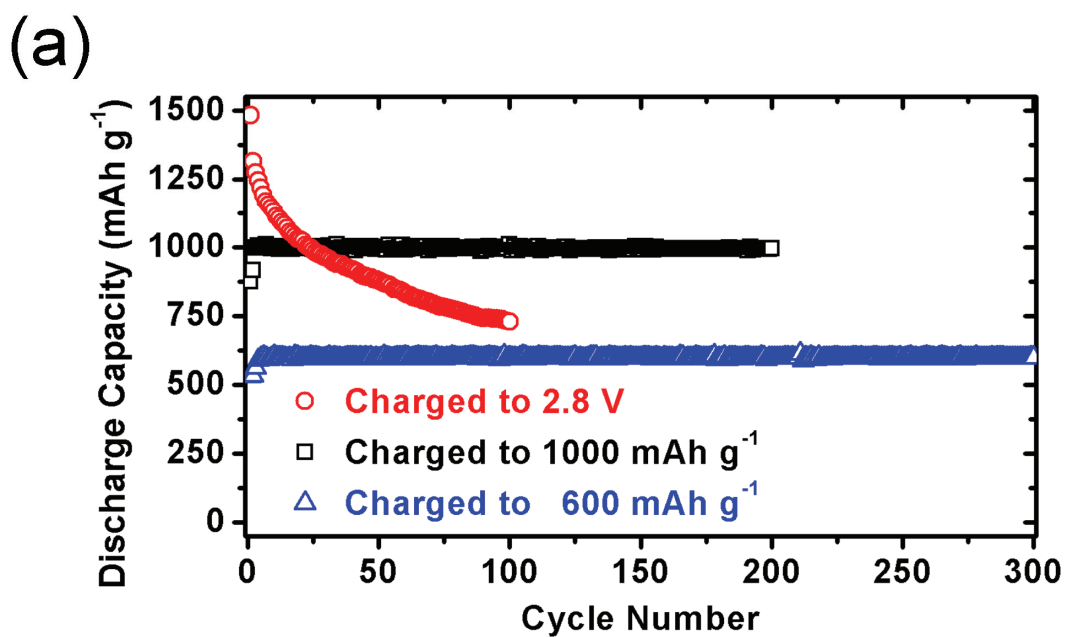
The samples were examined by XPS with a Kratos Axis Ultra spectrometer (Kratos Analytical) utilizing a monochromated Al K $\alpha$  X-ray source ( $h\nu = 1486.5$  eV) and a 45° take-off angle. The pressure in the analysis chamber was typically  $2 \times 10^{-9}$  torr during data acquisition. The microporous interlayer proved to be an efficient polysulfide trap in the Li-S cell, so it was used to analyze the polysulfide intermediates at different DoD. The interlayers were extracted from coin cells within an argon-filled glove box with the H<sub>2</sub>O and O<sub>2</sub> concentrations of < 0.1 ppm and transferred to the spectrometer right away via a custom interface (built at the Surface Analysis Laboratory of the Texas Materials Institute at the University of Texas at Austin) to avoid hydrolysis of Li<sub>2</sub>S and lithium polysulfides. Details of the design of the interface will be published elsewhere. All spectra were fitted with Gaussian-Lorentzian (30% Gaussian) functions and a Shirley-type background by the deconvolution software (CasaXPS, Casa Software). Three constraints on the component peaks were applied: the position (1.18 eV between S 2p<sub>3/2</sub> and S 2p<sub>1/2</sub>), the peak area ratio (S 2p<sub>3/2</sub> : S 2p<sub>1/2</sub> = 2 : 1), and equal full width at half maximum. All reported binding energy values are calibrated to the graphitic C 1s peak

with a value of 284.5 eV and the peak of sulfate signal from the  $\text{LiCF}_3\text{SO}_3$  residue with a value of 169.7 eV.

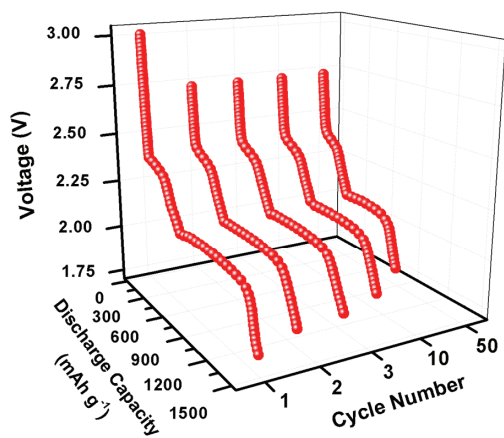
## 8.3 RESULTS AND DISCUSSION

### 8.3.1 Battery performance with extended cycles

The cycle performance comparison between the cells with the regular recharge setting (charging to 2.8 V) and modified recharge setting (charging until reaching 600  $\text{mAh g}^{-1}$  or 1000  $\text{mAh g}^{-1}$ ) is shown in Figure 8.2(a). Stable electrochemical reactions can be accomplished as long as the charge capacity is controlled within the lower plateau region (Figure 8.3). These cells were assembled with a microporous carbon interlayer configuration, which can significantly enhance the active material utilization and cyclability at high rates.<sup>76</sup> However, we found that when the Li-S batteries with interlayers were cycled under a lower C rate, capacity fading behavior can be observed during long-term cycling. The first discharge capacity of the cell under the regular recharge condition is as high as 1483  $\text{mAh g}^{-1}$  at C/5 rate (335  $\text{mA g}^{-1}$ ), but it declines to less than 1000  $\text{mAh g}^{-1}$  before the 100<sup>th</sup> cycle. In contrast, the cells under the modified recharge condition outputs stably the discharge capacity with almost exactly the same value up to 300 cycles. The capacity degradation rates of the cells charged until reaching 600  $\text{mAh g}^{-1}$  and 1000  $\text{mAh g}^{-1}$  are, respectively, only 0.0023% and 0.0027% per cycle, which are an order of magnitude lower than the best record reported by Seh *et al.*<sup>104</sup> This evidence further confirms that the upper plateau reactions are the main causes of the performance deterioration in the Li-S cell system. Accordingly, a simple recharge modification can play a critical role in the stabilization of electrochemical reactions for the sulfur cathode in the Li-S battery.



(b)



(c)

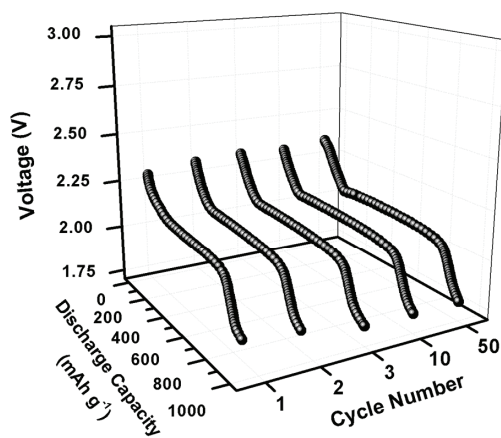


**Figure 8.2.** (a) Cycle performance of the Li-S cells with the regular recharge setting (charged to 2.8 V) and the modified recharge setting (charged to 1000 or 600  $\text{mAh g}^{-1}$ ) at C/5 rate. (b) Discharge curves of the Li-S cells with the regular recharge setting at various cycles. (c) Discharge curves of the Li-S cells with the modified recharge setting (charged to 1000  $\text{mAh g}^{-1}$ ) at various cycles.

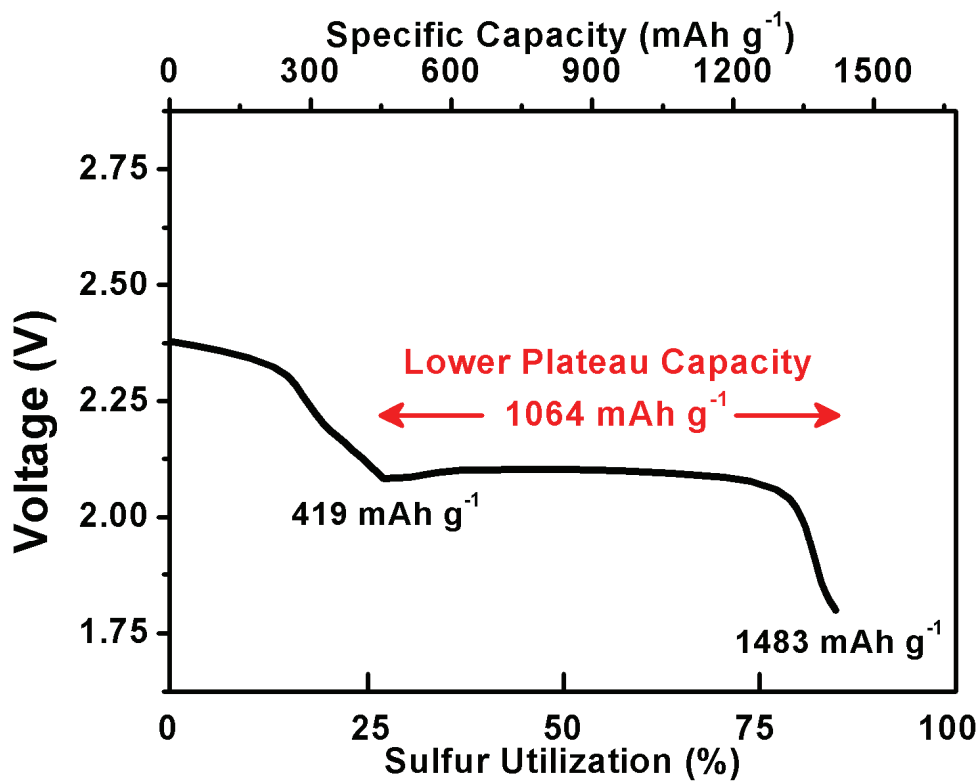


**Figure 8.3.** The initial discharge curve of the Li-S cell with the microporous carbon interlayer at C/5 rate. The lower plateau capacity is 1064 mAh/g<sup>-1</sup>, which is about 85% of the theoretical capacity.

Figure 8.2(b) displays the discharge profiles of the cell with the regular recharge setting. As seen, the upper plateau keeps shrinking with increasing cycle number, implying that the utilizable active material gradually decreases. In fact, the length of the lower plateau is also shortened as cycling proceeds due to the loss of soluble polysulfides. To ensure the lithium-ion transport between the electrolyte and the cathode region, the electrode should possess adequate channels for lithium ions to pass through; otherwise, the electrochemical reactions will terminate due to insufficient ion supply followed by lack of electron exchange. Therefore, the long-chain polysulfides formed in

the dissolution region might still migrate out of the cathode slowly and cannot be recaptured by the porous structure in the following cycles. While charging the cell within the solid-state region, the concern of active material loss from polysulfide dissolution is eliminated. In Figure 8.2(c), the discharge profiles of the cell recharged to  $1000 \text{ mAh g}^{-1}$  possess only the 2 V plateau. This affirms that the redox reactions can be preferentially selected by controlling the charging parameters. All of the lower plateaus at various cycles perform well with the discharge capacity close to  $1000 \text{ mAh g}^{-1}$ , representing an extraordinarily stable electrochemical reaction under this recharge operation.

### 8.3.2 *Ex situ* XPS analysis of polysulfides

To further understand the impact of different polysulfide formations on battery performance, *ex situ* XPS analysis of the interlayer samples retrieved from cycled cells was carried out without exposing the samples to air by employing an air-sensitive sample transfer chamber. Earlier reports have constructed a complete redox reaction mechanism of Li-S batteries via impedance analysis,<sup>11</sup> *in situ* X-ray diffraction (XRD),<sup>13, 174</sup> *ex situ* scanning electron microscopy (SEM),<sup>11, 27, 174</sup> UV-visible absorption spectroscopy,<sup>175</sup> and liquid chromatography (LC).<sup>175, 176</sup> Various XPS analyses have been carried out to investigate the Li electrode surface,<sup>34, 177</sup> but in-depth XPS measurements have not been conducted for detecting specific polysulfides separately so far. In order to avoid the side reactions between polysulfides and electrolyte during cell resting, a higher C rate of C/2 was used as the discharge rate for the XPS samples to assure the polysulfide intermediates are majorly produced from electrochemical reactions. Pristine sulfur and  $\text{Li}_2\text{S}$  powder, which have the binding energy of, respectively, 163.7 eV and 159.8 eV were measured beforehand as the references (Figure 8.4). Figure 8.5 displays a series of XPS results at different depths of discharge (DoD, Figure 8.5(a)). Near the end of the

upper plateau (DoD = 16%, Figure 8.5(b)), two lithium polysulfide peaks were detected. At the beginning of the lower plateau (DoD = 34%, Figure 8.5(c)), not only the previous two polysulfide peaks are observed, but also a small pure  $\text{Li}_2\text{S}$  peak is recognized. This finding is quite distinct from the mainstream electrochemical redox mechanisms that claim  $\text{Li}_2\text{S}_2$  is formed before the end product  $\text{Li}_2\text{S}$ . However, the XPS data show that  $\text{Li}_2\text{S}$ , with the same binding energy as the pristine  $\text{Li}_2\text{S}$  powder, is generated immediately after the start of the lower plateau, and this will be discussed in the following paragraph. At the middle of the lower plateau (DoD = 74%, Figure 8.5(d)), three XPS peaks are still detected but with different intensities, representing the consumption of the higher-valent active polysulfides and the formation of  $\text{Li}_2\text{S}$ . At the end of the lower plateau (DoD = 100%, Figure 8.5(e)), unsurprisingly, only  $\text{Li}_2\text{S}$  is observed as the major product. From the recent work of Diao *et al.* (25),  $\text{Li}_2\text{S}_6$  and  $\text{Li}_2\text{S}_4$  are found as the most stable form of  $\text{Li}_2\text{S}_n$  compounds in the Li-S battery, so the first polysulfide with high binding energy in Figure 8.5(c) could be  $\text{Li}_2\text{S}_6$  and the second one with low binding energy in Figure 8.5(c) must be  $\text{Li}_2\text{S}_4$  according to the combined capacity of the upper plateau and the sloping region ( $\sim 419 \text{ mAh g}^{-1}$ ).<sup>123, 176</sup>

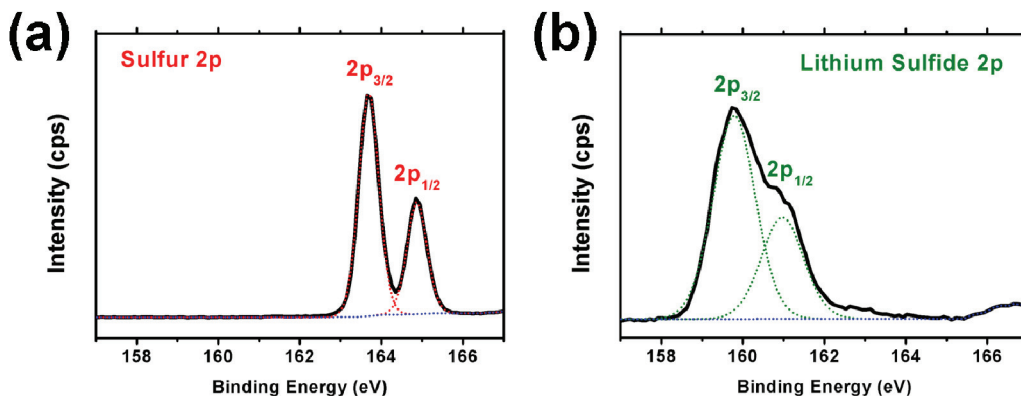


**Figure 8.4.** XPS curves of (a) pristine sulfur and (b) pristine lithium sulfide. ( $2p_{3/2}$ -sulfur: 163.7 eV;  $2p_{3/2}$ -lithium sulfide: 159.8 eV)

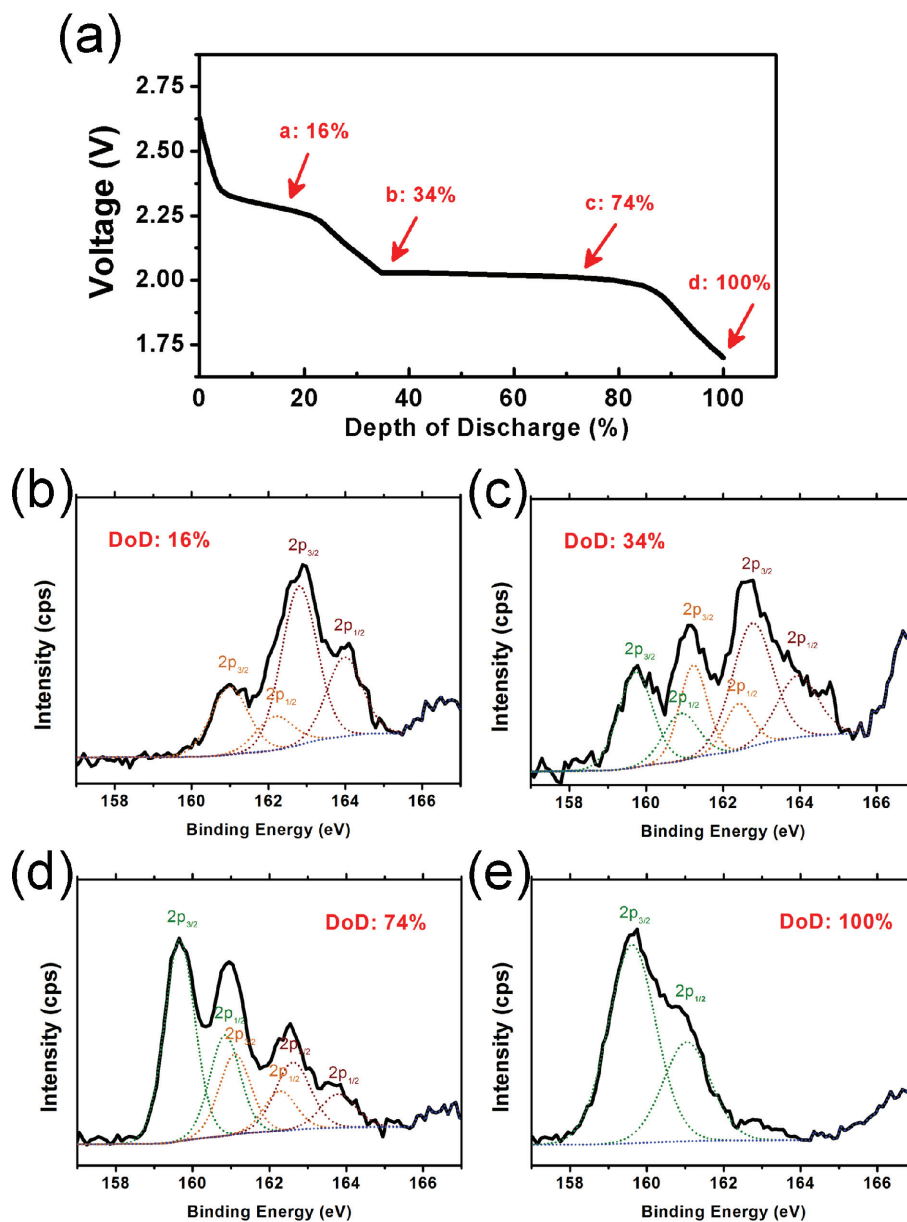


**Figure 8.5.** (a) Discharge curve of the Li-S cell cycled at C/2 rate with the depth of discharge (DoD) indicated. XPS plots of the active material at (b) 16% DoD, (c) 34% DoD, (d) 74% DoD, and (e) 100% DoD. ( $2p_{3/2}$ -brown( $\text{Li}_2\text{S}_6$ ): 162.8 eV;  $2p_{3/2}$ -yellow( $\text{Li}_2\text{S}_4$ ): 161.2 eV; and  $2p_{3/2}$ -green( $\text{Li}_2\text{S}$ ): 159.8 eV).

### 8.3.3 Discharge mechanism of the Li-S battery

In fact, early Li-S battery studies stated that  $\text{Li}_2\text{S}_2$  is stable in solid phase, yet it has not been fully confirmed in the sulfur cathode.<sup>27, 178</sup> Another early report claimed  $\text{Li}_2\text{S}_2$  is the main product of the lower plateau by the output capacity from the battery, but not by materials characterization.<sup>179</sup> Until now, there is no convincing proof from XRD showing the existence of  $\text{Li}_2\text{S}_2$  but only  $\text{Li}_2\text{S}$  after discharging,<sup>11, 174</sup> so the species of  $\text{Li}_2\text{S}_2$  might not dominate the battery reactions in this case. Barchasz *et al.*<sup>175</sup> applied UV-visible spectra to the determination of various polysulfides in Li-S cells, and the authors did observe the presence of  $\text{S}_8^{2-}$ ,  $\text{S}_6^{2-}$ ,  $\text{S}_3^{*-}$ ,  $\text{S}_5^{2-}$ ,  $\text{S}_4^{2-}$ ,  $\text{S}_3^{2-}$ ,  $\text{S}_2^{2-}$ , and  $\text{S}^{2-}$ . Nevertheless, several polysulfide species originate from the disproportionation reactions, but not redox reactions. On the other hand, the samples were measured in the form of catholyte, which might lead to different reaction mechanisms compared to ours. From former *ex situ* SEM analysis, solid-phase active material forms right after the beginning of the lower plateau reactions in accordance with the  $\text{Li}_2\text{S}$  detection in our report.<sup>11, 174</sup> Additionally, the migration of active material from its original location in carbon-based cathodes due to the polysulfide dissolution was observed.<sup>11, 27, 174</sup>  $\text{Li}_2\text{S}_6$  formed at the end of the upper plateau is found as a highly soluble lithium polysulfide from the observation of the electrolyte color,<sup>73, 180</sup> which is possibly the most unwanted soluble species in solid-state Li-S cells. By uniting the scientific reports above, we propose here a concise reaction mechanism for Li-S batteries in Figure 8.6. At a moderate or high cycling rate, the Li-S battery shows a three-step profile, the upper plateau, the sloping region, and the lower plateau, and each part represents the formation of predominate active materials, which are, respectively,  $\text{Li}_2\text{S}_6$ ,  $\text{Li}_2\text{S}_4$ , and  $\text{Li}_2\text{S}$ . Moreover, the polysulfide intermediates dissolved in the electrolyte are always a mixture, and they cannot be in the form of a single compound.<sup>176</sup> The discharge mechanism of Li-S cells with the

dioxolane/dimethoxyethane-based electrolyte is then clarified, although this may need to be modified for different electrolytes,<sup>19</sup> active material concentrations,<sup>175</sup> electrode designs,<sup>39</sup> and charge/discharge rates.

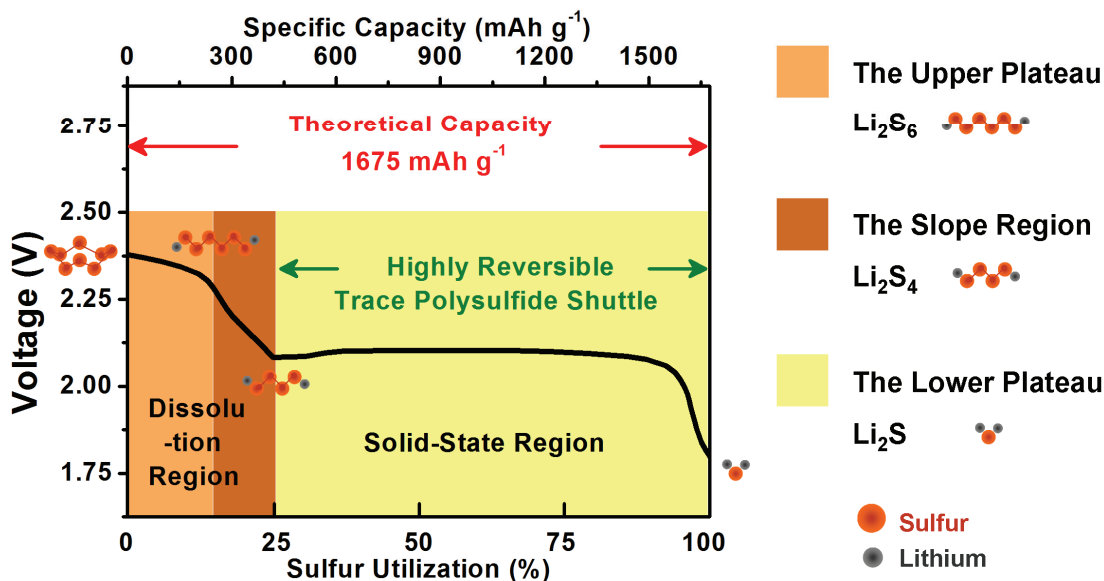


**Figure 8.6.** The discharge reaction mechanism of a Li-S battery, which can be divided into three regions: the upper plateau, the sloping region, and the lower plateau. The former two are located in the dissolution region, and the latter is located in the solid-state region that provides highly reversible capacity and has only a negligible amount of polysulfide shuttle behavior.

### 8.3.4 Long cycle life with the LiNO<sub>3</sub>-free electrolyte

LiNO<sub>3</sub> has been widely applied in Li-S cells to enhance Coulombic efficiency since it was found to passivate the Li anode and thus prevent the polysulfide shuttle attack.<sup>34, 130, 177</sup> However, LiNO<sub>3</sub> can be irreversibly reduced on the cathode surface, resulting in the instability of electrochemical reactions.<sup>130</sup> There are also safety concerns with LiNO<sub>3</sub> due to its strong oxidative property.<sup>21</sup> Furthermore, using this additive in the electrolyte may give researchers a misleading impression that battery systems work

perfectly once they obtain high Coulombic efficiency. Here, we also tested the cell with the interlayer but filled with a  $\text{LiNO}_3$ -free electrolyte to illustrate this point. Figure 8.7 compares the influence of the  $\text{LiNO}_3$  additive in the electrolyte on the Coulombic efficiency of the cell with the modified recharge setting. Even without the assistance of  $\text{LiNO}_3$ , the Li-S battery still has an efficiency of as high as 98.1% after 500 cycles, implying that the lower plateau reaction is highly reversible with minimal energy loss during charging. In other words, the long-standing polysulfide shuttle issue can be solved because of the suppression of the long-chain polysulfide production by employing our recharge strategy.

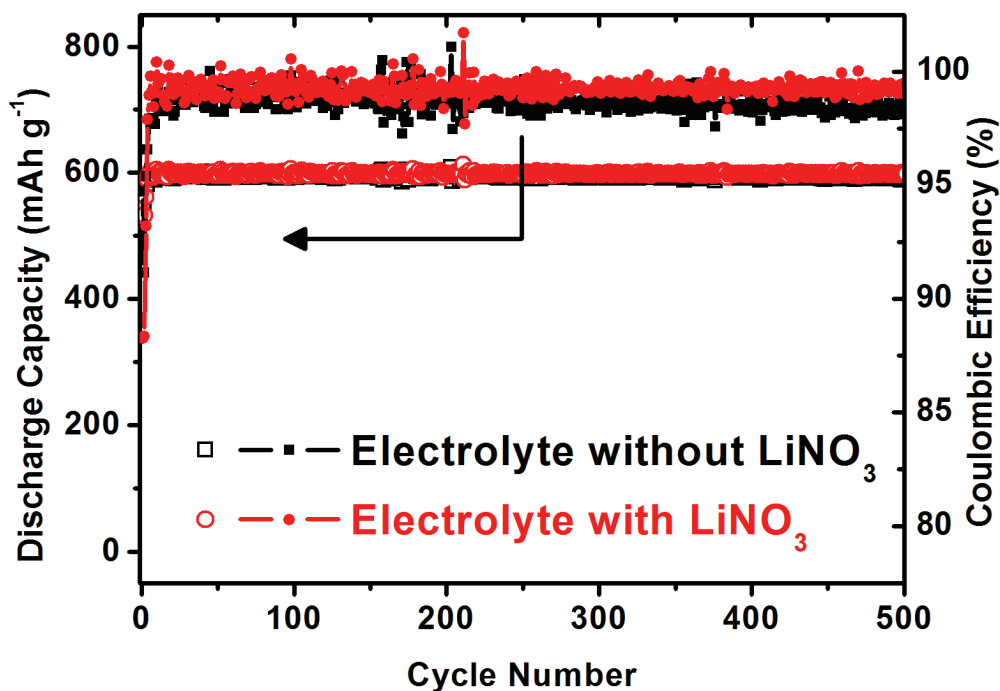


**Figure 8.7.** Impact of  $\text{LiNO}_3$  additive in the electrolyte on battery performance at C/5 rate. The  $\text{LiNO}_3$ -free electrolyte is also suitable for the Li-S cell by utilizing the modified recharge setting.

### 8.3.5 Dissolved polysulfide cells with the modified recharge setting

In order to determine whether this recharge setting is applicable to various Li-S battery systems, another promising lithium/dissolved polysulfide ( $\text{Li}_2\text{S}_6$ ) battery with a binder-free carbon nanofiber electrode, which is similar to our recent work with carbon nanotube electrodes, was cycled by only charging within the lower plateau region.<sup>73</sup> The microstructure of the low-cost carbon nanofiber mat is shown in Figure 8.8, which has an interwoven network that can trap the active material. It can be seen in Figure 8.9 that the initial discharge curve has only the sloping region and the lower plateau. Note that there is no upper plateau in this cell because the starting active material is  $\text{Li}_2\text{S}_6$  instead of pristine sulfur. Therefore,  $\text{Li}_2\text{S}_6$  should be generated right before the sloping region in a regular Li-S cell, and this behavior is in agreement with the assumed discharge mechanism we mentioned before. Figure 8.10(a) shows the discharge profiles of the battery after the 1<sup>st</sup>, 2<sup>nd</sup>, 3<sup>rd</sup>, 10<sup>th</sup>, and 50<sup>th</sup> cycles. These output capacities, which are contributed from the single plateau at near 2 V, are exactly similar. The extended cycling results are exhibited in Figure 8.10(b), and the superior cycle stability proves that the developed recharge setting can be broadly applied to different battery designs for elongating the cycle life of Li-S cells.

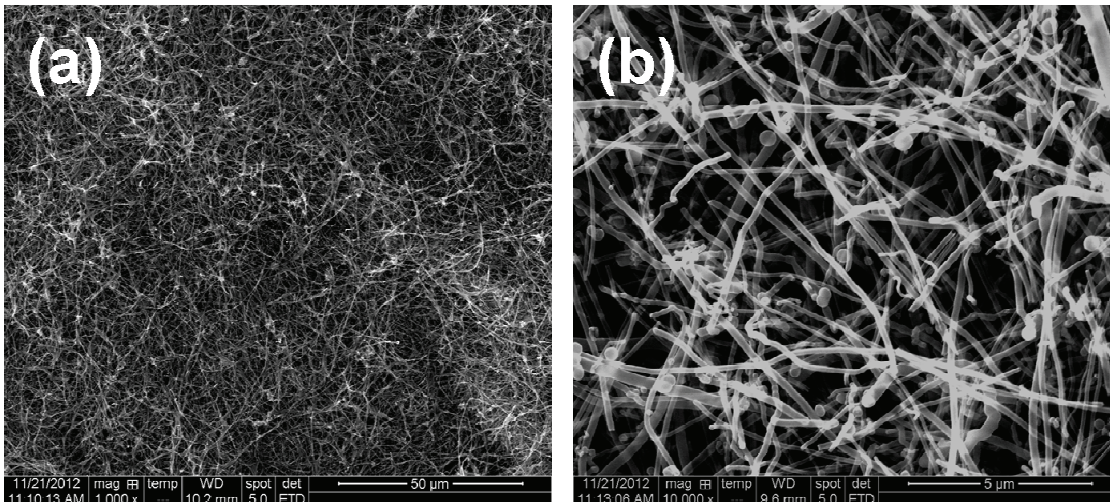


**Figure 8.8.** SEM of the CNF electrode of the Li/dissolved polysulfide cell with (a) low magnification and (b) high magnification.

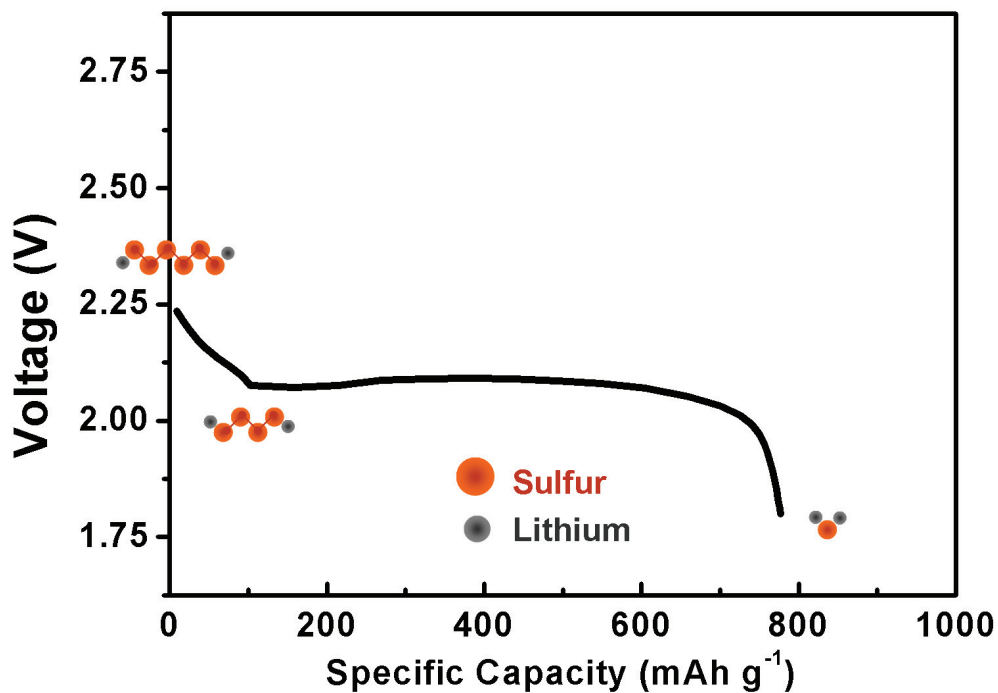


**Figure 8.9.** The initial discharge curve of the Li/dissolved polysulfide cell at C/5 rate. The starting active material is  $\text{Li}_2\text{S}_6$  instead of  $\text{S}_8$ .

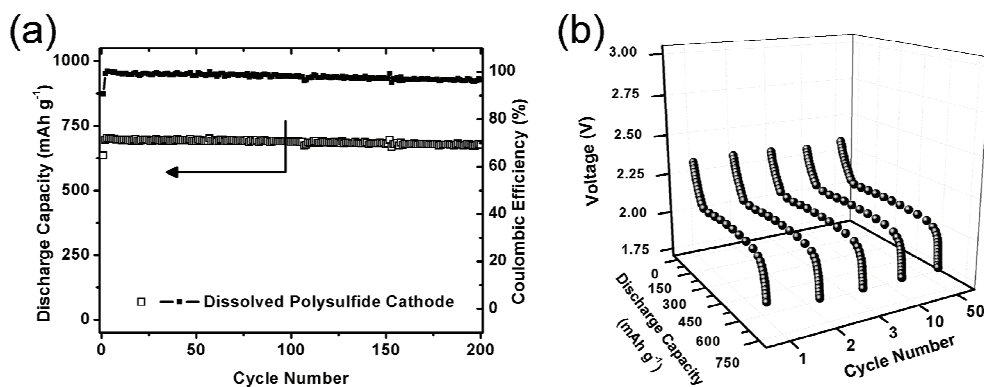


**Figure 8.10.** (a) Cyclability, Coulombic efficiency, and (b) discharge curves of the Li/dissolved polysulfide cells using commercial CNF electrodes with the modified recharge setting (charged to 700 mAh g<sup>-1</sup>) at C/5 rate.

## 8.4 CONCLUSIONS

In summary, the main cause of the deteriorating performance of Li-S batteries can be ascribed to the irreversible upper plateau reactions. Utilizing only the lower plateau during cycling significantly extends the cell cycle life, and it can be realized via a simple modified recharge setting. By charging the Li-S battery within the lower plateau capacity, high capacity and long cyclability with an ultra-low capacity degradation rate of 0.002% per cycle (~1% for 500 cycles here) can be readily obtained, which is the best capacity retention recorded in the literature at this time. The lower plateau near 2V involves the solid-state reaction directly forming Li<sub>2</sub>S confirmed by air-sensitive XPS analysis. Moreover, Li<sub>2</sub>S<sub>6</sub> and Li<sub>2</sub>S<sub>4</sub> are the major lithium polysulfide products detected in the upper plateau and sloping regions, and the former may be responsible for the capacity decay because of its high solubility. Moreover, the co-salt of LiNO<sub>3</sub> in the electrolyte will be unnecessary to improve the Coulombic efficiency if this recharge strategy is applied. This modified recharge approach is not only feasible with the Li-S cells with an interlayer configuration, but also is viable with the dissolved polysulfide systems. We believe this

recharge modification could be widely applied with various electrode designs and cell systems, thereby advancing the practical use of Li-S batteries for high-performance energy storage.

## Chapter 9: Summary

The conclusions on each aspect carried out in this dissertation are given under the conclusion section at the end of each chapter. Overall, the principles of developing a viable Li-S cell can be generalized as below, and this dissertation has contributed to some of these aspects.

- *Appropriate dispersion of active sulfur:* Although sulfur transforms into soluble polysulfides during cycling, the utilization of active material will be low if sulfur has insufficient contact with conductive agents, resulting in poor specific capacity. Therefore, electrode fabrication should be optimized, for example, as discussed in Chapters 3 and 4.
- *Efficient absorbing materials:* Even though the currently developed carbon frameworks seem to be a good fit for accommodating sulfur, the high carbon content in the cathode region decreases the energy density and still remains unsatisfactory. New conductive/porous materials need to be designed for the infiltration of sulfur, and the gravimetric/volumetric energy density should not be degraded too much at the same time. Binder-free fabrication process is also desired, which can eliminate unnecessary polymer binders and raise the sulfur loading in the cathode. These aspects were discussed in Chapters 5, 6, and 7.
- *Stable electrolyte systems:* The current liquid electrolyte is barely acceptable, but still not good enough for the commercialization of Li-S cells because of the side reactions between polysulfides/electrolyte solvent/lithium metal. A more reliable electrolyte is preferred to avoid the consumption of electrolyte, which could reduce the capacity degradation of Li-S batteries. This dissertation did not focus on this aspect.

- *Safer anode materials*: Employing lithium metal anodes always brings safety concern; therefore, protected lithium anodes and prelithiated high-energy anodes may be two feasible directions for building a safer Li-S cell. This dissertation did not focus on this aspect.
- *Intelligent recharge settings*: Utilizing only the lower plateau (~2 V) region has been proved as a practical means to significantly improve the cycle life of the Li-S battery. The only concern is that the utilization of the lower plateau must be high enough ( $> 1000 \text{ mAh g}^{-1}$ ); otherwise, the merit of applying high-energy sulfur cathodes will vanish. These aspects were discussed in Chapter 8.

By taking these principles into account, a practical Li-S battery is probable to be developed and applied in the future.

## Appendix: List of Publications

1. **Y.-S. Su**, Y.-Z. Fu, B. Guo, S. Dai and A. Manthiram, "Fast, Reversible Lithium Storage with a Sulfur/Long-Chain Polysulfides Redox Couple," *Chem. Eur. J.*, 2013, 19, 8621-8626.
2. Y.-Z. Fu, **Y.-S. Su** and A. Manthiram, "Highly Reversible Lithium/Dissolved Polysulfide Batteries with Carbon Nanotube Electrodes," *Angew. Chem. Int. Ed.*, 2013, 52, 6930-6935.
3. A. Manthiram, Y.-Z. Fu and **Y.-S. Su**, "In Charge of the World: Electrochemical Energy Storage," *J. Phys. Chem. Lett.*, 2013, 4, 1295-1297.
4. A. Manthiram, Y.-Z. Fu and **Y.-S. Su**, "Challenges and Prospects of Lithium-Sulfur Batteries," *Acc. Chem. Res.*, 2013, 46, 1125-1134.
5. C. Zu, **Y.-S. Su**, Y.-Z. Fu and A. Manthiram, "Improved Lithium-Sulfur Cells with a Treated Carbon Paper Interlayer," *Phys. Chem. Chem. Phys.*, 2013, 15, 2291-2297.
6. Y.-Z. Fu, **Y.-S. Su** and A. Manthiram, "Li<sub>2</sub>S-Carbon Sandwiched Electrodes with Superior Performance for Lithium-Sulfur Batteries," *Adv. Energy Mater.*, 2013, (in press).
7. **Y.-S. Su**, Y.-Z. Fu, T. Cochell and A. Manthiram, "A Strategic Approach to Recharge Li-S Batteries for Long Cycle Life," *Nat. Commun.*, 2013, (in revision).
8. **Y.-S. Su** and A. Manthiram, "Sulfur-Intercalation Compounds Hybrid Cathode System for Li-S Cells," 2013, *Electrochem. Commun.*, (in preparation).
9. A. Manthiram, **Y.-S. Su et al.**, "Progress of Lithium-Sulfur Batteries," *Chemical Reviews*, 2013, (in preparation).
10. A. Manthiram, Y.-Z. Fu and **Y.-S. Su**, "Rechargeable Lithium-Sulfur Batteries," *Wiley Book Chapter*, Woodhead Publishing, Cambridge, United Kingdom, 2013, (in press).
11. **Y.-S. Su** and A. Manthiram, "Lithium-Sulphur Batteries with a Microporous Carbon Paper as a Bifunctional Interlayer," *Nat. Commun.*, 2012, 3, 1166.
12. **Y.-S. Su** and A. Manthiram, "A New Approach to Improve Cycle Performance of Rechargeable Lithium-Sulfur Batteries by Inserting a Free-Standing MWCNT Interlayer," *Chem. Commun.*, 2012, 48, 8817-8819.

13. **Y.-S. Su**, Y.-Z. Fu and A. Manthiram, "Self-Weaving Sulfur–Carbon Composite Cathodes for High Rate Lithium–Sulfur Batteries," *Phys. Chem. Chem. Phys.*, 2012, 14, 14495-14499.
14. **Y.-S. Su** and A. Manthiram, "A Facile *In Situ* Sulfur Deposition Route to Obtain Carbon-Wrapped Sulfur Composite Cathodes for Lithium-Sulfur Batteries," *Electrochim. Acta*, 2012, 77, 272-278.
15. Y.-Z. Fu, **Y.-S. Su** and A. Manthiram, "Sulfur-Carbon Nanocomposite Cathodes Improved by an Amphiphilic Block Copolymer for High Rate Lithium-Sulfur Batteries," *ACS Appl. Mater. Interfaces*, 2012, 4, 6046-6052.
16. Y.-Z. Fu, **Y.-S. Su** and A. Manthiram, "Sulfur-Polypyrrole Composite Cathodes for Lithium-Sulfur Batteries," *J. Electrochem. Soc.*, 2012, 159, A1420-A1424.

## References

1. F. Schlachter, *Proceedings of the National Academy of Sciences*, **110**, 5273 (2013).
2. M. S. Whittingham, *Chem. Rev.*, **104**, 4271 (2004).
3. M. Armand, J. M. Tarascon, *Nature*, **451**, 652 (2008).
4. J. B. Goodenough, Y. Kim, *Chem. Mater.*, **22**, 587 (2010).
5. B. Scrosati, J. Garche, *J. Power Sources*, **195**, 2419 (2010).
6. P. G. Bruce, S. A. Freunberger, L. J. Hardwick, J. M. Tarascon, *Nat. Mater.*, **11**, 19 (2012).
7. X. L. Ji, L. F. Nazar, *J. Mater. Chem.*, **20**, 9821 (2010).
8. A. Manthiram, Y. Fu, Y.-S. Su, *Acc. Chem. Res.*, **46**, 1125 (2013).
9. “Mineral commodity summaries 2013: U.S. Geological Survey” (U.S. Geological Survey, Reston, Virginia, 2013).
10. Y.-S. Su, Y. Fu, T. Cochell, A. Manthiram, *Nat. Commun.*, (in revision) (2013).
11. L. X. Yuan, X. P. Qiu, L. Q. Chen, W. T. Zhu, *J. Power Sources*, **189**, 127 (2009).
12. W. Ahn, K. B. Kim, K. N. Jung, K. H. Shin, C. S. Jin, *J. Power Sources*, **202**, 394 (2012).
13. J. Nelson *et al.*, *J. Am. Chem. Soc.*, **134**, 6337 (2012).
14. A. Manthiram, Y. Z. Fu, Y. S. Su, *J. Phys. Chem. Lett.*, **4**, 1295 (2013).
15. Y. Yang, G. Y. Zheng, Y. Cui, *Energy Environ. Sci.*, **6**, 1552 (2013).
16. B. Dunn, H. Kamath, J. M. Tarascon, *Science*, **334**, 928 (2011).
17. Z. G. Yang *et al.*, *Chem. Rev.*, **111**, 3577 (2011).
18. J. A. Dean, *Lange's handbook of chemistry*. (New York : McGraw-Hill, ed. 15th ed., 1999).

19. R. D. Rauh, F. S. Shuker, J. M. Marston, S. B. Brummer, *J. Inorg. Nucl. Chem.*, **39**, 1761 (1977).
20. R. D. Rauh, K. M. Abraham, G. F. Pearson, J. K. Surprenant, S. B. Brummer, *J. Electrochem. Soc.*, **126**, 523 (1979).
21. S. S. Zhang, *J. Power Sources*, **231**, 153 (2013).
22. Y. Mikhaylik *et al.*, in *Battery/Energy Technology*, Z. Ogumi, N. J. Dudney, S. R. Narayanan, Eds. (Electrochemical Soc Inc, Pennington, 2010), vol. 25, pp. 23-34.
23. H. S. Ryu *et al.*, *Electrochim. Acta*, **52**, 1563 (2006).
24. H. S. Ryu *et al.*, *J. Power Sources*, **140**, 365 (2005).
25. H. Yamin, E. Peled, *J. Power Sources*, **9**, 281 (1983).
26. Y. V. Mikhaylik, J. R. Akridge, *J. Electrochem. Soc.*, **151**, A1969 (2004).
27. S. E. Cheon *et al.*, *J. Electrochem. Soc.*, **150**, A796 (2003).
28. Y. Diao, K. Xie, S. Xiong, X. Hong, *J. Power Sources*, **235**, 181 (2013).
29. Y.-S. Su, A. Manthiram, *Electrochim. Acta*, **77**, 272 (2012).
30. S. S. Zhang, J. A. Read, *J. Power Sources*, **200**, 77 (2012).
31. S. E. Cheon *et al.*, *J. Electrochem. Soc.*, **151**, A2067 (2004).
32. S. E. Cheon *et al.*, *J. Electrochem. Soc.*, **150**, A800 (2003).
33. B. H. Jeon, J. H. Yeon, K. M. Kim, I. J. Chung, *J. Power Sources*, **109**, 89 (2002).
34. D. Aurbach *et al.*, *J. Electrochem. Soc.*, **156**, A694 (2009).
35. X. M. He *et al.*, *J. Power Sources*, **190**, 154 (2009).
36. X. L. Ji, K. T. Lee, L. F. Nazar, *Nat. Mater.*, **8**, 500 (2009).
37. B. Zhang, C. Lai, Z. Zhou, X. P. Gao, *Electrochim. Acta*, **54**, 3708 (2009).
38. C. Wang, J. J. Chen, Y. N. Shi, M. S. Zheng, Q. F. Dong, *Electrochim. Acta*, **55**, 7010 (2010).
39. S. Xin *et al.*, *J. Am. Chem. Soc.*, **134**, 18510 (2012).

40. B. Zhang, X. Qin, G. R. Li, X. P. Gao, *Energy Environ. Sci.*, **3**, 1531 (2010).
41. X. L. Li *et al.*, *J. Mater. Chem.*, **21**, 16603 (2011).
42. D. Li *et al.*, *ACS Appl. Mater. Interfaces*, **5**, 2208 (2013).
43. X. Y. Tao *et al.*, *J. Mater. Chem. A*, **1**, 3295 (2013).
44. J. Schuster *et al.*, *Angew. Chem. Int. Ed.*, **51**, 3591 (2012).
45. C. D. Liang, N. J. Dudney, J. Y. Howe, *Chem. Mater.*, **21**, 4724 (2009).
46. S. R. Chen *et al.*, *Electrochim. Acta*, **56**, 9549 (2011).
47. B. Ding *et al.*, *Chem.-Eur. J.*, **19**, 1013 (2013).
48. K. Xi *et al.*, *Chem. Commun.*, **49**, 2192 (2013).
49. S. C. Wei *et al.*, *Energy Environ. Sci.*, **4**, 736 (2011).
50. C. F. Zhang, H. B. Wu, C. Z. Yuan, Z. P. Guo, X. W. Lou, *Angew. Chem. Int. Ed.*, **51**, 9592 (2012).
51. N. Jayaprakash, J. Shen, S. S. Moganty, A. Corona, L. A. Archer, *Angew. Chem. Int. Ed.*, **50**, 5904 (2011).
52. N. Brun *et al.*, *PCCP*, **15**, 6080 (2013).
53. S. C. Han *et al.*, *J. Electrochem. Soc.*, **150**, A889 (2003).
54. S. S. Jeong, Y. J. Choi, K. W. Kim, in *Eco-Materials Processing & Design Vii*, H. S. Kim, Y. B. Li, S. W. Lee, Eds. (Trans Tech Publications Ltd, Zurich-Uetikon, 2006), vol. 510-511, pp. 1106-1109.
55. L. X. Yuan, H. P. Yuan, X. P. Qiu, L. Q. Chen, W. T. Zhu, *J. Power Sources*, **189**, 1141 (2009).
56. J. J. Chen *et al.*, *Electrochim. Acta*, **55**, 8062 (2010).
57. W. Wei *et al.*, *Electrochem. Commun.*, **13**, 399 (2011).
58. J.-J. Chen *et al.*, *Physical chemistry chemical physics : PCCP*, **14**, 5376 (2012).
59. Y.-S. Su, Y. Z. Fu, A. Manthiram, *PCCP*, **14**, 14495 (2012).
60. J. Guo, Y. Xu, C. Wang, *Nano Lett.*, **11**, 4288 (2011).

61. Y. J. Choi, K. W. Kim, H. J. Ahn, J. H. Ahn, *J. Alloys Compd.*, **449**, 313 (2008).
62. G. Zheng, Y. Yang, J. J. Cha, S. S. Hong, Y. Cui, *Nano Lett.*, **11**, 4462 (2011).
63. L. W. Ji *et al.*, *Energy Environ. Sci.*, **4**, 5053 (2011).
64. M. M. Rao, X. Y. Song, E. J. Cairns, *J. Power Sources*, **205**, 474 (2012).
65. H. Wang *et al.*, *Nano Lett.*, null (2011).
66. L. W. Ji *et al.*, *J. Am. Chem. Soc.*, **133**, 18522 (2011).
67. S. Evers, L. F. Nazar, *Chem. Commun.*, **48**, 1233 (2012).
68. N. Li *et al.*, *Chem. Commun.*, **48**, 4106 (2012).
69. J. Q. Huang *et al.*, *Nano Energy*, **2**, 314 (2013).
70. C. Zu, A. Manthiram, *Adv. Energy Mater.*, (in press) (2013).
71. J. L. Wang, J. Yang, J. Y. Xie, N. X. Xu, Y. Li, *Electrochem. Commun.*, **4**, 499 (2002).
72. G. He, X. L. Ji, L. Nazar, *Energy Environ. Sci.*, **4**, 2878 (2011).
73. Y. Z. Fu, Y.-S. Su, A. Manthiram, *Angew. Chem. Int. Ed.*, **52**, 6930 (2013).
74. S. S. Zhang, D. T. Tran, *J. Power Sources*, **211**, 169 (2012).
75. Y.-S. Su, A. Manthiram, *Chem. Commun.*, **48**, 8817 (2012).
76. Y.-S. Su, A. Manthiram, *Nat. Commun.*, **3**, 1166 (2012).
77. W. Zheng, Y. W. Liu, X. G. Hu, C. F. Zhang, *Electrochim. Acta*, **51**, 1330 (2006).
78. K. P. Lee, N. C. Chromey, R. Culik, J. R. Barnes, P. W. Schneider, *Fundam. Appl. Toxicol.*, **9**, 222 (1987).
79. S. Y. Chew *et al.*, *Carbon*, **47**, 2976 (2009).
80. S. H. Ng, J. Wang, Z. P. Guo, G. X. Wang, H. K. Liu, *Electrochim. Acta*, **51**, 23 (2005).
81. R. Elazari, G. Salitra, A. Garsuch, A. Panchenko, D. Aurbach, *Adv. Mater.*, **23**, 5641 (2011).

82. S. Dorfler *et al.*, *Chem. Commun.*, **48**, 4097 (2012).
83. A. K. Geim, K. S. Novoselov, *Nature Materials*, **6**, 183 (2007).
84. C. X. Zu, Y.-S. Su, Y. Z. Fu, A. Manthiram, *PCCP*, **15**, 2291 (2013).
85. J. Wang *et al.*, *Electrochim. Acta*, **51**, 4634 (2006).
86. Y. Z. Fu, A. Manthiram, *J. Phys. Chem. C*, **116**, 8910 (2012).
87. Y. Z. Fu, A. Manthiram, *Chem. Mater.*, **24**, 3081 (2012).
88. Y. Z. Fu, Y.-S. Su, A. Manthiram, *J. Electrochem. Soc.*, **159**, A1420 (2012).
89. Y. Z. Fu, A. Manthiram, *RSC Adv.*, **2**, 5927 (2012).
90. F. Wu, J. Z. Chen, L. Li, T. Zhao, R. J. Chen, *J. Phys. Chem. C*, **115**, 24411 (2011).
91. L. Xiao *et al.*, *Adv. Mater.*, **24**, 1176 (2012).
92. F. Wu *et al.*, *J. Phys. Chem. C*, **115**, 6057 (2011).
93. F. Wu, S. X. Wu, R. J. Chen, J. Z. Chen, S. Chen, *Electrochem. Solid State Lett.*, **13**, A29 (2010).
94. W. Y. Li *et al.*, *Proc. Natl. Acad. Sci. U. S. A.*, **110**, 7148 (2013).
95. J. L. Wang *et al.*, *Adv. Funct. Mater.*, **13**, 487 (2003).
96. L. C. Yin, J. L. Wang, J. Yang, Y. N. Nuli, *J. Mater. Chem.*, **21**, 6807 (2011).
97. Y. Fu, Y.-S. Su, A. Manthiram, *ACS Appl. Mater. Interfaces*, **4**, 6046 (2012).
98. G. Y. Zheng *et al.*, *Nano Lett.*, **13**, 1265 (2013).
99. M. S. Song *et al.*, *J. Electrochem. Soc.*, **151**, A791 (2004).
100. Y. G. Zhang, Y. Zhao, A. Yermukhambetova, Z. Bakenov, P. Chen, *J. Mater. Chem. A*, **1**, 295 (2013).
101. Y. J. Choi *et al.*, *Phys. Scr.*, **T129**, 62 (2007).
102. X. L. Ji, S. Evers, R. Black, L. F. Nazar, *Nat. Commun.*, **2**, (2011).
103. S. Evers, T. Yim, L. F. Nazar, *J. Phys. Chem. C*, **116**, 19653 (2012).

104. Z. W. Seh *et al.*, *Nat. Commun.*, **4**, (2013).
105. Y.-S. Su, A. Manthiram, *Electrochem. Commun.*, (in preparation) (2013).
106. J. E. Trevey, C. R. Stoldt, S. H. Lee, *J. Electrochem. Soc.*, **158**, A1282 (2011).
107. Y. Yang *et al.*, *Nano Lett.*, **10**, 1486 (2010).
108. J. Hassoun, B. Scrosati, *Angew. Chem.-Int. Edit.*, **49**, 2371 (2010).
109. J. Hassoun, Y. K. Sun, B. Scrosati, *J. Power Sources*, **196**, 343 (2011).
110. Y. Yang *et al.*, *J. Am. Chem. Soc.*, **134**, 15387 (2012).
111. K. P. Cai, M. K. Song, E. J. Cairns, Y. G. Zhang, *Nano Lett.*, **12**, 6474 (2012).
112. Y. Fu, Y.-S. Su, A. Manthiram, *Adv. Energy Mater.*, (in press) (2013).
113. J. C. Guo, Z. C. Yang, Y. C. Yu, H. D. Abruna, L. A. Archer, *J. Am. Chem. Soc.*, **135**, 763 (2013).
114. C. Barchasz *et al.*, *J. Power Sources*, **211**, 19 (2012).
115. S.-H. Chung, A. Manthiram, *Electrochim. Acta*, **107**, 569 (2013).
116. S.-H. Chung, A. Manthiram, *J. Mater. Chem. A*, (in press) (2013).
117. Y. Q. Huang *et al.*, *J. Electrochem. Soc.*, **155**, A764 (2008).
118. J. Sun *et al.*, *Electrochim. Acta*, **53**, 7084 (2008).
119. Y. Wang *et al.*, *Electrochim. Acta*, **54**, 4062 (2009).
120. M. He, L. X. Yuan, W. X. Zhang, X. L. Hu, Y. H. Huang, *J. Phys. Chem. C*, **115**, 15703 (2011).
121. Z. A. Zhang *et al.*, *ECS Electrochem. Lett.*, **1**, A34 (2012).
122. J. L. Wang, Z. D. Yao, C. W. Monroe, J. Yang, Y. Nuli, *Adv. Funct. Mater.*, **23**, 1194 (2013).
123. Y.-S. Su, Y. Fu, B. Guo, S. Dai, A. Manthiram, *Chem. Eur. J.*, **19**, 8621 (2013).
124. J. W. Choi *et al.*, *Electrochim. Acta*, **52**, 2075 (2007).

125. D. R. Chang, S. H. Lee, S. W. Kim, H. T. Kim, *J. Power Sources*, **112**, 452 (2002).
126. J. Gao, M. A. Lowe, Y. Kiya, H. D. Abruna, *J. Phys. Chem. C*, **115**, 25132 (2011).
127. D. W. Wang *et al.*, *PCCP*, **14**, 8703 (2012).
128. W. H. Zhang *et al.*, *Electrochim. Acta*, **87**, 497 (2013).
129. Y. V. Mikhaylik. (US Patent 7354680, 2008).
130. S. S. Zhang, *Electrochim. Acta*, **70**, 344 (2012).
131. L. M. Suo, Y. S. Hu, H. Li, M. Armand, L. Q. Chen, *Nat. Commun.*, **4**, (2013).
132. M. Armand, F. Endres, D. R. MacFarlane, H. Ohno, B. Scrosati, *Nature Materials*, **8**, 621 (2009).
133. M. Galinski, A. Lewandowski, I. Stepniak, *Electrochim. Acta*, **51**, 5567 (2006).
134. L. X. Yuan *et al.*, *Electrochem. Commun.*, **8**, 610 (2006).
135. J. Wang *et al.*, *Carbon*, **46**, 229 (2008).
136. J. W. Park *et al.*, *J. Phys. Chem. C*, **117**, 4431 (2013).
137. Y. Yan *et al.*, *Electrochim. Acta*, **91**, 58 (2013).
138. B. K. Guo *et al.*, *Chem. Commun.*, **49**, 4905 (2013).
139. J. Hassoun, B. Scrosati, *Adv. Mater.*, **22**, 5198 (2010).
140. A. Hayashi, T. Ohtomo, F. Mizuno, K. Tadanaga, M. Tatsumisago, *Electrochem. Commun.*, **5**, 701 (2003).
141. M. Nagao, A. Hayashi, M. Tatsumisago, *Electrochim. Acta*, **56**, 6055 (2011).
142. J. E. Trevey, J. R. Gilsdorf, C. R. Stoldt, S. H. Lee, P. Liu, *J. Electrochem. Soc.*, **159**, A1019 (2012).
143. J. E. Trevey, Y. S. Jung, S. H. Lee, *Electrochim. Acta*, **56**, 4243 (2011).
144. Y. M. Lee, N. S. Choi, J. H. Park, J. K. Park, *J. Power Sources*, **119**, 964 (2003).
145. J. Hassoun *et al.*, *J. Power Sources*, **202**, 308 (2012).

146. Y. V. Mikhaylik, J. R. Akridge, *J. Electrochem. Soc.*, **150**, A306 (2003).
147. X. M. He *et al.*, *Ionics*, **14**, 335 (2008).
148. A. Manthiram, *J. Phys. Chem. Lett.*, **2**, 176 (2011).
149. K. Kumaresan, Y. Mikhaylik, R. E. White, *J. Electrochem. Soc.*, **155**, A576 (2008).
150. C. Lai, X. P. Gao, B. Zhang, T. Y. Yan, Z. Zhou, *J. Phys. Chem. C*, **113**, 4712 (2009).
151. S. Li, M. Xie, J. B. Liu, H. Wang, H. Yan, *Electrochem. Solid State Lett.*, **14**, A105 (2011).
152. S. R. Narayanan, D. H. Shen, S. Surampudi, A. I. Attia, G. Halpert, *J. Electrochem. Soc.*, **140**, 1854 (1993).
153. T. Ohzuku, R. J. Brodd, *J. Power Sources*, **174**, 449 (2007).
154. T. Muraliganth, A. V. Murugan, A. Manthiram, *J. Mater. Chem.*, **18**, 5661 (2008).
155. X. L. Li, F. Y. Kang, X. D. Bai, W. Shen, *Electrochem. Commun.*, **9**, 663 (2007).
156. K. Sheem, Y. H. Lee, H. S. Lim, *J. Power Sources*, **158**, 1425 (2006).
157. Z. C. Wu *et al.*, *Science*, **305**, 1273 (2004).
158. H. S. Ryu, Z. P. Guo, H. J. Ahn, G. B. Cho, H. K. Liu, *J. Power Sources*, **189**, 1179 (2009).
159. D. Peramunage, S. Licht, *Science*, **261**, 1029 (1993).
160. M. S. Dresselhaus, G. Dresselhaus, R. Saito, A. Jorio, *Physics Reports-Review Section of Physics Letters*, **409**, 47 (2005).
161. M. Kruk, M. Jaroniec, *Chem. Mater.*, **13**, 3169 (2001).
162. G. Pognon, T. Brousse, D. Belanger, *Carbon*, **49**, 1340 (2011).
163. O. Knop, R. J. Boyd, S. C. Choi, *J. Am. Chem. Soc.*, **110**, 7299 (1988).
164. A. I. Boldyrev, J. Simons, P. V. Schleyer, *J. Chem. Phys.*, **99**, 8793 (1993).
165. Y. Wang, G. Z. Cao, *Adv. Mater.*, **20**, 2251 (2008).

166. J. Chen, F. Y. Cheng, *Acc. Chem. Res.*, **42**, 713 (2009).
167. C. Liu, F. Li, L. P. Ma, H. M. Cheng, *Adv. Mater.*, **22**, E28 (2010).
168. H. L. Wang *et al.*, *Angew. Chem.-Int. Edit.*, **50**, 7364 (2011).
169. H. G. Zhang, X. D. Yu, P. V. Braun, *Nat. Nanotechnol.*, **6**, 277 (2011).
170. X. Q. Wang, J. S. Lee, C. Tsouris, D. W. DePaoli, S. Dai, *J. Mater. Chem.*, **20**, 4602 (2010).
171. Y. Fu, Y.-S. Su, A. Manthiram, *Angew. Chem. Int. Ed.*, **52**, 6930 (2013).
172. W. Weng, V. G. Pol, K. Amine, *Adv. Mater.*, **25**, 1608 (2013).
173. R. V. Chebiam, A. M. Kannan, F. Prado, A. Manthiram, *Electrochem. Commun.*, **3**, 624 (2001).
174. N. A. Canas, S. Wolf, N. Wagner, K. A. Friedrich, *J. Power Sources*, **226**, 313 (2013).
175. C. Barchasz *et al.*, *Anal. Chem.*, **84**, 3973 (2012).
176. Y. Diao, K. Xie, S. Z. Xiong, X. B. Hong, *J. Electrochem. Soc.*, **159**, A421 (2012).
177. S. Z. Xiong, K. Xie, Y. Diao, X. B. Hong, *Electrochim. Acta*, **83**, 78 (2012).
178. H. Yamin, A. Gorenshstein, J. Penciner, Y. Sternberg, E. Peled, *J. Electrochem. Soc.*, **135**, 1045 (1988).
179. E. Peled, Y. Sternberg, A. Gorenshstein, Y. Lavi, *J. Electrochem. Soc.*, **136**, 1621 (1989).
180. Y. J. Li, H. Zhan, S. Q. Liu, K. L. Huang, Y. H. Zhou, *J. Power Sources*, **195**, 2945 (2010).

## **Vita**

Yu-Sheng Su was born in 1983, in Kaohsiung, Taiwan. Later he moved with his family to Taipei, Taiwan. He was an intern at the Industrial Technology Research Institute for the lithium-ion batteries project in 2004. He received his B.S. and M.S. degrees in Materials Science and Engineering from National Tsing Hua University in Hsinchu, Taiwan, respectively, in 2005 and 2007. After receiving his M.S. degree, he served in the military until September 2008. Then he worked at Academia Sinica as a research assistant in the area of environmental changes. In August 2009, he joined the Materials Science and Engineering Graduate Program at the University of Texas at Austin and focused on advanced lithium-sulfur batteries research.

Email Address: [yushengsu@gmail.com](mailto:yushengsu@gmail.com)

This dissertation was typed by the author.